Molecular Beam Epitaxy of AlGaN Epilayers on Foreign Substrates for Semiconductor Deep Ultraviolet Lasers

Xue Yin

Department of Electrical & Computer Engineering
McGill University
Montréal, Canada
August 2023

A thesis submitted to McGill University in partial fulfillment of the requirements of the degree of Doctor of Philosophy

To my beloved parents and husband, Xingyu

Abstract

Aluminum gallium nitride (AlGaN) ultraviolet (UV) laser diodes (LDs) are of great research interest due to their wide range of applications and promising future to replace today's dominant UV lasing technologies, such as gas lasers and solid-state lasers. Nonetheless, the majority of the studies on AlGaN deep UV lasers are still on optical pumping and the development of electrically driven counterparts is relatively slow, mainly rooted in the difficulties in achieving high quality AlGaN epilayers and insufficient p-type conduction. In addition, the AlGaN UV laser research predominantly relies on the structures grown by metalorganic chemical vapor deposition (MOCVD) and the research of AlGaN UV lasers by molecular beam epitaxy (MBE) is rare. It is also noted that the recent progress on electrically injected AlGaN deep UV lasers relies on expensive AlN substrates.

The research in this dissertation follows the track of MBE-grown AlGaN on cost-effective foreign substrates, such as silicon (Si) and sapphire, to address the current impediments. This research first demonstrates a novel buffer layer technology, which enables low-cost, highly reproducible, high quality, and nearly strain-free AlN thin film through exploiting the low Al adatom migration during the coalescence process on a GaN nanowire template on Si. This research further demonstrates high quality AlGaN epilayers on such nanowire-assisted AlN templates by MBE. Peak internal quantum efficiency (IQE) of ~50% is derived, which is significantly improved compared to the previously reported bulk AlGaN epilayers on sapphire.

In parallel, the research in this dissertation also, for the first time, reports deep UV lasing from MBE-grown AlGaN on sapphire by optical pumping, with clear lasing evidence. Lasing at 298 nm from the AlGaN/AlN double heterostructure (DH) is first obtained, with a lasing threshold of 950 kW/cm^2. This research further studies the correlation between point defects and lasing threshold, reducing the lasing threshold to 530 kW/cm^2 at 287 nm, together with an increase in IQE of ~16%. Towards the electrically injected AlGaN UV LDs, the research in this dissertation designs and numerically investigates a unique Al-content engineered superlattice electron blocking layer (AESL-EBL), which not only improves charge carrier transport with the assistance of hot hole effects but also minimizes optical loss due to doping.

Abrégé

Les diodes laser ultraviolets (UV) à base de nitrure d'aluminium-gallium (AlGaN) suscitent un grand intérêt en recherche en raison de leur large éventail d'applications et de leur avenir prometteur pour remplacer les technologies de laser UV dominantes actuelles, telles que les lasers à gaz et les lasers à solide. Néanmoins, la majorité des études sur les lasers UV profonds en AlGaN portent encore sur le pompage optique et le développement de leurs homologues électriquement pilotés est relativement lent, principalement en raison des difficultés à obtenir des épitaxies AlGaN de haute qualité et de la conduction de type p insuffisante. En outre, la recherche sur les lasers UV en AlGaN repose principalement sur des structures développées par épitaxie en phase vapeur aux organométalliques (EPVOM) et les travaux sur les lasers UV en AlGaN par épitaxie par jets moléculaires (MBE) sont rares. Il convient également de souligner que les avancées récentes des lasers UV profonds à injection électrique en AlGaN sont tous réalisés sur des substrats en AlN coûteux.

La recherche dans cette dissertation suit la voie de l'AlGaN développé par MBE sur des substrats étrangers économiques, tels que silicium (Si) et saphir, pour surmonter les obstacles actuels. Cette recherche démontre d'abord une nouvelle technologie de couche tampon, qui permet d'obtenir un film mince AlN peu coûteux, hautement reproductible, de haute qualité et presque exempt de contraintes en exploitant la faible migration des adatomes d'Al lors du processus de coalescence sur un modèle de nanofil de GaN sur Si. Cette recherche montre également des épitaxies AlGaN de haute qualité sur de tels modèles d'AlN assistés par nanofils grâce à l'utilisation de MBE. Une efficacité quantique interne (IQE) maximal d'environ 50% est obtenu, ce qui représente une amélioration significative par rapport aux couches épitaxiales massives d'AlGaN sur saphir précédemment rapportées.

En parallèle, la recherche dans cette dissertation rapporte également, pour la première fois, une émission laser UV profonde provenant d'AlGaN développé par MBE sur saphir par pompage optique, avec des preuves claires d’émission laser. Une émission laser à 298 nm à partir de la double hétérostructure (DH) AlGaN/AlN est d'abord obtenue, avec un seuil de d’émission laser de 950 kW/cm^2. Cette recherche étudie également la corrélation entre les défauts ponctuels et le seuil d’émission laser, réduisant le seuil à 530 kW/cm^2 à 287 nm, accompagné d'une augmentation de l'IQE d'environ 16%. En vue de diodes laser UV en AlGaN à injection électrique, la recherche de cette dissertation conçoivent et étudient numériquement une unique couche de blocage d'électrons à super réseau avec composition d'Al ajustée (AESL-EBL), qui améliore non seulement le transport des porteurs de charge avec l'aide des effets de trous chauds, mais minimise également les pertes optiques dues au dopage.

Table of Contents

Acknowledgement

Pursuing this Ph.D. has been a fresh and life-changing experience for me, and I will never regret this memorable journey. I would like to sincerely thank every individual who helped, supported, and accompanied me in the past four years.

First and foremost, I would like to express my deepest gratitude to my supervisor, Prof. Songrui Zhao, who offered me the first key to the door of research and funded me on various fantastic training. His passion for science and immense knowledge greatly influenced me. He has provided almost 24/7 support and kind understanding whenever I faced bottlenecks in my research and life. Without his patient guidance and help, this doctoral dissertation would never have existed.

I would also like to extend my appreciation to my lab mates, Jiaying Lu, Qihua Zhang, Mohammadfazel Vafadar, Heemal Parimoo, Wenqi Liang, and Yun Zhong, for their research support and shared valuable experience. Many thanks to my peers, David Guan, for helping translate this abstract into French, as well as Md Mahadi Masnad and Essam Radwan Berikaa, for their encouragement in my daily life.

Continuing on the academic side, I am also grateful to Prof. Thomas Szkopek and Eli Martel at McGill University for their support on the AFM facility; Dr. Hatem Titi at McGill University as well as Dr. Patrick Daoust, Dr. Jérôme Nicolas, and Zeinab Abboud at Polytechnique Montréal for their assistance on XRD. Special thanks to all the supporting staff from McGill Nanotools Microfab, SEM, and TEM facilities for their patient training and guidance.

I would like to thank Prof. Odile Liboiron-Ladouceur and Prof. Thomas Szkopek for serving as my committee members and providing valuable comments and suggestions on my research proposal and seminar.

Finally, my acknowledgement would be incomplete without thanking to my parents and my husband, Xingyu Li. Their unconditional love and dedicated support are what sustained me this far.

This work was supported by Natural Sciences and Engineering Research Council of Canada (NSERC) and Fonds de Recherche du Quebec – Nature et Technologies (FRQNT).

Contribution of Authors

Throughout this dissertation work, the candidate and her supervisor, Prof. Zhao, contributed together to the project definition, experiments, and manuscript writing. Overall, the candidate carried out the MBE growth, PL, STEM, XRD, and AFM experiments, theoretical modeling, and result analyses. Chapter 3 to Chapter 7 are based on referred journal publications. Below describes the contribution of the candidate to these chapters *experimentally and theoretically*: For Chapter 3, the candidate conducted MBE growth and PL experiment jointly with Prof. Zhao and communicated with Dr. Titi for XRD experiments. The wet etching experiments were performed by Qihua Zhang. The STEM studies were carried out by Prof. Zhao. For Chapter 4, the candidate conducted MBE growth jointly with Prof. Zhao, and PL experiments and IQE analysis nearly independently, with advice from Prof. Zhao. The SEM studies were carried out by Prof. Zhao. XRD experiments were carried out by Dr. Titi. For Chapter 5, the candidate and Prof. Zhao jointly performed the experiments and results analysis. This is the first journal publication of the candidate. For Chapter 6, the candidate conducted MBE growth, optical experiments, and results analysis, assisted by Prof. Zhao. For Chapter 7, the candidate dominated the research, with suggestions from Prof. Zhao.

List of Table

List of Figures

List of Acronyms

2D	Two Dimensional
3D	Three Dimensional
AESL-EBL	Al-content Engineered Superlattice Electron Blocking Layer
AlGaN	Aluminum Gallium Nitride
AlN	Aluminum Nitride
APSYS	Advanced Physical Models of Semiconductor Devices
BEBL	Bulk Electron Blocking Layer
C	Conduction
Ca	Calcium
CH	Crystal-Field Split-Off
CW	Continuous-Wave
DAP	Donor-to-Acceptor Pair
DH	Double Heterostructure
DI	Deionized
DPD	Distributed Polarization Doping
DPSS	Diode-Pumped Solid State
DUV	Deep Ultraviolet
EBL	Electron Blocking Layer
EL	Electroluminescence
ELO	Epitaxial Lateral Overgrowth
FIB	Focused Ion Beam

FWHM	Full Width at Half Maximum
GEBL	Graded Electron Blocking Layer
GSL-EBL	Graded Superlattice Electron Blocking Layer
HAADF	High-Angle Annular Dark-Field
HEMTs	High Electron Mobility Transistors
HH	Heavy-Hole
InGaN	Indium Gallium Nitride
IPL	Integrated PL Intensity
IQE	Internal Quantum Efficiency
ITL	Intermediate Tunneling Layer
KOH	Potassium Hydroxide
LEDs	Light-Emitting Diodes
LEO	Lateral Epitaxial Overgrowth
LDs	Laser Diodes
LH	Light-Hole
L-L	Light Input-Light Output
LQB	Last Quantum Barrier
LQW	Last Quantum Well
LT	Low Temperature
MBE	Molecular Beam Epitaxy
MEMS	Microelectromechanical Systems
Mg	Magnesium
MOCVD	Metalorganic Chemical Vapor Deposition

MOVPE	Metalorganic Vapor Phase Epitaxy
MQWs	Multiple Quantum Wells
N	Nitrogen
ND	Neutral Density
NLOS	Non-Line-Of-Sight
PAMBE	Plasma-Assisted Molecular Beam Epitaxy
PICS3D	Photonic Integrated Circuit Simulator in 3D
PL	Photoluminescence
PLD	Pulsed Laser Deposition
Pt	Platinum
QCSE	Quantum-Confined Stark Effect
QW	Quantum Well
RF	Radio-Frequency
RHEED	Reflection High-Energy Electron Diffraction
RIE	Reactive Ion Etching
RT	Room Temperature
SAG	Selective-Area Growth
SAW	Surface Acoustic Wave
SEM	Scanning Electron Microscopy
Si	Silicon
SLs	Superlattices
SL-EBL	Superlattice Electron Blocking Layer
SOI	Silicon-On-Insulator

SPSLs	Short-Period Superlattices
SRH	Shockley-Read-Hall
STEM	Scanning Transmission Electron Microscopy
TDDs	Threading Dislocations Densities
TE	Transverse Electric
TJs	Tunnel Junctions
TM	Transverse Magnetic
UHV	Ultrahigh Vacuum
UV	Ultraviolet
WZ	Wurtzite
XRD	X-Ray Diffraction
ZB	Zinc Blende
Zn	Zinc

Chapter 1

Introduction

1.1 Motivation

The development of UV LDs is of great research interest because of their promising and wide range of applications, including non-line-of-sight (NLOS) communications, UV curing, water sterilization, high-density data storage, medical diagnostics, just to mention a few [1-9]. **Figure 1.1** gives an overview of the potential applications in terms of various UV wavelengths, divided into UVA (400-315 nm), UVB (315-280 nm), and UVC (280-200 nm) bands.

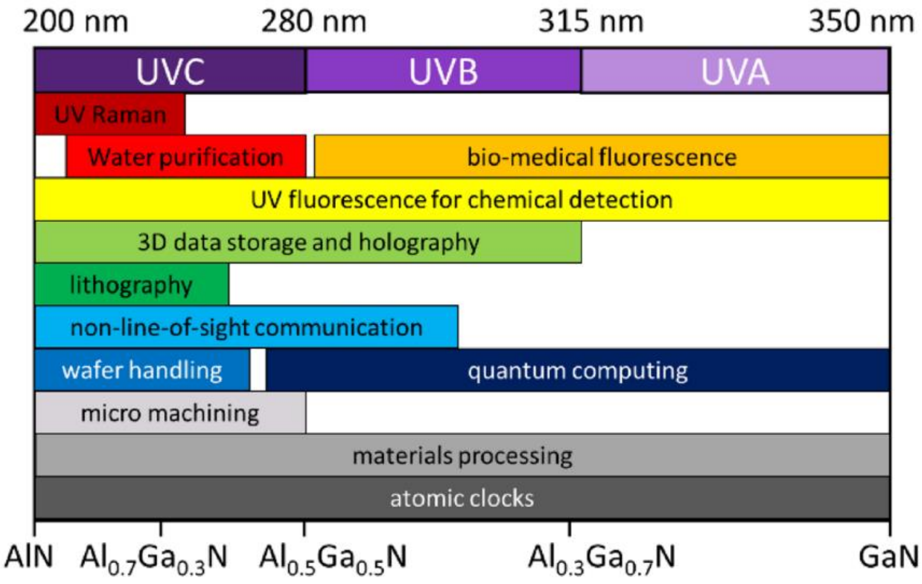

Figure 1.1. Applications of AlGaN-based UV LDs. Reproduced with permission [9]. Copyright 2021, Springer Nature.

Today, the dominant UV lasing technologies mainly rely on gas lasers and solid-state lasers [1, 4, 7, 8]. They not only contain environmental hazards (e.g., fluoride) but are also bulky, high-power consuming, and have limited lifetime as well as non-tunable wavelengths. Compared to conventional UV laser sources, semiconductor UV LDs offer several advantages, such as compact size, lower power consumption and higher efficiency, robust against vibrations, longer lifetime, environment-friendly, mass fabrication, more versatile in terms of emission wavelengths, and portability [9, 10].

Among various semiconductor candidates, AlGaN alloys in the III-nitride material system are considered as the most promising candidate to develop semiconductor UV LDs, due to their direct, ultrawide, and tunable bandgap energies, ranging from 3.4 eV (GaN) to 6.2 eV (AlN) that could cover nearly the whole UV range by tailoring the Al alloy compositions [1-8].

LDs emitting in the deep UV range, e.g., wavelengths < 300 nm, would be grown mainly based on Al-rich AlGaN, whereas those with longer emission wavelengths (> 300 nm) would be grown mainly based on Ga-rich AlGaN. Compared to UVA LDs, deep UV LDs show more diverse applications, as reflected in **Figure 1.1**. Especially for their applications in water purification, UV lithography, NLOS, and micro machining, where high power densities are needed [9]. Therefore, significant research efforts have been put into developing AlGaN deep UV lasers by both optical pumping and electrical injection. Compared to optically pumped AlGaN deep UV lasers, the progress on the development of electrically driven counterparts is relatively slow. The electrically injected AlGaN UV lasing wavelengths have been limited in the UVA range, i.e., no deep UV lasing, until 2019 [11-18].

The main impediments to the development of AlGaN UV lasers mainly root in the poor material quality of AlGaN epilayers grown on lattice-mismatched foreign substrates with high dislocation densities (TDDs) and the difficulties in achieving sufficient p-type conduction due to the large Mg activation energy and co-doping effects. Therefore, the majority of the studies on AlGaN deep UV lasers today are still on optical pumping. The optically-pumped AlGaN UV lasers could be used to examine not only the material quality of AlGaN epilayers but also the corresponding laser design parameters. It is also worth noting that, at the time of writing this dissertation, the AlGaN UV laser research, no matter by optically pumping or electrical injection, predominantly relies on the structures grown by MOCVD. The studies of AlGaN UV lasers with MBE-grown structures are rare.

1.2 Fundamental Properties of AlGaN Alloys

III-nitride compound semiconductors, including InN, GaN, and AlN, have three crystal structures: hexagonal wurtzite (WZ), zinc blende (ZB), and rock-salt. All the III-nitrides in this thesis study have the WZ structure, which is the most stable crystal structure of III-nitrides [5]. **Figure 1.2** shows the band energies of WZ III-nitrides, ranging from 0.7 eV in InN, 3.4 eV in GaN, to 6.2 eV in AlN. Moreover, they are direct bandgap materials, which are suitable for developing light emitters due to their fast radiative recombination rate. In this project, we mainly focus on the deep UV LD light emitters with high Al-content AlGaN.

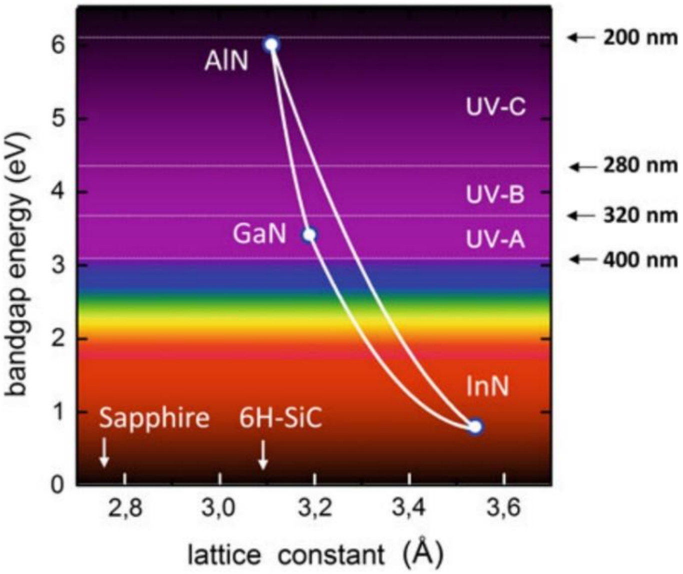

Figure 1.2. III-nitride material system. Reproduced with permission [19]. Copyright 2016, Springer Nature.

The Al composition of AlGaN alloys could be estimated via Vegard's law using photoluminescence (PL) measurements,

$$E_g(Al_xGa_{1-x}N\ ) = (1-x)\cdot E_g(GaN) + xE_g\cdot(AlN) - x(1-x)C_B, \qquad (1.1)$$

where x is the Al composition, $E_g(Al_xGa_{1-x}\mathrm{N}\ )$ is the PL peak position under low excitation, $E_g(GaN)$ and $E_g(AlN)$ are the respective bandgap energies of GaN and AlN, and C_B is the bowing parameter, which is typically in the range of 0.6 to 1.3 eV [20]. In the dissertation, C_B of 0.7 eV is used for WZ AlGaN [20].

Moreover, WZ AlGaN are tetrahedrally coordinated semiconductors with two different polarities, including group-III polarity and N polarity. The unit cell of the WZ structure with group-III polarity is shown in **Figure 1.3 (a)** as an example, which contains two group-III atoms and two nitrogen (N) atoms [21]. The Ga(Al)-face and N-face tetrahedral WZ structures are shown in

Figure 1.3 (b) and **(c)**, respectively, consisting of hexagonal close-packed group-III atoms and N atoms stacking up on each other. Such WZ crystal structure could be defined by the lattice constants *a* and *c*, and a microscopic dimensionless parameter *u* that denotes the length of the bond parallel to the $\vec{c}$-axis. The angle between *a* axes is 120°, and that between *a* and *c* axes is 90°. The ideal WZ crystal has lattice constant ratios of c/a=1.633 and u/c=0.375 [22], respectively. The lattice constant of WZ AlGaN could be calculated based on Vegard's law,

$$a_{AlGaN} = a_{AlN} \cdot x + a_{GaN} \cdot (1 - x), \tag{1.2}$$

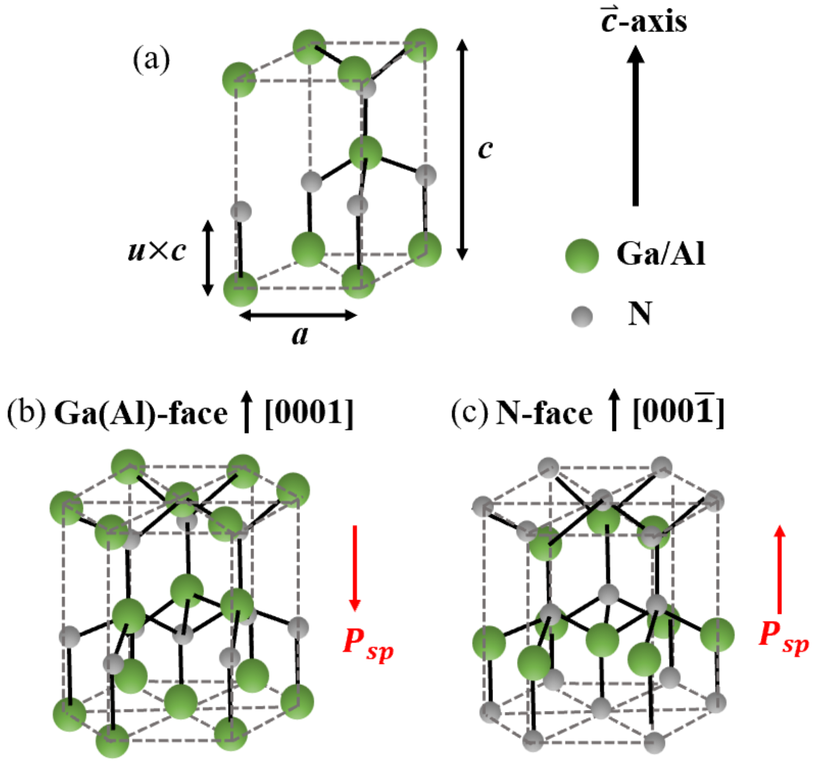

Figure 1.3. (a) The Al(Ga)N WZ unit cell structure with group-III polarity. The WZ structure of Al(Ga)N with (b) group-III polarity and (c) N polarity, respectively. Note that the growth directions related to (b) and (c) are along the $\vec{c}$-axis.

The noncentrosymmetry of the WZ structure results in a unique spontaneous polarization (P_{sp}), which can exist even without strain. For example, in a Ga(Al)-face WZ structure that is grown with Ga top, as reflected in **Figure 1.3 (b)**, each N atom is tetrahedrally bound to four Ga atoms. Due to the large electronegativity of N than Ga, it can be considered that the N and Ga atoms exhibit respective anionic and cationic characteristics. This results in total electric dipole moments along the $[000\bar{1}]$ direction. As a result, strong P_{sp} occurs in the same direction along the $[000\bar{1}]$ direction, marked by the red arrow in **Figure 1.3 (b)**. Vice versa, the N-face WZ structure is grown with N top, but P_{sp} is also along the $[000\bar{1}]$ direction, as shown in **Figure 1.3 (c)**. However, it is noted that the growth directions related to **Figure 1.3 (b)** and **(c)** are all along the $\vec{c}$-axis, so P_{sp} is flipped with respect to the $\vec{c}$-axis.

For WZ AlGaN alloys, taking group-III polarity as an example, the P_{sp} (in C/m^2) can be expressed as [23, 24],

$$P^{sp}_{Al_xGa_{1-X}N} = P^{sp}_{AlN} \cdot x + P^{sp}_{GaN} \cdot (1-x) + 0.019x(1-x), \tag{1.3}$$

where the first two terms in Equation (1.3) are the linear interpolation of P_{sp} between AlN and GaN, where P^{sp}_{AlN}= -0.09 C/m^2 and P^{sp}_{GaN} = -0.034 C/m^2. The negative values of P_{sp} indicate that the directions of P_{sp} are in the opposite direction of the $\vec{c}$-axis [21, 24]. The last term is the so-called bowing, and the higher-order terms are neglected.

Besides P_{sp}, the WZ AlGaN alloys can also show the piezoelectric polarization (P_{pz}), resulting from the tensile and compressive strain (ε) due to the lattice mismatch between different epitaxial materials. The basal strain can be expressed as follows [21, 23],

$$\varepsilon(x) = \left[a_{buffer} - a(x)\right]/a(x), \tag{1.4}$$

where a_{buffer} and $a(x)$ are the *a* lattice constants of the unstrained GaN (or AlN) buffer layer and AlGaN epilayer grown on top, respectively.

Similarly, such P_{pz} (in C/m^2) of WZ AlGaN alloys can be expressed as,

$$P^{pz}_{Al_xGa_{1-x}N} = P^{pz}_{AlN} \cdot x + P^{pz}_{GaN} \cdot (1 - x), \tag{1.5}$$

where P^{pz}_{AlN} and P^{pz}_{GaN} are the strain-dependent bulk P_{pz} of AlN and GaN. Based on Equation (1.4) and taking the case of unstrained GaN buffer as an example, P_{pz} of strained AlN and relaxed GaN grown on top can be represented as follows [25],

$$P^{pz}_{AlN} = -1.808\varepsilon + 5.624\varepsilon^2 \text{ for } \varepsilon < 0,$$
$$P^{pz}_{AlN} = -1.808\varepsilon - 7.888\varepsilon^2 \text{ for } \varepsilon > 0, \tag{1.6}$$
$$P^{pz}_{GaN} = -0.918\varepsilon + 9.541\varepsilon^2.$$

In terms of group-III polarity AlGaN, when the AlGaN epilayer is under compressive strain (ε < 0), P_{pz} is oriented along the $\vec{c}$-axis direction; when the AlGaN epilayer is under tensile strain (ε >0), P_{pz} is pointing towards the opposite direction of the $\vec{c}$-axis. If the polarity flips to N polarity, the P_{pz} changes its signs accordingly. **Figure 1.4** demonstrates the signs of P_{pz} for strained and relaxed AlGaN/GaN heterostructures, with respective group-III and N polarity, as an example [26]. In addition, the corresponding polarization induced sheet charge densities (σ) at the interface are also presented.

The total polarization of WZ AlGaN alloys is the sum of P_{sp} and P_{pz} :

$$P^{Total}_{Al_xGa_{1-x}N} = P^{sp}_{Al_xGa_{1-x}N} + P^{Pz}_{Al_xGa_{1-x}N}. \tag{1.7}$$

The corresponding WZ AlN and WZ GaN parameters used in the dissertation can be found in Ref. [20]. The application of the unique electric polarization properties of III-nitrides will be discussed in Chapter 7.

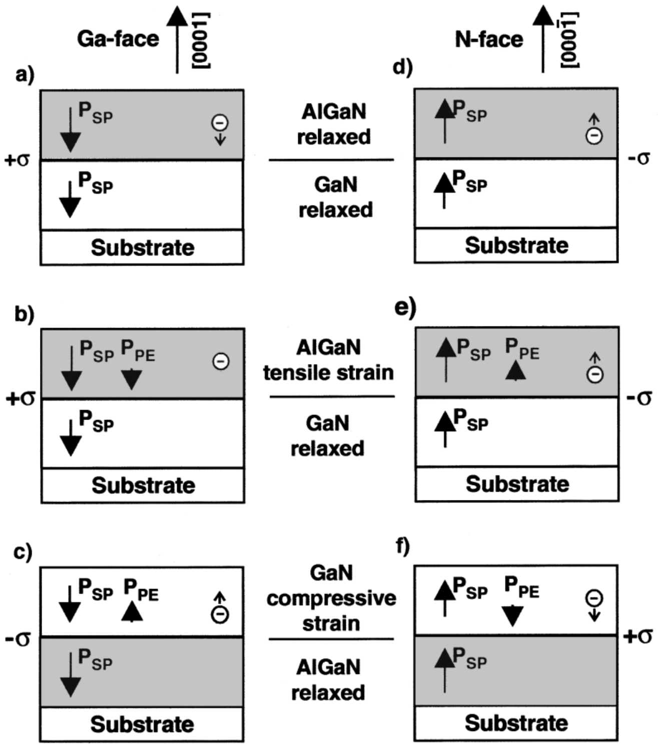

Figure 1.4. Directions of spontaneous and piezoelectric polarization of strained and relaxed AlGaN/GaN heterostructures with respective group-III and N polarities, together with the polarization induced sheet charge density at the interface labeled. Reproduced with permission [26]. Copyright 1999, AIP Publishing.

1.3 Molecular Beam Epitaxy of AlGaN

In the 1960s, Bruce Joyce and co-workers at Plessey Labs deposited homoepitaxial Si films using the molecular beam of saline on heated Si (111) substrates [27-29]. In the 1970s, the term “molecular beam epitaxy” was created by Cho *et al.* in the *Proceedings of the Third International Symposium on GaAs and Related Compounds* [30, 31], which denotes the compound semiconductor epitaxial growth process that involves the reaction of multiple thermal molecular beams at crystalline surface under an ultrahigh vacuum (UHV) environment.

Since then, MBE has been widely used in compound semiconductor growth, including group-IV, group III-V, group II-VI, and group-III nitride materials. Today, two major types of MBE systems have been used for III-nitrides, i.e., ammonia MBE and plasma-assisted MBE (PAMBE). The difference lies in their way of generating active N species, where the former uses ammonia gas injectors and the latter uses plasma sources.

1.3.1 MBE in this Thesis Study

In this project, we used the Veeco GENxplor PAMBE system, and the corresponding schematic is shown in **Figure 1.5**. The MBE system contains three vacuum chambers, including a load lock chamber, a buffer chamber, and a growth chamber. Cleaned wafers are loaded into/taken out of the load lock chamber. A buffer chamber is a “buffer” between the load lock chamber and the growth chamber, as suggested by its name. Wafer outgas is performed in the buffer chamber, in order to maintain the UHV environment of the growth chamber.

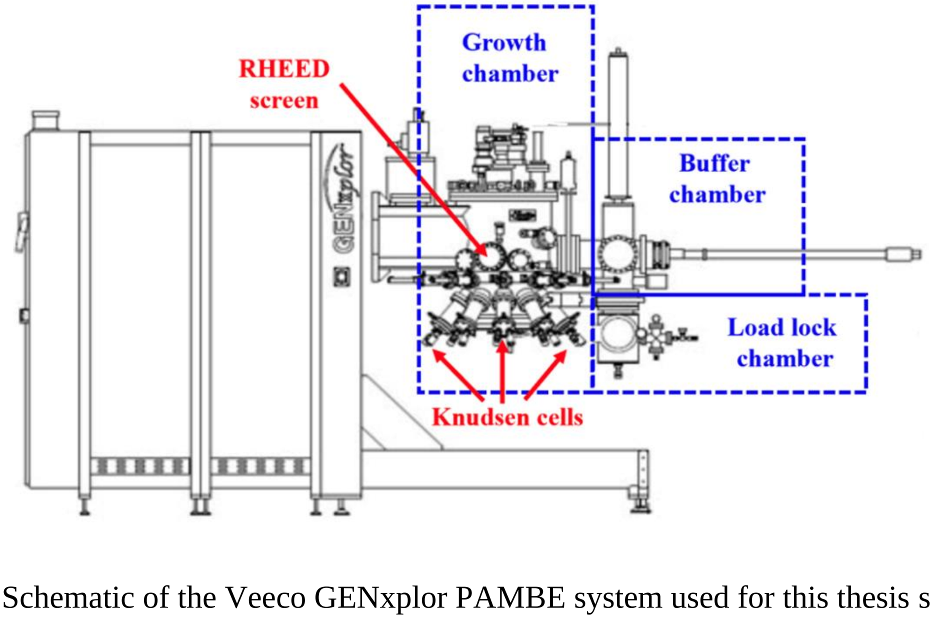

Figure 1.5. Schematic of the Veeco GENxplor PAMBE system used for this thesis study [32].

Regarding III-nitride growth, the group-III metal sources are provided from crucibles in the Knudsen cells, from where the materials are thermally evaporated as molecular/atomic beams onto the rotated and heated substrate surface to form semiconductor epitaxial layers. The active N species are provided via the radio-frequency (RF) plasma nitrogen source.

In addition, reflection high-energy electron diffraction (RHEED) is used for *in situ* monitoring during the growth. **Figure 1.6** demonstrates the schematic diagram of the RHEED geometry. The RHEED gun emits high-energy electrons that strike on the wafer surface at a low angle of around 0.5-2.5°. Then, the diffracted electrons strike on a phosphor screen and form the RHEED pattern, through constructive interference. It is also noted that electrons could only penetrate a few Å into the sample, thus RHEED is more surface sensitive. To date, RHEED is considered as one of the most important *in situ* monitoring methods and widely used to calibrate the growth condition in real time via the feedback shown on the phosphor screen for the surface morphology.

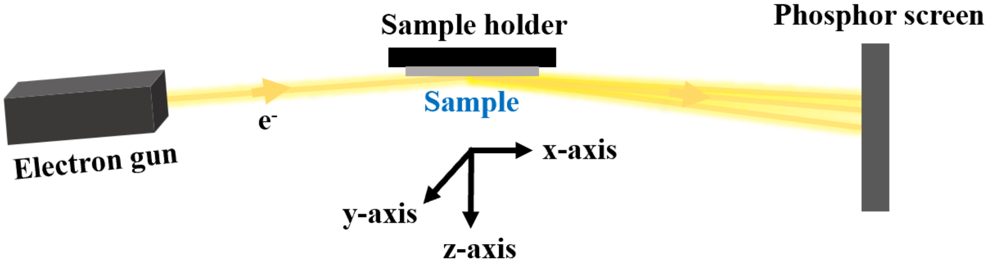

Figure 1.6. Schematic diagram of the RHEED geometry.

1.3.2 Advantages of MBE for AlGaN

As mentioned earlier, the majority of UV AlGaN lasers are developed by MOCVD, and the research on AlGaN UV lasers by MBE is rare. Compared to MOCVD, MBE offers several advantages in terms of AlGaN epilayer growth.

First, MBE system typically operates under the UHV environment (base pressure of 10^{-11} to 10^{-12} Torr), which could minimize any impurity incorporation. Moreover, the use of ultrahigh purity source materials (6N5 and above) further reduces potential impurity incorporation.

Second, MBE is able to control the substrate and each source temperatures separately, which can provide excellent control on the heterointerface properties. Furthermore, recent studies also suggest that MBE may favor p-type dopant, magnesium (Mg), incorporation [33, 34], which is beneficial for electrically injected light-emitting devices with high Al-content AlGaN alloys. Unlike MOCVD and other growth techniques, MBE growth of AlGaN epilayers only requires a substrate growth temperature of around 800 ℃ [35-39], whereas MOCVD technique usually needs higher temperatures of 1000-1200 ℃ [15, 16, 40, 41].

Furthermore, the MBE system contains a unique RHEED component that allows *in situ* growth monitoring, whereas MOCVD does not have such an *in situ* growth monitoring capacity. Patterns obtained from RHEED in general can be correlated to the surface properties of the grown AlGaN epilayers; therefore, monitoring RHEED patterns allows instantaneous adjustment of the growth parameters. For example, for AlGaN epilayers grown under metal-rich conditions, when the growth enters strongly metal-rich conditions (droplet regime, metal/N flux ratio >> 1), Ga droplets could be formed on the wafer surface due to excess metal flux accumulation. This yields a dim RHEED pattern with hardly visible streaks due to the coverage of metal droplets [42]. However, other reasons could also lead to the dim RHEED pattern. On the other hand, N-rich conditions (metal/N flux ratio < 1) typically yield pitted and rough surface morphologies and correlate to spotted RHEED patterns, suggesting the possible existence of a three-dimensional (3D) growth mode [43]. However, it should be noted that N-rich conditions can also produce relatively smooth III-nitride epilayers. Lastly, it is worth noting that despite the convenience of the RHEED monitoring during the epitaxy process, due to the complexity of RHEED patterns, thorough analysis is often required in order to adjust parameters properly.

1.4 Contributions of this Thesis Work

In this dissertation, we follow the track of MBE-grown AlGaN on foreign substrates, such as Si and sapphire. For AlGaN on Si, the shortest wavelength of electrically injected lasing is still in the near UV regime, with lasing wavelength at around 390 nm [44], due to fundamental material challenges (discussed in Chapter 2). The research in this dissertation demonstrates a novel method of growing AlN thin films on Si, through exploiting the low Al adatom migration and the N-rich environment on a GaN nanowire template [45], which improves the material quality for AlN on Si and provides high quality templates for AlGaN epilayers on top. The research in this dissertation further demonstrates MBE-grown AlGaN epilayers on Si using such nanowire-assisted AlN template on Si and UV light emission on Si [46]. To understand the optical quality of such AlGaN epilayers, a systematic study on the IQE is carried out. Compared to the IQE of bulk AlGaN epilayers on sapphire, the IQE of AlGaN epilayers presented in this thesis work is significantly improved.

The research in this dissertation also demonstrates, for the first time, deep UV lasing from MBE-grown AlGaN on sapphire, with clear lasing evidence. The lasing wavelength is around 298 nm, with a lasing threshold of 950 kW/cm^2 [47]. The research in this dissertation further studies the correlation between point defects and lasing threshold, reducing the lasing threshold to 530 kW/cm^2 at 287 nm [48]. Towards the electrically injected laser devices, the research in this dissertation further proposes a novel AESL-EBL, which can not only improve the carrier injection into the device active region but also minimize the optical loss related to doping.

1.5 Thesis Outline

Chapter 1 provides an introduction to the fundamental properties of AlGaN alloys, MBE system and advantages of MBE for AlGaN, as well as the motivation of this thesis study. Chapter 2 provides a literature review of the state-of-the-art AlGaN lasers by both optical pumping and electrical injection, and the underlying challenges including material quality, p-type doping, optical and carrier confinement, transverse electric (TE)/transverse magnetic (TM) polarization, and difficulties related to device fabrication.

Chapter 3 and Chapter 4 describe the high quality nanowire-assisted AlN template on Si and IQE study of AlGaN epilayers on Si using such AlN templates. These studies are published in *Crystal Growth & Design* and *ECS Journal of Solid State Science and Technology*, respectively. Chapter 5 and Chapter 6 demonstrate optically pumped 298 nm and 287 nm AlGaN DH lasers on sapphire substrates, respectively; and both are published in *Physics Status Solidi B*. In Chapter 7, the design of AESL-EBL on improving the carrier transport for the electrically injected AlGaN deep UV lasers on sapphire is presented. The work is published in *IEEE Journal of Quantum Electronics*. Chapter 8 concludes this thesis and discusses the further work.

Chapter 2

Overview of AlGaN UV Lasers

2.1 Current Status of AlGaN UV Lasers

The research on III-nitride UV lasers started in the 1970s [5, 49]. The first stimulated emission was achieved from the single-crystal needles of GaN at low temperature (LT) by Dingle *et al.* in 1971 [50]. Further using GaN thin films, room temperature (RT) lasing was demonstrated by Amano *et al.* in 1990 [50, 51]. Later on, tremendous efforts have been put into developing optically pumped AlGaN UV lasers on sapphire [52-68] and AlN [69-75]. Significant progress has been made, with AlGaN grown by both MOCVD and MBE. As shown in **Figure 2.1**, to date, the lasing thresholds of optically pumped AlGaN UV lasers have been successfully reduced to as low as 6 kW/cm^2 on native AlN substrates [69, 70], and to around 100 kW/cm^2 on sapphire [53, 58, 63, 64].

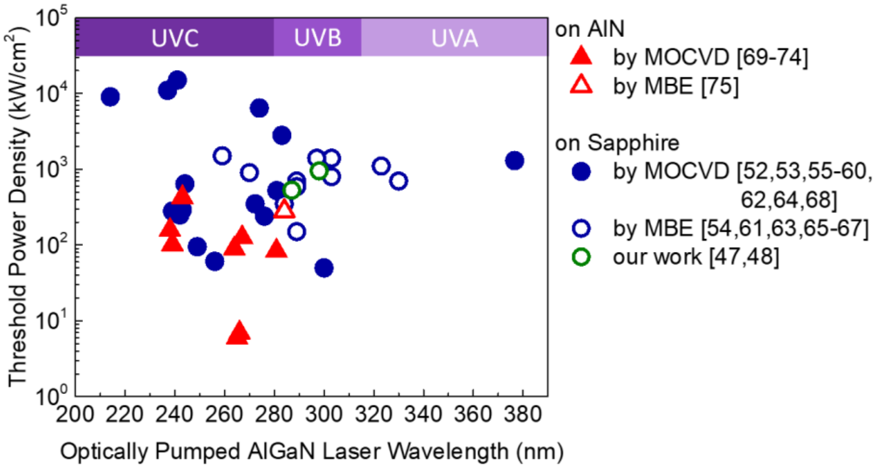

Figure 2.1. The threshold power density of optically pumped AlGaN thin-film UV lasers as a function of the lasing wavelength on AlN [69-75] and sapphire [52-68], respectively.

In contrast, the development of the electrical injected AlGaN UV LDs is much slower. The first violet III-nitride LD was realized by Nakamura *et al.* in 1996 [76]. Since then, Akasaki *et al*. reported the first UV indium gallium nitride (InGaN) LD in 1996 with a lasing wavelength of 376 nm [51], and Nakamura *et al.* further fabricated the first GaN UV LD in 2001, lasing at 366.9 nm [77]. The shortest wavelength of AlGaN electrically driven LDs had been stuck in the UVA range (336 nm) [16] for a decade until the recently reported 271.8 nm deep UV lasers on AlN substrates in 2019 [18]. Later on, although various techniques have been developed to solve the challenges for AlGaN deep UV LDs (discussed in detail in Section 2.2), the threshold current density was still relatively high compared to blue LDs and limited to above 10 kA/cm^2. Moreover, continuous-wave (CW) AlGaN LDs were only achieved in the UVA range [11, 78-80].

It was not until very recently (2022) that the first LT and RT CW operation of deep UV AlGaN LDs were reported by Zhang *et al.* using AlN substrates, with lasing wavelengths at 274.8 nm and 274 nm, respectively [81, 82]. The corresponding threshold current densities were further reduced to 3.7 kA/cm^2 and 4.2 kA/cm^2, respectively [81, 82]. **Figure 2.2** summarizes the lasing wavelength of electrically injected AlGaN UV LDs as a function of the threshold current density in different UV ranges. *It is also worth noting that these developments are all based on MOCVD-grown AlGaN laser structures*.

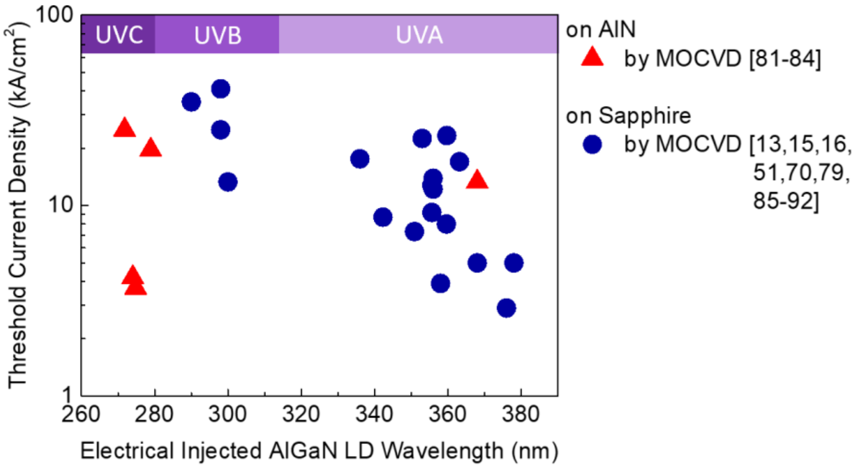

Figure 2.2. The threshold current density of the electrical injected AlGaN thin-film UV lasers as a function of the lasing wavelength on AlN [81-84] and sapphire [13, 15, 16, 51, 70, 79, 85-92], respectively. Note: AlGaN nanowire UV lasers are not shown in this plot.

2.2 Key Challenges for AlGaN Deep UV Lasers

In this section, several key impediments in the development of AlGaN deep UV lasers are discussed, including the poor material quality, difficulties in p-type doping, low electrical and optical confinement, TE/TM polarization, as well as device fabrication challenges. Among those, most of the challenges are originated from the intrinsic properties of AlGaN alloys.

2.2.1 Substrates

To realize deep UV AlGaN LDs, high crystalline quality AlGaN epilayers are necessary to support light propagation, confinement, and charge carrier injection into active regions. To date, the majority of the current AlGaN deep UV LDs were achieved either on native AlN substrates or on sapphire substrates. As mentioned earlier in section 2.1, the lowest lasing thresholds of AlGaN deep UV lasers, both under optical pumping [69] and electrical injection [81], were realized on native AlN substrates. This is mainly attributed to the relatively small lattice mismatch (~2.4%) between AlGaN epilayers and AlN substrate, as well as the availability of AlN substrates with low TDDs (<10^4 cm^{-2}) [93], contributing to the growth of high quality Al-rich AlGaN epilayers. Nevertheless, such native AlN substrates are extremely costly with a limited wafer size (2 inches) [10], making them impractical for mass fabrication, at least at the time of this thesis writing.

Compared to the widely used sapphire and AlN substrates, Si substrates offer a few advantages, such as low cost, large wafer size (12 inches), excellent electric and thermal conductivity, Si-based electronics integration, as well as mature processing technologies [94, 95]. Therefore, it is still of great interest to develop AlGaN deep UV lasers on Si. Nonetheless, to date, there has been no deep UV laser demonstration on Si using AlGaN epilayers. This is mainly limited by the large lattice mismatch between hexagonal high Al-content AlGaN alloys and Si (111), among others. The comparison of AlN, sapphire, and Si substrates is listed in **Table 1** [10, 96].

Table 1. Comparison of AlN, sapphire, and Si substrates [10, 96].

	a-axis (Å)	*c*-axis (Å)	Mismatch to GaN	Mismatch to AlN	Thermal conductivity ($Wcm^{-1}K^{-1}$)	UV transparency	Price
AlN	3.112	4.982	2.4%	0%	2.1	Yes	$$$$
Sapphire	4.765	12.982	16%	13%	0.23	Yes	$$
Si	3.840	3.136	17%	19%	1.6	No	$

In general, the large lattice mismatch between the foreign substrates, such as sapphire and Si, and AlGaN epilayers, could lead to high TDDs of 10^{10} cm^{-2} [97] in the AlGaN epilayers and even crack formation [98-101], particularly the case for AlGaN grown on Si substrates.

Consequently, the optical and electrical performance of the device will be significantly degraded. As shown in **Figure 2.3**, a reduction in TDDs, acting as nonradiative recombination centers, could lead to a dramatic increase in the IQE of AlGaN multiple quantum wells (MQWs) on sapphire substrates, which is critical to the realization of highly efficient and low threshold deep UV AlGaN lasers.

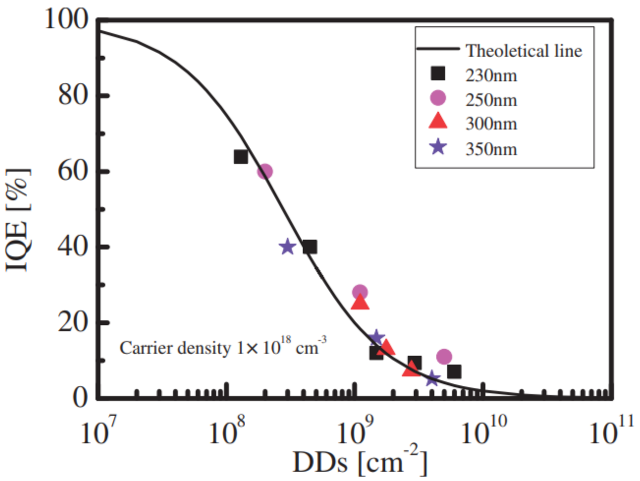

Figure 2.3. IQE of AlGaN MQWs on sapphire substrates as a function of dislocation densities at low excitations with a carrier density of 1×10^{18} cm^{-3}. The solid line is the theoretical curve calculated by the model described in Ref. [102]. Reproduced with permission [97]. Copyright 2008, IOP Publishing.

Therefore, researchers have developed various approaches to reduce TDDs, in order to achieve high crystalline quality AlGaN epilayers, including the utilization of AlN buffer layers [44, 53, 58, 61, 66, 94], introducing superlattices [58, 63, 66, 95, 101, 103] and graded AlGaN buffer layers [44, 53, 104], lateral epitaxial overgrowth (LEO) [62, 105, 106], and implementation of patterned substrates [68, 106-109]. Consequently, the TDDs of AlGaN epilayers on sapphire and Si substrates have been successfully reduced to the low-10^8 cm^{-2} [61, 105, 110] and mid-10^8 cm^{-2} [44, 111] ranges, respectively.

Apart from the TDDs reduction, controlling point defects is equally important. Point defect act as a radiative recombination center and could be a more severe issue, especially for AlGaN deep UV lasers with high Al compositions. It has been reported that an increase in impurity incorporation and native defect generation, e.g., vacancies, is observed along with the increase in Al composition [2, 112-116]. By controlling point defects, Kirste *et al.* have successfully achieved the lowest threshold (6 kW/cm^2) AlGaN deep UV lasing on native AlN substrate under optical pumping [69].

2.2.2 N- and P-type Doping for Al-rich AlGaN

Highly conductive n- and p-type AlGaN epilayers are essential to achieve high current density in order to reach population inversion for lasing. Therefore, the electrical doping of AlGaN epilayers has been intensively studied in the past decades. Si is the most commonly used n-type dopant for III-nitrides, which provides a relatively low donor ionization energy (E_d), only increasing slightly from ~15 meV in GaN to ~50 meV in AlGaN epilayers with Al contents below 0.8 [2, 117]. Accordingly, the highest electron concentration up to around 4×10^{19} cm^{-3} has been achieved in n-AlGaN ($x < 0.8$) by both MOCVD [118] and MBE [119], together with resistivities of around 3-4 mΩ·cm and electron mobilities of around 40-50 cm^2/Vs.

Nevertheless, once the Al content in AlGaN exceeds 0.8, E_d experiences a drastic increase to around 300 meV in AlN [2, 117]. This phenomenon is partially ascribed to the formation of DX centers (a donor-defect complex that undergoes a large lattice relaxation [120]), with formation energy increases from 63 meV for $x = 0.79$ to 240 meV for $x = 1$ [121, 122], leading to a drastic increase in the resistivity of n-AlGaN for $x > 0.8$, which makes it especially challenging for the development of AlGaN deep UV lasers with lasing wavelength below 250 nm.

Achieving sufficient p-type conduction in AlGaN epilayers is even more challenging. Mg is the most commonly used p-type dopant for III-nitrides. Although its acceptor ionization energy (E_a) is smaller compared to other p-type dopants, such as Zinc (Zn) and Calcium (Ca), a large energy is still needed to activate Mg dopant. The E_a of Mg typically increases with the Al composition, ranging from ~200 meV in GaN to ~500 meV in AlN [123, 124]. Consequently, only a small fraction of Mg generates free holes, especially in the case of Al-rich AlGaN, leading to poor p-type conduction at RT. In most literatures, the reported RT hole concentrations from Al-rich bulk AlGaN films are in general still below 10^{18} cm^{-3}, together with resistivity values in the range of tens to thousands of Ω·cm and low mobility values on the order of 1-3 cm^{2}/Vs [125-129].

Various solutions have been explored to improve hole concentrations of Al-rich AlGaN. One approach is to introduce Mg-doped short-period superlattices (SPSLs) [130]. Hole concentrations as high as around 3.4×10^{18} cm^{-3}, resistivity of 6.5 Ω·cm, and mobility around 0.3 cm^{2}/Vs have been achieved in AlN/ $Al_{0.75}Ga_{0.25}N$ SLs with a high average Al content of 0.8 [130]. Another method, widely implemented in AlGaN LDs, is the distributed polarization doping (DPD) method [131, 132]. Hole concentrations of 4.2×10^{17} cm^{-3} and 4.5×10^{18} cm^{-3} have been achieved in the undoped-DPD layer with average Al content of 0.86 [132] and Mg-doped DPD layer with average Al content of 0.68 [131], respectively. Recently, interface doping effect has also been studied in p-type AlGaN [133, 134]. A low resistivity of 6.94 Ω·cm, with hole concentration of 1.52×10^{18} cm^{-3} and mobility of 0.57 cm^{2}/Vs, has been reported in bulk Mg-doped $Al_{0.6}Ga_{0.4}N$ on sapphire, with Mg doping concentration of ~7×10^{19} cm^{-3} [133].

Moreover, besides the relatively large E_a of Mg dopant, the co-doping effect from native point defects and impurities is another limiting factor for sufficient p-type conduction. These defects influence the availability of Mg dopants contributing to free holes [112, 113, 116, 135]. By controlling the co-doping effect, a low resistivity of 10 Ω·cm has been achieved recently in heavily Mg-doped (5×10^{19} cm^{-3}) bulk $Al_{0.6}Ga_{0.4}N$ on AlN, with a hole concentration around 3×10^{18} cm^{-3} and mobility around 0.2 cm^2/Vs [126].

2.2.3 Unbalanced Carrier Distribution

Excellent charge carrier transport is another prerequisite for achieving AlGaN deep UV LDs. However, WZ AlGaN alloys have a relatively large effective mass of holes, ranging from 0.46 m_0 in GaN to 2.7 m_0 in AlN [123], compared to that of electrons, increasing from 0.2 m_0 in GaN to 0.3 m_0 in AlN [20]. Lower hole mobilities than electron mobilities are expected in AlGaN epilayers. Thereby, highly unbalanced carrier distribution in the active region and electron overflow could occur, which is particularly the case for the device structures with high Al contents, significantly limiting the charge carrier density in the device active region and making it impossible to reach transparency condition.

To mitigate this issue, various approaches have been investigated in the past. One way is to insert a thin bulk electron blocking layer (EBL) with high Al composition between the active region and p-type injection layers [136-147]. However, such bulk EBL could also simultaneously block hole injection. Therefore, different EBL designs have been demonstrated to take care of the hole transport in the meantime, including graded EBL (GEBL) [138-140, 143] and superlattice EBL (SL-EBL) [136, 144, 148, 149]. Moreover, other techniques such as band engineering of last quantum barrier (LQB) [150-152], insertion of SPSLs structures [130, 153-155], DPD method [18, 124, 156-158], and implementation of tunnel junctions (TJs) [159-169] have also been widely studied both theoretically and experimentally.

In addition to the strategies mentioned above, hot hole generation is another way to improve hole injection. By utilizing the favorable electric polarization, holes can gain additional kinetic energies when traveling through the p-region and accelerate the transport process. A detailed discussion on the hot hole effect will be presented in Chapter 7.

2.2.4 Optical Confinement and Polarization

Even though balanced charge carrier transportation could be achieved via band engineering, this does not mean such doping concentrations can be used in an AlGaN deep UV LD structure. This is because a high doping can cause a high optical loss. A low doping, however, makes it difficult to obtain high p-type conductivity. As such, the trade-off between electrical conduction and optical loss is obvious. Moreover, from the optical confinement viewpoint, since the refractive index contrast for AlGaN alloys is relatively small, thick Al-rich p-AlGaN regions are typically required to ensure proper optical confinement. This creates several issues, such as decreased p-type conductivity, higher optical loss due to both UV light absorption and Mg induced scattering loss. Therefore, a careful design is required.

To further move on to even shorter lasing wavelengths, the optical polarization switching from TE to TM becomes another bottleneck. Today, it has remained challenging to achieve AlGaN QW with TE-polarized light emission for wavelengths shorter than 250 nm [3, 60]. As the Al content in AlGaN alloy increases, the emission changes from TE polarization to TM polarization, due to the difference in crystal-field splitting between GaN and AlN [170]. It is also reported that the TE gain of AlGaN QWs decreases as Al content increases, whereas the TM gain shows an opposite trend, attributed to the strong mixing of the light-hole (LH) and crystal-field split-off (CH) sub-bands [171]. Nevertheless, the TM-polarized light penetrates deeper into the p-type region of a laser structure than the TE-polarized light does [3], giving a higher optical loss. Therefore, to achieve deep UV lasing, TE polarization is preferred, especially for low threshold deep UV lasing.

Ultrathin GaN can be a potential solution to achieve TE-polarized light below 250 nm, due to the larger separation between heavy-hole (HH)/LH and CH sub-bands [172-174]. The light emission comes from the dominant conduction (C) to HH sub-band transitions, instead of C-CH transitions in conventional AlGaN structures with high Al contents. Using MBE-grown ultrathin GaN/AlN heterostructures, 226 nm TE-polarized light emission has been reported by Bayerl *et al.* [175].

2.2.5 Challenges in Fabrication

In order to realize efficient electrical injection, ohmic contact is necessary. Nevertheless, the commonly available metal does not have proper work function to enable ohmic contact to large bandgap AlGaN alloys. Moreover, the poor p-type conduction of AlGaN makes it even more challenging to realize ohmic contact with high Al-content p-AlGaN. Therefore, a common strategy is to grow a thin degenerately doped p-GaN contact layer on top, providing a desired specific contact resistance (ρ_c) in the range of 10^{-5} to 10^{-6} $\Omega\cdot\text{cm}^2$ [176]; unfortunately, this is at the cost of high UV absorption. To overcome the p-contact issue, low resistive TJs, ending with n-AlGaN contact layers, could be a suitable solution [168, 177, 178]. In contrast to contacts to p-layers, low ρ_c to n-AlGaN has been achieved, with a value of 10^{-6} $\Omega\cdot\text{cm}^2$ for $x < 0.8$ and 10^{-3} $\Omega\cdot\text{cm}^2$ for $x > 0.8$ [2].

Furthermore, reliable cleaving along the *m*-plane and facet coating with highly reflective mirrors, e.g., HfO_2/SiO_2, are typically required in the LD fabrication process, as the naturally cleaved facet only provides a reflectivity of ~19% [10, 18, 81, 82]. Nonetheless, due to the hardness of sapphire and AlN substrates, cracks could be easily generated on cleaved substrates with unfavorable cleaving planes. To mitigate this issue, approaches such as substrate lapping, laser scribing, cavity-end polishing, as well as dry and/or wet etching process have been reported [10, 59, 83, 179, 180]. However, those methods not only inevitably increase the fabrication cost and process time, but also suffer the risk of device performance degradation.

Chapter 3

High Quality Nanowire-assisted AlN Template on Silicon

As introduced earlier, significant research progress has been made on AlGaN UV lasers grown on sapphire and AlN substrates [18, 53, 69, 85]. In sharp contrast, the development of AlGaN UV lasers on Si falls behind, despite the appealing benefits offered by Si substrates [44]. This is mainly ascribed to the large lattice mismatch and thermal mismatch between hexagonal AlGaN and Si (111) substrates, leading to high defect densities and micro cracks [108]. Therefore, obtaining high quality crack-free AlN on Si, as a platform for further AlGaN epilayer growth, is necessary towards the realization of AlGaN UV lasers on Si.

In this Chapter, we report smooth and nearly strain-free AlN thin film on a GaN nanowire template on Si, through the coalescence of AlN, by MBE in the N-rich environment. Lattice mismatch induced strain was largely relaxed during the nanowire growth stage, with dislocations mainly localized around the coalescence boundaries. High quality crack-free AlN thin film was obtained beyond the coalescence region.

3.1 Manuscript

The following manuscript was published in *Crystal Growth & Design* (X. Yin, Q. Zhang, and S. Zhao, "Molecular Beam Epitaxial Growth of AlN Thin Films on Si through Exploiting Low Al Adatom Migration and the Nitrogen-Rich Environment on a Nanowire Template," *Crystal Growth & Design,* vol. 21, no. 7, pp. 3645-3649, 2021, doi: 10.1021/acs.cgd.1c00327).

This manuscript represents the MBE growth of high quality and nearly strain-free nanowire-assisted AlN template on Si, with corresponding structural properties studied in detail. This work aims at providing a low-cost, highly reproducible, and rapid way to grow high quality AlN buffer on Si for the development of AlGaN UV lasers.

Molecular Beam Epitaxial Growth of AlN Thin Films on Si in the Nitrogen-rich Environment on a Nanowire Template

*Xue Yin, Qihua Zhang, and Songrui Zhao**

Department of Electrical and Computer Engineering, McGill University, 3480 University Street,
Montreal, Quebec H3A 0E9, Canada

Abstract: In this work, we demonstrate an aluminum nitride (AlN) thin film on Si through exploiting the low Al adatom migration and the nitrogen (N)-rich environment on a nanowire template by molecular beam epitaxy. The AlN thin film is relatively smooth, and the X-ray diffraction experiments further suggest that the film is nearly strain free. In addition, the observation of 3 × reconstruction from the reflection high-energy electron diffraction suggests that the AlN film is N-polar, which is further confirmed by chemical etching experiments. We further show that, using such an AlN thin film as a buffer layer, room-temperature ultraviolet-emitting aluminum gallium nitride (AlGaN) epilayers at various wavelengths can be obtained on Si.

Keywords: aluminum nitride, coalescence, Si, ultraviolet, molecular beam epitaxy

3.1.1. Introduction

Aluminum nitride (AlN) on silicon (Si) is an appealing platform for semiconductor electronic and optoelectronic devices, not only for the availability of high crystalline quality Si substrates at a low cost and the dominant role of Si in modern semiconductor device technologies but also for the technical importance of AlN for a wide range of applications, such as deep ultraviolet (UV) light emission (i.e., light emission wavelength less than 300 nm), high electron mobility transistors (HEMTs), microelectromechanical systems (MEMS), and surface acoustic wave (SAW) devices.[1-6] Moreover, obtaining high-quality AlN on Si represents the first step toward III-nitrides-based electronic and optoelectronic devices on Si.[7-17] For example, AlN is an important buffer layer for aluminum gallium nitride (AlGaN) deep UV light-emitting devices on Si;[10-12] and it has been found that there is a direct correlation between the device performance improvement and the improvement in the AlN buffer layer quality.[10, 11]

In the past, various techniques have been used for the growth of AlN on Si, including molecular beam epitaxy (MBE), metal-organic chemical vapor deposition (MOCVD) and/or metal-organic vapor phase epitaxy (MOVPE), and pulsed laser deposition (PLD).[9, 18-30] However, it remains challenging today to grow high-quality AlN thin films on Si, due to the large thermal and lattice mismatches between hexagonal AlN and Si (111). Different from the growth of GaN on Si, wherein the tensile strain can be compensated by using AlN and/or AlGaN buffer layers that introduce compressive strain, for the growth of AlN on Si, there are no such strain compensation buffer layers due to the unavailability of a material that can be grown epitaxially with a lattice constant smaller than that of AlN.

Hitherto, with the aim of obtaining high-quality AlN on Si, different approaches have been developed. These include applying the NH_3 pulsed-flow growth mode in a MOCVD chamber,[14] using silicon-on-insulator (SOI) wafers,[26] employing Si substrates with different orientations,[28] and exploiting the lateral epitaxial overgrowth (LEO) on patterned substrates.[12, 27, 30-32] Indeed, high-quality AlN thin films have been achieved on patterned Si.[10-12, 16, 30, 32] In spite of the progress, the growth on patterned Si remains a costly process. Lithography and etching processes, which are required for the wafer patterning, add additional time and dollar cost.

In recent years, self-organized GaN nanowires by plasma-assisted MBE have emerged as an alternative path to "pattern" an Si substrate and have been used for the GaN thin film growth.[33-37] This is an appealing approach, as it is free of the lithography process and the GaN nanowire template could relax the large strain induced by Si in the GaN thin film. However, the GaN thin films obtained often show rough surfaces with noticeable three-dimensional (3D) features. Moreover, there have been no studies of using a GaN nanowire template to grow AlN thin films on Si.

In this work, we demonstrate AlN thin film on a GaN nanowire template in a nitrogen (N)-rich environment through the coalescence of AlN by MBE, which is different from the conventional approaches to grow AlN thin films on Si. Our detailed electron microscopy characterizations suggest that the AlN thin film is relatively smooth, drastically improved in comparison to GaN thin films obtained from the coalescence of self-organized GaN nanowires. X-ray diffraction (XRD) experiments further indicate that such an AlN thin film is nearly strain free. Moreover, the AlN thin film is further confirmed to be N-polar. Lastly, by further using such AlN thin film as a buffer layer, deep-UV-emitting AlGaN epilayers have been further demonstrated on Si.

3.1.2. Experimental Section

In this work, the AlN sample was grown by Veeco GENxplor plasma-assisted MBE on 3-inch Si (111) substrates. Standard solvent cleaning and hydrofluoric acid etching were performed before loading the substrate to the MBE system. Prior to the growth, the wafer was thermally outgassed *in situ* for 15 min. This was followed by the growth of a GaN nanowire template under the N-rich condition. The growth parameters for AlN thin film included a substrate temperature of 810 ℃, a N flow rate of 1 sccm, and an Al flux of around 2×10^{-8} Torr.

The detailed structural properties were characterized by scanning electron microscopy (SEM) and scanning transmission electron microscopy (STEM). The specimen for the cross-sectional imaging was prepared by a focused ion beam (FIB) etching, wherein a platinum (Pt) protective layer was coated on the sample surface. The XRD 2θ-θ scan was performed to assess the crystalline properties of the as-grown wafer.

The photoluminescence (PL) experiments were performed at room temperature, with a 213 nm pulse laser. The laser has a pulse width of 7 ns. In this experiment, the laser light was focused onto the sample surface by a silica focus lens, and the emitted light was collected by a silica focus lens from the sample surface. The collection lens was further coupled to an optical fiber, which was connected to a deep-UV spectrometer for spectral analysis.

3.1.3. Results and Discussion

Figure 3.1 illustrates the conceptual growth process. First, we start the growth with a GaN nanowire template that is self-organized and is free of any time- and cost-consuming lithography and etching processes;[38, 39] by optimizing the growth condition, we bring the individual GaN nanowires close to coalescence (**Figure 3.1 (a)**). Then, we start the growth of AlN. By exploitation of the slow Al adatom migration, the vertical growth is reduced, which subsequently promotes the coalescence of AlN (**Figure 3.1 (b)**). In the end, beyond the coalescence region, a high-quality AlN thin film is obtained in the N-rich environment (**Figure 3.1 (c)**).

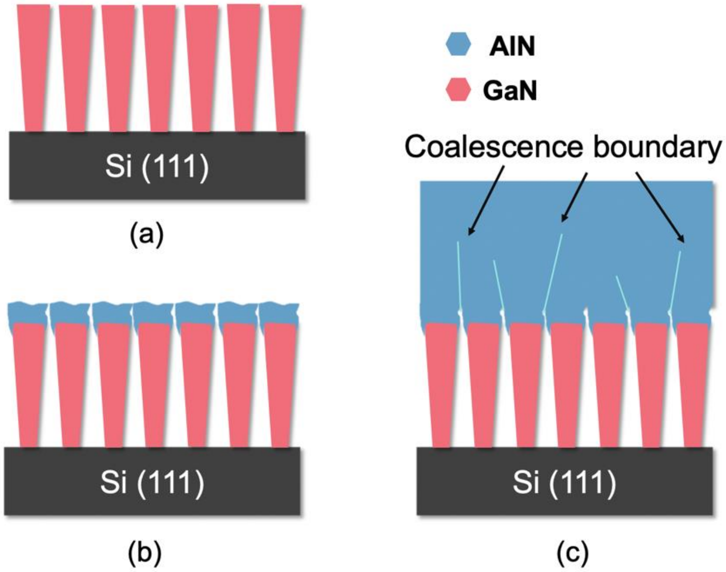

Figure 3.1. (a) Schematic of the self-organized GaN nanowire template. (b) Initial growth of nanoscale AlN crystals on the GaN nanowire template. (c) AlN thin film obtained through the coalescence of AlN.

There are a few key factors that ensure the success of the above conceptual growth process. First, as the starting point of this approach is nanowires, the large strain induced by Si substrates can be well relaxed at the nanowire growth stage and high-quality nanowires on Si substrates have been shown previously.[38, 39]

Second, previous studies have shown that, for the nanowire coalescence process, structural defects are mainly localized around the coalescence boundaries, and the area beyond the coalescence region can have high quality.[33, 35]

Third, we exploit the slow Al adatom migration during the AlN coalescence process. It is well-known that the slow migration of Al makes the growth of AlN and/or high-Al-content AlGaN more challenging than that of GaN, and significant efforts have been spent in improving the Al migration: e.g., high growth temperatures are used for the growth of AlN and/or high-Al content AlGaN nanowires on a GaN nanowire template.[40, 41] Here we utilize the low Al migration, rather than work against it. In comparison to the typical growth temperature of AlN nanowires under N-rich conditions, the growth temperature of AlN used in the present study is considerably lower.[40, 42] As such, the low Al adatom migration leads to a low vertical growth rate and promotes the coalescence. This also contributes to the achievement of smooth films with a small thickness.

At this point, it is noted that typically for the growth of III-nitride thin films, the low mobility of metal species leads to rough thin films. However, the growth conditions of AlN in the present study fall in the N-rich growth conditions of III-nitride thin films by MBE: i.e., the use of a relatively high substrate temperature and higher N flux in comparison to the flux of metal species. It has been shown previously that N-rich conditions can lead to smooth III-nitride thin films by MBE. [43] Separately, it is also noted that, hitherto, III-nitride thin films grown by MBE are predominantly under metal-rich conditions, and the growth in N-rich condition is rare.

Figure 3.2 shows the reflection high-energy electron diffraction (RHEED) patterns along the $\langle 11\bar{2}0\rangle$ direction at different growth stages. As shown in **Figure 3.2 (a)**, towards the end of the growth of the GaN nanowire template, the dots, which correspond to the 3D growth of vertically aligned GaN nanowires under the N-rich conditions, became connected. This indicates a high density of nanowires and/or the start of coalescence. After the growth of AlN was started for 30 min, the RHEED pattern evolved into streaks, with the presence of certain spotty features (**Figure 3.2 (b)**). Towards the end of the growth, a completely streaky RHEED pattern was observed (**Figure 3.2 (c)**), suggesting the formation of a smooth, planar thin film. Moreover, a clear 3 × RHEED reconstruction was observed during cooling of the wafer (**Figure 3.2 (d)**), indicating that the present AlN film is N-polar.[9, 44] This is further confirmed by the potassium hydroxide (KOH) wet etching experiments (to be discussed).

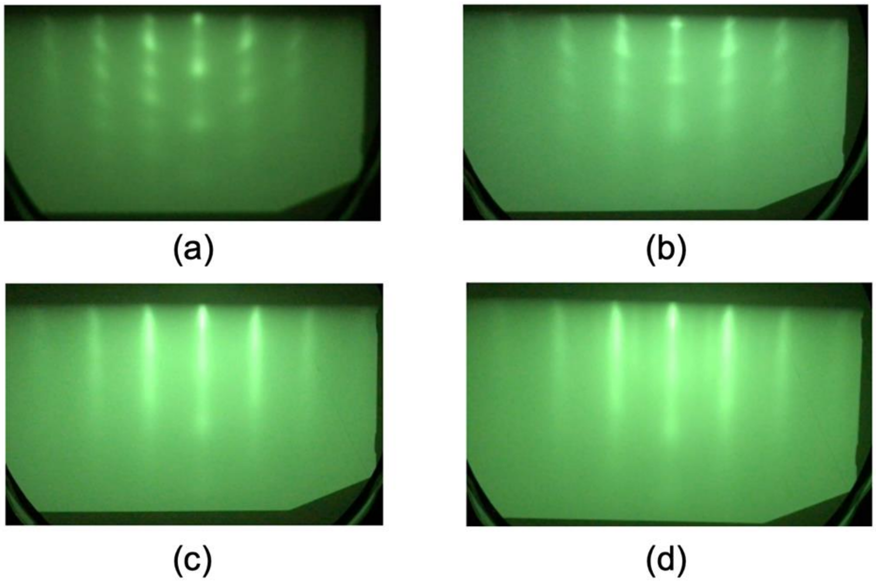

Figure 3.2. The RHEED pattern along the $\langle 11\bar{2}0 \rangle$ direction, taken (a) at the end of the growth of the GaN nanowire template, (b) 30 mins after the growth of the AlN, (c) towards the end of the AlN growth, and (d) during cooling down after the growth (at ~400 ℃), respectively.

We further characterized the surface morphology and structural properties of the AlN thin film. **Figure 3.3 (a)** illustrates the large-scale SEM image of the sample, manifesting that the film is crack-free. As further shown by **Figure 3.3 (b)**, the film shows a relatively smooth surface, in contrast to the previously reported GaN thin films through the coalescence of self-organized GaN nanowires, which are rough and possess noticeable 3D features.[33-37] This can be largely explained by the benefit of lower Al mobility compared to Ga during the coalescence stage, such that the adverse effects of using self-organized nanowires for obtaining smooth thin films, e.g., the nonuniform nanowire height and the misorientation of individual nanowires with respect to the substrate, as encountered during the growth of GaN thin films through the coalescence of self-organized GaN nanowires, can be largely mitigated. It is also noted that, as the GaN thin films through the coalescence of self-organized GaN nanowires are generally rough, it thus might not be practical to use such GaN thin films as the template to further grow AlN thin films. In addition, from the viewpoint of fabricating of deep-UV photonic devices, GaN in general needs to be avoided due to the absorption of deep-UV light.

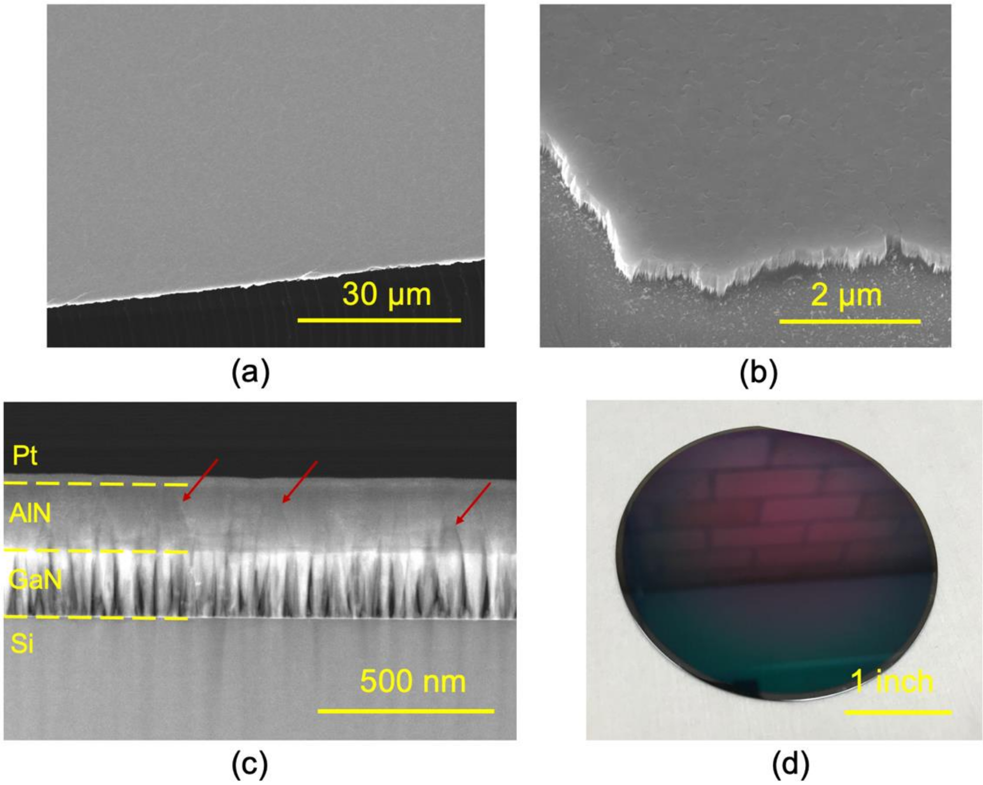

Figure 3.3. (a) Large-scale and (b) small-scale SEM images of the as-grown wafer, indicating an overall crack-free, smooth surface. (c) Cross-sectional STEM HAADF image of the wafer. The arrows mark exemplary coalescence boundaries. (d) Optical image of the wafer.

Figure 3.3 (c) shows the cross-sectional STEM high-angle annular dark-field (HAADF) image of the sample, with each layer labeled. The GaN nanowire template exhibits a relatively uniform height and vertical alignment, as well as a strong tapering that minimizes the nanowire spacing and/or enables a certain degree of coalescence before the growth of AlN. This morphology is consistent with what is shown from the RHEED pattern (**Figure 3.2 (a)**). After the growth of AlN was started, the coalescence became more noticeable and was completed before the end of the growth. A few coalescence boundaries are marked by arrows. Our detailed examination further suggests that the average minimum thickness for the completion of coalescence is around 120 nm. A relatively smooth surface is also seen from the STEM image. An optical image of such an AlN on Si wafer is shown in **Figure 3.3 (d)**. It is seen that the wafer is mirror-reflective (with a clear view of environmental elements) and uniform, without any color rings.

We have further investigated the crystalline properties of the AlN thin film by XRD experiments. **Figure 3.4** is a 2θ-θ scan over a scanning angle of 33°-37°. The two diffraction peaks at $2\theta = 34.64°$ and 36.00° are from GaN (002) plane and AlN (002) plane, respectively. In general, the 2θ-θ scan peak position can be a rapid strain condition estimation, and the diffraction peak position from the AlN (002) plane indicates that the present AlN thin film is nearly free of strain.[45] As such, although the nominal thickness (including the coalescence region) of the present AlN thin film is around 180 nm, it could be possible to grow thicker films without cracks. The full width at half maximum (FWHM) of the diffraction peak from the AlN (002) plane is derived to be around 972 arcsec (0.27°), and this FWHM broadening could be ascribed to crystal size and misorientation.[45]

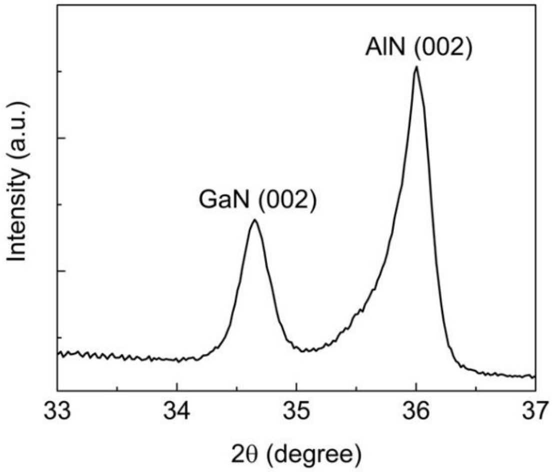

Figure 3.4. XRD 2θ-θ scan of the as-grown wafer.

We then examined the polarity of the AlN thin film through a KOH wet etching experiment. In this experiment, 45% w/w potassium hydroxide solution was diluted into 3 mol/L molar concentration and maintained at room temperature. After etching, deionized (DI) water was applied immediately to remove any residual chemicals, followed by drying with nitrogen gas. **Figure 3.5** shows the SEM image of the wafer after KOH etching. It is seen that the AlN thin film surface was etched, which is a fingerprint of N-polarity.[9, 46]

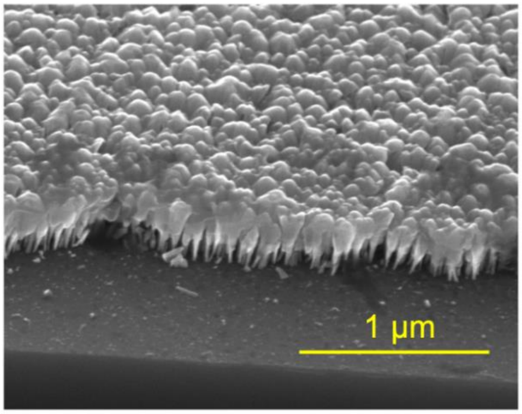

Figure 3.5. SEM image of the sample after KOH etching.

In the end, we show that using such an AlN thin film as a buffer layer, AlGaN epilayers with different emission wavelengths can be obtained on Si. All the AlGaN epilayers were grown under metal-rich conditions at a substrate temperature of 720 ℃. The relatively low substrate temperature is to ensure the presence of a Ga metal layer at the growth front and a smooth surface. The thickness of the AlGaN epilayers was around 50 nm. **Figure 3.6** illustrates the normalized PL spectra of three samples with different Al compositions. It is seen that the emission wavelengths at 287 nm, 307 nm, and 312 nm were obtained. The Al contents, using Vegard's law with bandgap energies E_g(GaN) = 3.4 eV, E_g(AlN) = 6.2 eV and a bowing parameter of 0.7 eV,[47] were further estimated to be around 0.37, 0.27, and 0.24, respectively.

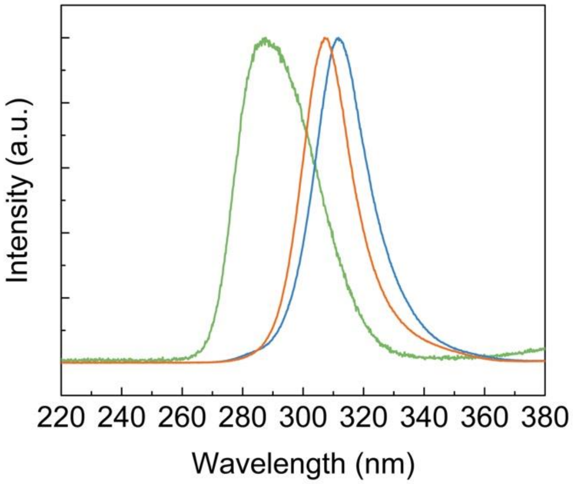

Figure 3.6. Room-temperature PL spectra of AlGaN epilayers with different Al contents grown on the AlN buffer layer on Si.

3.1.4. Conclusion

In summary, we have demonstrated a new approach to grow AlN thin films on Si, which exploits the low Al migration mobility during the coalescence stage and the N-rich growth regime of the film on a nanowire template by MBE. The obtained AlN thin film is relatively smooth – drastically improved in comparison to GaN thin films obtained from the coalescence of self-organized GaN nanowires. XRD experiments further indicate that the film is nearly strain free. In comparison to the previous approaches of growing AlN thin films on Si, our approach enables highly reproducible low-cost and high-quality AlN thin films on Si that can be fabricated rapidly. With the demonstration of AlGaN epilayers with a room-temperature deep-UV emission using such AlN thin films as a buffer layer, as well as the N polarity of the AlN thin film that brings additional benefits to electronic and optoelectronic devices, such as the lower contact resistance and the reduced efficiency droop,[48-50] this AlN on Si buffer layer technology by MBE could enable high-performance, highly compact, and low-cost III-nitride optoelectronic and electronic devices *in situ* on Si.

References

(1) Strite, S.; Morkoc, H., GaN, AlN, and InN: a review. *J. Vac. Sci. Technol., B: Microelectron. Nanometer Struct.* **1992,** *10,* 1237-1266.

(2) Iriarte, G. F.; Rodríguez, J. G.; Calle, F., Synthesis of c-axis oriented AlN thin films on different substrates: A review. *Mater. Res. Bull.* **2010,** *45*, 1039-1045.

(3) Taniyasu, Y.; Kasu, M.; Makimoto, T., An aluminium nitride light-emitting diode with a wavelength of 210 nanometres. *Nature* **2006,** *441*, 325-8.

(4) Li, J.; Nam, K. B.; Nakarmi, M. L.; Lin, J. Y.; Jiang, H. X.; Carrier, P.; Wei, S.-H., Band structure and fundamental optical transitions in wurtzite AlN. *Appl. Phys. Lett.* **2003,** *83*, 5163-5165.

(5) M. Shatalov, M. G., V. Adivarahan, and A. Khan, , Room-Temperature Stimulated Emission from AlN at 214 nm. *Jpn. J. Appl. Phys.* **2006,** *45*, L1286.

(6) Zhao, S.; Connie, A. T.; Dastjerdi, M. H.; Kong, X. H.; Wang, Q.; Djavid, M.; Sadaf, S.; Liu, X. D.; Shih, I.; Guo, H.; Mi, Z., Aluminum nitride nanowire light emitting diodes: Breaking the fundamental bottleneck of deep ultraviolet light sources. *Sci Rep* **2015,** *5*, 8332.

(7) A.Watanabe; T.Takeuchi; K.Hirosawa; H.Amano; K.Hiramatsu; I.Akasaki, The growth of single crystalline GaN on a Si substrate using A1N as an intermediate layer. *J. Cryst. Growth* **1993,** *128*, 391.

(8) Chen, P.; Zhang, R.; Zhao, Z. M.; Xi, D. J.; Shen, B.; Chen, Z. Z.; Zhou, Y. G.; Xie, S. Y.; Lu, W. F.; Zheng, Y. D., Growth of high quality GaN layers with AlN buffer on Si(1 1 1) substrates. *J. Cryst. Growth* **2001,** *225*, 150-154.

(9) Dasgupta, S.; Wu, F.; Speck, J. S.; Mishra, U. K., Growth of high quality N-polar AlN($000\bar{1}$) on Si(111) by plasma assisted molecular beam epitaxy. *Appl. Phys. Lett.* **2009,** *94*, 151906.

(10) Tran, B. T.; Maeda, N.; Jo, M.; Inoue, D.; Kikitsu, T.; Hirayama, H., Performance Improvement of AlN Crystal Quality Grown on Patterned Si(111) Substrate for Deep UV-LED Applications. *Sci Rep* **2016,** *6*, 35681.

(11) Tran, B. T.; Hirayama, H., Growth and Fabrication of High External Quantum Efficiency AlGaN-Based Deep Ultraviolet Light-Emitting Diode Grown on Pattern Si Substrate. *Sci Rep* **2017,** *7*, 12176.

(12) Zhang, Y.; Gautier, S.; Cho, C.-Y.; Cicek, E.; Vashaei, Z.; McClintock, R.; Bayram, C.; Bai, Y.; Razeghi, M., Near milliwatt power AlGaN-based ultraviolet light emitting diodes based on lateral epitaxial overgrowth of AlN on Si(111). *Appl. Phys. Lett.* **2013,** *102*, 011106.

(13) Arulkumaran, S.; Egawa, T.; Matsui, S.; Ishikawa, H., Enhancement of breakdown voltage by AlN buffer layer thickness in AlGaN/GaN high-electron-mobility transistors on 4in. diameter silicon. *Appl. Phys. Lett.* **2005,** *86*, 123503.

(14) Fujikawa, S.; Hirayama, H., 284–300 nm Quaternary InAlGaN-Based Deep-Ultraviolet Light-Emitting Diodes on Si(111) Substrates. *Appl. Phys. Express* **2011,** *4*, 061002.

(15) Xiang, P.; Liu, M.; Yang, Y.; Chen, W.; He, Z.; Leung, K. K.; Surya, C.; Han, X.; Wu, Z.; Liu, Y.; Zhang, B., Improving the Quality of GaN on Si(111) Substrate with a Medium-Temperature/High-Temperature Bilayer AlN Buffer. *Jpn. J. Appl. Phys.* **2013,** *52*, 08jb18.

(16) Cicek, E.; McClintock, R.; Cho, C. Y.; Rahnema, B.; Razeghi, M., AlxGa1−xN-based solar-blind ultraviolet photodetector based on lateral epitaxial overgrowth of AlN on Si substrate. *Appl. Phys. Lett.* **2013,** *103*, 181113.

(17) Tran, B. T.; Lin, K.-L.; Sahoo, K. C.; Chung, C.-C.; Nguyen, C.-L.; Chang, E. Y., Effect of multiple AlN layers on quality of GaN films grown on Si substrates. *Electron. Mater. Lett.* **2014,** *10*, 1063-1067.

(18) Stevens, K. S.; Ohtani, A.; Kinniburgh, M.; Beresford, R., Microstructure of AlN on Si (111) grown by plasma‐assisted molecular beam epitaxy. *Appl. Phys. Lett.* **1994,** *65*, 321-323.

(19) Lin, W. T.; Meng, L. C.; Chen, G. J.; Liu, H. S., Epitaxial growth of cubic AlN films on (100) and (111) silicon by pulsed laser ablation. *Appl. Phys. Lett.* **1995,** 66, (16), 2066-2068.

(20) Vispute, R. D.; Narayan, J.; Wu, H.; Jagannadham, K., Epitaxial growth of AlN thin films on silicon (111) substrates by pulsed laser deposition. *J. Appl. Phys.* **1995,** *77*, 4724-4728.

(21) Calleja, E.; Sánchez-García, M. A.; Monroy, E.; Sánchez, F. J.; Muñoz, E.; Sanz-Hervás, A.; Villar, C.; Aguilar, M., Growth kinetics and morphology of high quality AlN grown on Si(111) by plasma-assisted molecular beam epitaxy. *J. Appl. Phys.* **1997,** *82*, 4681-4683.

(22) Bourret, A.; Barski, A.; Rouvière, J. L.; Renaud, G.; Barbier, A., Growth of aluminum nitride on (111) silicon: Microstructure and interface structure. *J. Appl. Phys.* **1998,** *83*, 2003.

(23) Lahreche, H.; Vennegues, P.; Tottereau, O.; Laugt, M.; Lorenzini, P.; Leroux, M.; Beaumont, B.; Gibart, P., Optimisation of AlN and GaN growth by metalorganic vapour-phase epitaxy (MOVPE) on Si(1 1 1). *J. Cryst. Growth* **2000,** *217*, 13.

(24) Lebedeva, V.; Jinschek, J.; Kräußlich, J.; Kaiser, U.; Schröter, B.; Richter, W., Hexagonal AlN films grown on nominal and off-axis Si(0 0 1) substrates. *J. Cryst. Growth* **2001,** *230*, 426.

(25) Auner, G. W.; Jin, F.; Naik, V. M.; Naik, R., Microstructure of low temperature grown AlN thin films on Si(111). *J. Appl. Phys.* **1999,** *85*, 7879-7883.

(26) Niu, L.; Hao, Z.; E, Y.; Hu, J.; Wang, L.; Luo, Y., MBE-grown AlN-on-Si with improved crystalline quality by using silicon-on-insulator substrates. *Appl. Phys. Express* **2014,** *7*, 065505.

(27) Tran, B. T.; Hirayama, H.; Jo, M.; Maeda, N.; Inoue, D.; Kikitsu, T., High-quality AlN template grown on a patterned Si(111) substrate. *J. Cryst. Growth* **2017,** *468*, 225-229.

(28) Shen, X.-Q.; Takahashi, T.; Ide, T.; Shimizu, M., High quality thin AlN epilayers grown on Si(110) substrates by metal-organic chemical vapor deposition. *CrystEngComm* **2017,** *19*, 1204-1209.

(29) Huang, L.; Li, Y.; Wang, W.; Li, X.; zheng, Y.; Wang, H.; Zhang, Z.; Li, G., Growth of high-quality AlN epitaxial film by optimizing the Si substrate surface. *Appl. Surf. Sci.* **2018,** *435*, 163-169.

(30) Shen, J.; Yang, X.; Liu, D.; Cai, Z.; Wei, L.; Xie, N.; Xu, F.; Tang, N.; Wang, X.; Ge, W.; Shen, B., High quality AlN film grown on a nano-concave-circle patterned Si substrate with an AlN seed layer. *Appl. Phys. Lett.* **2020,** *117*, 1204-1209.

(31) Robin, Y.; Ding, K.; Demir, I.; McClintock, R.; Elagoz, S.; Razeghi, M., High brightness ultraviolet light-emitting diodes grown on patterned silicon substrate. *Mater. Sci. Semicond. Process.* **2019,** *90*, 87-91.

(32) Demir, İ.; Robin, Y.; McClintock, R.; Elagoz, S.; Zekentes, K.; Razeghi, M., Direct growth of thick AlN layers on nanopatterned Si substrates by cantilever epitaxy. *Phys. Status Solidi (a)* **2017,** *214*, 1600303.

(33) Dogan, P.; Brandt, O.; Pfüller, C.; Lähnemann, J.; Jahn, U.; Roder, C.; Trampert, A.; Geelhaar, L.; Riechert, H., Formation of High-Quality GaN Microcrystals by Pendeoepitaxial Overgrowth of GaN Nanowires on Si(111) by Molecular Beam Epitaxy. *Cryst. Growth Des.* **2011,** *11*, 4257-4260.

(34) Yeom, B.-R.; Navamathavan, R.; Park, J.-H.; Ra, Y.-H.; Lee, C.-R., Growth behavior of GaN epilayers on Si(111) grown by GaN nanowires assisted epitaxial lateral overgrowth. *CrystEngComm* **2012,** *14*, 5558.

(35) Fan, S.; Zhao, S.; Liu, X.; Mi, Z., Study on the coalescence of dislocation-free GaN nanowires on Si and SiOx. *J. Vac. Sci. Technol., B: Nanotechnol. Microelectron.: Mater., Process., Meas., Phenom.* **2014,** *32*, 02C114.

(36) Wu, Y.; Wang, Y.; Sun, K.; Aiello, A.; Bhattacharya, P.; Mi, Z., Molecular beam epitaxy and characterization of Mg-doped GaN epilayers grown on Si (0 0 1) substrate through controlled nanowire coalescence. *J. Cryst. Growth* **2018,** *498*, 109-114.

(37) Bougrioua, Z.; Gibart, P.; Calleja, E.; Jahn, U.; Trampert, A.; Ristic, J.; Utrera, M.; Nataf, G., Growth of freestanding GaN using pillar-epitaxial lateral overgrowth from GaN nanocolumns. *J. Cryst. Growth* **2007,** *309*, 113-120.

(38) Zhao, S.; Lu, J.; Hai, X.; Yin, X., AlGaN Nanowires for Ultraviolet Light-Emitting: Recent Progress, Challenges, and Prospects. *Micromachines* **2020,** *11*, 125.

(39) Zhao, S.; Mi, Z., AlGaN Nanowires: Path to Electrically Injected Semiconductor Deep Ultraviolet Lasers. *IEEE J. Quantum Electron.* **2018,** *54*, 1-9.

(40) Landré, O.; Fellmann, V.; Jaffrennou, P.; Bougerol, C.; Renevier, H.; Cros, A.; Daudin, B., Molecular beam epitaxy growth and optical properties of AlN nanowires. *Appl. Phys. Lett.* **2010,** *96*, 061912.

(41) Zhao, S.; Woo, S. Y.; Sadaf, S. M.; Wu, Y.; Pofelski, A.; Laleyan, D. A.; Rashid, R. T.; Wang, Y.; Botton, G. A.; Mi, Z., Molecular beam epitaxy growth of Al-rich AlGaN nanowires for deep ultraviolet optoelectronics. *APL Mater.* **2016,** *4*, 086115.

(42) Zhong, Y.; Berikaa, E.; Lu, J.; Yin, X.; Zhao, S., Molecular beam epitaxial growth and optical characterization of AlGaN nanowires with reduced substrate temperature. *AIP Adv.* **2020**, *10*, 25022.

(43) Koblmüller, G.; Wu, F.; Mates, T.; Speck, J. S.; Fernández-Garrido, S.; Calleja, E., High electron mobility GaN grown under N-rich conditions by plasma-assisted molecular beam epitaxy. *Appl. Phys. Lett.* **2007,** *91*, 221905.

(44) Brubaker, M. D.; Duff, S. M.; Harvey, T. E.; Blanchard, P. T.; Roshko, A.; Sanders, A. W.; Sanford, N. A.; Bertness, K. A., Polarity-Controlled GaN/AlN Nucleation Layers for Selective-Area Growth of GaN Nanowire Arrays on Si(111) Substrates by Molecular Beam Epitaxy. *Cryst. Growth Des.* **2015,** *16*, 596-604.

(45) Moram, M. A.; Vickers, M. E., X-ray diffraction of III-nitrides. *Rep. Prog. Phys.* **2009,** *72*, 036502.

(46) Brubaker, M. D.; Levin, I.; Davydov, A. V.; Rourke, D. M.; Sanford, N. A.; Bright, V. M.; Bertness, K. A., Effect of AlN buffer layer properties on the morphology and polarity of GaN nanowires grown by molecular beam epitaxy. *J. Appl. Phys.* **2011,** *110*, 053506.

(47) Vurgaftman, I.; Meyer, J. R., Band parameters for nitrogen-containing semiconductors. *J. Appl. Phys.* **2003,** *94*, 3675-3696.

(48) Wong, M. H.; Keller, S.; Dasgupta, N. S.; Denninghoff, D. J.; Kolluri, S.; Brown, D. F.; Lu, J.; Fichtenbaum, N. A.; Ahmadi, E.; Singisetti, U.; Chini, A.; Rajan, S.; DenBaars, S. P.; Speck, J. S.; Mishra, U. K., N-polar GaN epitaxy and high electron mobility transistors. *Semicond. Sci. Technol.* **2013,** *28*, 074009.

(49) Verma, J.; Simon, J.; Protasenko, V.; Kosel, T.; Grace Xing, H.; Jena, D., N-polar III-nitride quantum well light-emitting diodes with polarization-induced doping. *Appl. Phys. Lett.* **2011,** *99*, 171104.

(50) Akyol, F.; Nath, D. N.; Krishnamoorthy, S.; Park, P. S.; Rajan, S., Suppression of electron overflow and efficiency droop in N-polar GaN green light emitting diodes. *Appl. Phys. Lett.* **2012,** *100*, 111118.

3.2 Further Discussions on Coalescence

III-nitride nanowires have been mainly studied by MBE in the past, which are formed through a diffusion-driven self-organized process under N-rich conditions. —Compared to their planar counterparts, Al(Ga)N nanowires possess a number of fundamental advantages: (1) due to the large surface area to bulk volume ratio, the lattice strain between Al(Ga)N nanowires and foreign substrates can be efficiently relaxed, leading to high-quality bulk regions; (2) the reduced QCSE and piezoelectric field, due to reduced strain; (3) the improved doping incorporation, due to enhanced surface doping of nanowires. Thus, MBE-grown Al(Ga)N nanowire could be a promising route to mitigate the challenges mentioned in Section 2.2.

In recent years, attempts have been made to high quality Al(Ga)N planar structures formation via spontaneous nanowire coalescence [45, 181-187]. Leveraging the advantages of nanowires, the lattice strain could be largely relaxed during the nanowire growth stage and the defects generated during the coalescence process could be localized near the coalescence boundaries, leading to high quality thin films beyond the coalescence region [45, 183, 184]. Self-organized GaN nanowires have been studied to form GaN thin films on Si; unfortunately, the obtained GaN thin films often lead to rough surfaces with hillocks and pits [183-186], mainly due to the uncontrollable nanowire height, misorientation, and various sizes [187]. Even though the selective-area growth (SAG) method can provide better control on the nanowire growth and achieves nearly dislocation-free structures, it is at the cost of long processing time and additional fabrication costs related to the patterned substrates [188].

Different from the GaN nanowire coalescence process, Al has a much slower adatom migration compared to Ga in the N-rich environment, the vertical growth rate of AlN is much slower, and thus the adverse effects of using the self-organized nanowires for obtaining high quality thin films, such as the non-uniform nanowire height and the misorientation of individual nanowires with respect to the substrate, could be potentially accommodated. Consequently, by exploiting the low Al adatom migration under relatively low growth temperature, high-quality AlN thin films that are free of hillocks and/or pits, as reflected in **Figure 3.3,** can be achieved via the AlN nanowire coalescence process. Such obtained AlN thin films could serve as potential templates for the future development of AlGaN-based photonic and electronic devices on Si.

Chapter 4

High Internal Quantum Efficiency AlGaN Epilayer on the AlN Template on Silicon

Following the successful demonstration of the smooth and nearly strain-free AlN template on Si, we take a further step towards the MBE growth of AlGaN epilayers on such templates. Moreover, we report the RT IQE study on such AlGaN epilayers, together with the analysis of the efficiency drop mechanism. As an indicator of the intrinsic material quality, IQE is closely related to the TDDs levels in the as-grown epilayers (discussed in Section 2.2). Therefore, fundamental studies on the IQE of AlGaN epilayers on Si are of great importance to the improvement of device quantum efficiency.

4.1 Manuscript

This manuscript was published in *ECS Journal of Solid State Science and Technology* (X. Yin and S. Zhao, "High Internal Quantum Efficiency AlGaN Epilayer Grown by Molecular Beam Epitaxy on Si Substrate," *ECS Journal of Solid State Science and Technology*, vol. 10, no. 7, pp.076001, 2021, doi: 10.1149/2162-8777/ac0f15.).

This manuscript studies both structural and optical properties of MBE-grown AlGaN epilayers on the nanowire-assisted AlN template on Si. RT IQE of ~50% was obtained, which is significantly improved compared to the previously reported counterparts grown on sapphire substrates [189-194].

High Internal Quantum Efficiency AlGaN Epilayer Grown by Molecular Beam Epitaxy on Si Substrate

Xue Yin and Songrui Zhao [z]

Department of Electrical and Computer Engineering, McGill Univeristy

3480 University Street, Montreal, Quebec H3A 0E9, Canada

[z] Corresponding Author E-mail Address [songrui.zhao@mcgill.ca]

Abstract: We report the molecular beam epitaxy growth and characterization of aluminum gallium nitride (AlGaN) epilayer on an Si substrate. The AlGaN epilayer was grown on an AlN buffer layer through a coalescence process on a nanowire template. The AlGaN epilayer possessed a relatively smooth surface. The room-temperature internal quantum efficiency (IQE) was investigated using the power-dependent photoluminescence experiments and theoretical analysis. A maximum IQE of around 50% is derived, with an estimated carrier density of 3×10^{18} cm^{-3}. This IQE is significantly improved compared to the previously reported bulk AlGaN epilayers grown on sapphire and/or AlN-on-sapphire templates. The efficiency droop mechanism is also discussed, which could presumably be attributed to the carrier delocalization.

4.1.1. Introduction

Over the past decades, aluminum gallium nitride (AlGaN) alloys have attracted great attention in developing ultraviolet (UV) phototransistors, solar-blind photodetectors, and semiconductor UV light-emitting devices including light-emitting diodes (LEDs) and laser diodes (LDs), due to their direct, ultra-wide, and tunable bandgap energies. [1-10] In fact, AlGaN-based UV light-emitting devices are positioned to replace conventional mercury-based UV light-emitting devices that have bulky size, low efficiency, and are environmental hazards.

Hitherto, AlGaN-based optoelectronic devices are mainly developed on foreign substrates, such as sapphire and AlN-on-sapphire templates. Compared with these foreign substrates, Si substrate has several advantages: (1) Low cost. (2) Si has excellent electrical and thermal conduction. (3) High-quality Si substrates are available at 12 inch at a low cost, taking the advantage of mature processing technologies. (4) Using Si as the substrate is an appealing route to the fabrication of flip-chip UV LEDs due to the easy removal of Si by wet etching. This is in contrast to the removal of sapphire substrates wherein the laser lift-off process can cause the degradation of devices.[11, 12] (5) The development of AlGaN UV LEDs on Si naturally allows the integration to Si-based electronics. However, the growth of high-quality AlGaN epilayers on Si substrate remains challenging, mainly due to the large lattice mismatch and thermal mismatch between AlGaN and Si, which leads to materials with large defect densities and cracks.[13]

Today, different techniques have been developed to improve the material quality. The most common approach is to use an AlN buffer layer. The use of AlN can introduce compressive strain and thus compensate the tensile strain of AlGaN layers on Si,[14-16] promising crack-free AlGaN epilayers on Si. Nonetheless, obtaining high-quality AlN buffer layers is not an easy task. Hitherto, different techniques have been developed, such as using superlattices (SLs),[17] employing a NH_3

pulsed-flow growth mode,[18] and exploiting lateral epitaxial growth (LEO) growth techniques.[13, 19-23] These efforts have enabled AlGaN UV LEDs down to 256 nm on Si with optical output powers in the milliwatt range.[18-21]

Another alternative approach is to use Al(Ga)N SLs. The typical strategy is to deposit Al(Ga)N SLs after an AlN layer.[24-26] Using AlN and AlGaN SL buffer layers, high-quality AlGaN epilayers have been achieved on Si.[24] Alternatively, followed by a thin AlN layer, compositionally graded AlGaN buffer layers have also been used to develop high-quality AlGaN epilayers on Si.[27-29] Phenomenally, with such compositionally graded AlGaN buffer layers, electrically-injected lasers on Si in the near UV band have been demonstrated.[29]

In spite of the progress, there are several issues of the current approaches. For example, for AlN buffer layers on patterned Si substrates, the patterning adds additional time- and dollar-cost in the wafer preparation process. Moreover, for the use of multiple buffer layers, the growth process typically takes a long time due to the complexity of the buffer layer structure. In addition, the wafer bowing induced by multiple buffer layers also affects the uniformity across the wafer during the growth. As such, it is desirable to reduce the complexity of the buffer layer.[30, 31]

In this work, we carry out the molecular beam epitaxy (MBE) growth and characterization of AlGaN epilayer on Si with a different buffer layer technology that exploits a nanowire template and an AlN buffer layer through a coalescence process.[32] It is also noted that, compared to many studies on the internal quantum efficiency (IQE) of bulk AlGaN epilayers and AlGaN quantum wells on sapphire and/or AlN-on-sapphire templates,[33-38] such studies are *barely* carried out for AlGaN epilayers on Si, which is nonetheless critical to further improve the device performance. Therefore, in this work, we further present a detailed study on the room-temperature IQE of bulk

AlGaN epilayer, including the analysis on the intrinsic IQE as a function of the excitation and the efficiency droop.

4.1.2. Experiments

In this study, the AlGaN epilayer was grown by radio-frequency (RF) plasma-assisted MBE on n-type Si (111) substrates with a resistivity around 0.005 Ω cm or lower. The schematic is shown in **Figure 4.1 (a)**, which starts with a GaN nanowire template with a thickness of around 200 nm, followed by the growth of the AlN buffer layer through a coalescence process with a thickness of 250 nm, and then the final AlGaN epilayer on top with a thickness of 50 nm. Both the GaN nanowire template and the AlN buffer layer were grown under nitrogen (N)-rich conditions. The substrate temperatures for these two layers were 720 ℃ and 810 ℃, respectively. The use of a relatively low substrate temperature for the AlN buffer layer in the N-rich environment promotes the coalescence of AlN, and our previous studies have shown that using such a nanowire template and coalescence approach, smooth AlN thin films can be obtained.[32] The AlGaN epilayer was grown under metal-rich condition with a substrate temperature of 720 ℃. The Ga flux and Al flux were 1×10^{-7} Torr and 2×10^{-8} Torr, respectively.

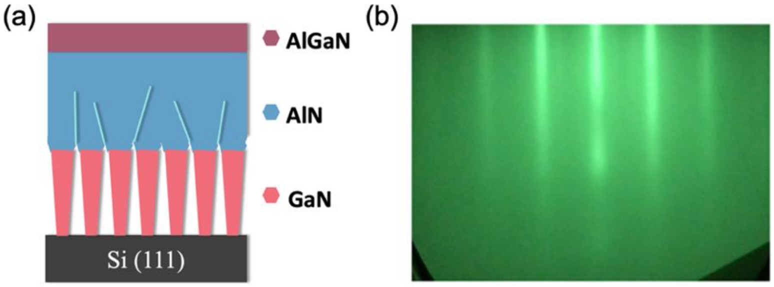

Figure 4.1. (a) Schematic of the AlGaN epilayer grown on Si. (b) The RHEED pattern of AlGaN layer taken along the $\langle 11\bar{2}0\rangle$ direction under metal-rich growth condition.

The structural properties of the grown wafer were characterized by scanning electron microscopy (SEM) and scanning transmission electron microscopy (STEM), as well as X-ray diffraction (XRD). The specimens for the cross-sectional imaging were prepared by the focused ion beam (FIB) etching. A platinum (Pt) protection layer was coated on the sample surface.

The optical properties of the AlGaN epilayer were studied by the power-dependent photoluminescence (PL) experiments at room temperature. A 213 nm pulse laser, with a pulse of 7 ns, was used as the excitation source. A neutral density (ND) filter was used to adjust the laser excitation power. The laser light was focused onto the sample surface through a silica focus lens, and the emitted light from the sample surface was also collected by a silica focus lens, which was further coupled to an optical fiber and a deep UV spectrometer.

4.1.3. Results and Discussion

Figure 4.1 (b) shows the reflection high-energy electron diffraction (RHEED) pattern taken during the growth of the AlGaN epilayer along the $\langle 11\bar{2}0 \rangle$ direction. It is seen that a bright and streaky RHEED pattern is observed, indicating a relatively smooth AlGaN thin film under metal-rich condition.

Figure 4.2 (a) shows a cross-sectional SEM image at a large scale, highlighting the overall cross-sectional structure of the wafer and a relatively smooth surface. **Figure 4.2 (b)** shows the cross-sectional STEM high-angle annular dark-field (HAADF) image, with each layer labeled. It is seen that the coalescence of AlN is complete within the AlN buffer layer, with a few coalescence boundaries. The exemplary coalescence boundaries are marked by arrows. An optical image of the wafer is shown in **Figure 4.2 (c)**, and no cracks can be seen. Our detailed examination further confirms that there are no cracks in the whole wafer.

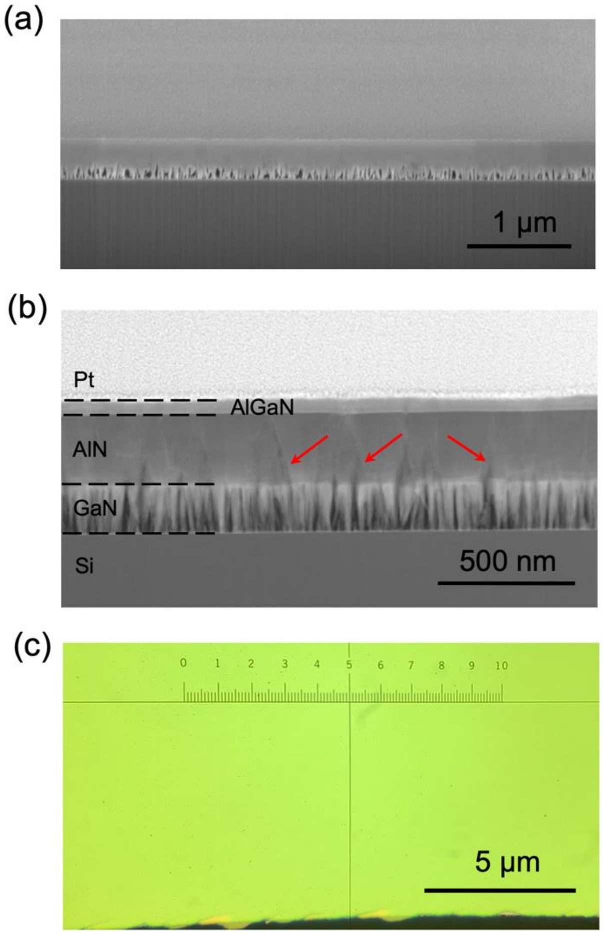

Figure 4.2. (a) and (b) Cross-sectional SEM image at a larger scale and cross-sectional STEM image at a smaller scale of the wafer, respectively. The arrows mark the exemplary coalescence boundaries in the AlN layer. (c) Optical image of the wafer.

The grown wafer was further examined by XRD 2θ-θ scans from 33° to 37°. **Figure 4.3** shows three diffraction peaks at 34.64°, 35.13°, and 36.02°, which correlate to GaN (002), AlGaN (002), and AlN (002) planes, respectively. Compared to the peak position of relaxed GaN (34.57°), the value of the present GaN layer could suggest the presence of a small in-plane tensile strain due to the Si substrate; on the hand, the diffraction peak position of the AlN layer is close to the relaxed value (36.03°) indicating that the present AlN layer is nearly strain-free.[39-42] Moreover, further considering the peak position of the AlGaN layer and assuming that the AlGaN layer is fully strained, the Al content is estimated to be 0.26. This number is consistent with what is derived from PL experiments (to be discussed), indirectly suggesting that the AlGaN layer is highly strained.

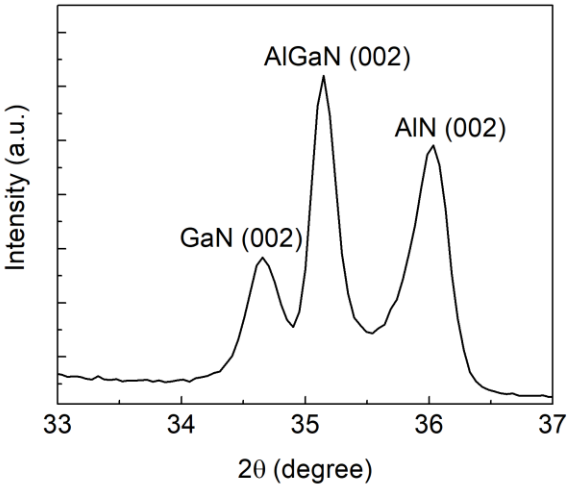

Figure 4.3. XRD 2θ-θ scan of the wafer.

The optical properties of the AlGaN epilayer were further studied by the power-dependent PL experiments at room temperature. **Figure 4.4 (a)** shows the PL spectra under different excitations. The emission peak is around 313 nm, from which we estimated the Al composition using the Vegard's law: by assuming the bandgap energies of GaN and AlN to be 3.42 eV and 6.2 eV, respectively, and the bowing parameter to be 0.7 eV,[43] an Al composition of 0.23 was derived. It is also noted that the PL spectral linewidth is noticeably broader than the previously reported AlGaN epilayers on sapphire with similar Al contents and comparable to the linewidth of AlGaN nanowires, suggesting that strong compositional inhomogeneity and/or compositional fluctuations are present.[35, 44, 45]

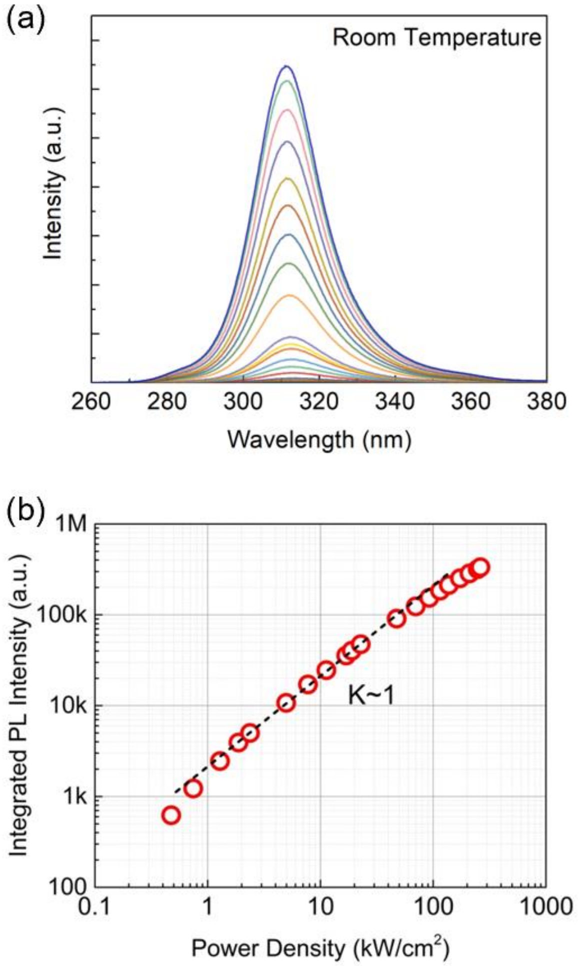

Figure 4.4. (a) PL spectra of the AlGaN sample under different excitations at room temperature. (b) The integrated PL intensity extracted from the power-dependent PL spectra vs the power density.

Figure 4.4 (b) illustrates the integrated PL intensity I_{PL} as a function of the excitation power density in a logarithmic scale. A slope k = 1, which corresponds to the radiative recombination dominated process, is also shown. It is seen the PL emission is governed by the radiative recombination process over a wide range of excitation powers, suggesting a high IQE and low density of structural defects.

We next studied the excitation-dependent room-temperature IQE of the AlGaN epilayer by considering the Shockley–Read–Hall (SRH) nonradiative recombination (An), the bimolecular radiative recombination rate (Bn^2), and the high-order nonradiative recombination rate (Cn^3), where A, B, C are the respective coefficients, and n is the carrier concentration at different excitations. Using the steady-state approximation, the carrier generation rate G is equal to the total recombination rate R, i.e., $G = R = An + Bn^2 + Cn^3$. The generation rate G can be calculated experimentally as follows:

$$G = \frac{P_{Laser}(1-R_F)\alpha}{A_{spot}hv}, \tag{4.1}$$

where A_{spot} (9.0×10^4 μm^2) is laser beam spot size, hv (5.82 eV) is the photon energy of the 213 nm laser, P_{Laser} is the peak pumping power under various excitations, α (2.5×10^5 cm^{-1})[46] is the absorption coefficient of the epilayer, and R_F is the reflectance (18%) estimated by the Fresnel's law. On the other hand, taking the integrated PL intensity I_{PL} in the form of $I_{PL} = \gamma Bn^2$, where I_{PL} can be extracted from the power-dependent PL spectra and γ is a fitting parameter, the carrier concentration can be expressed as $n = \sqrt{\frac{I_{PL}}{\gamma B}}$. Therefore, the generation rate G takes the form:

$$G = \frac{A}{\sqrt{B\gamma}}\sqrt{I_{PL}} + \frac{1}{\gamma}I_{PL} + \frac{C}{\sqrt{(B\gamma)^3}}\sqrt{I_{PL}{}^3}, \tag{4.2}$$

through which, parameter γ can be fitted, and IQE can be calculated via,

$$IQE = \frac{Bn^2}{An+Bn^2+Cn^3} = \frac{I_{PL}}{\gamma G}. \tag{4.3}$$

Figure 4.5 (a) shows the experimentally determined G as a function of I_{PL}, extracted from **Figure 4.4 (a)**, in a logarithmic scale, together with a fitting curve using Equation (4.2). It is seen that an excellent fitting is obtained. **Figure 4.5 (b)** shows the calculated IQE as a function of the generation rate. It is seen that a maximum IQE of around 50% is reached. This high IQE is consistent with the slope suggested in **Figure 4.4 (b)**. In the derivation of IQE with Equation (4.3), as *A*, *B*, and *C* coefficients were not involved, it thus reflects the intrinsic IQE of the present AlGaN epilayer. We have further estimated the carrier density at the peak IQE by taking *B* of 8×10^{-11} cm^3s^{-1}, following the recent studies for bulk AlGaN epilayers with a similar emission wavelength,[47] which yields a carrier density *n* of 3×10^{18} cm^{-3}.

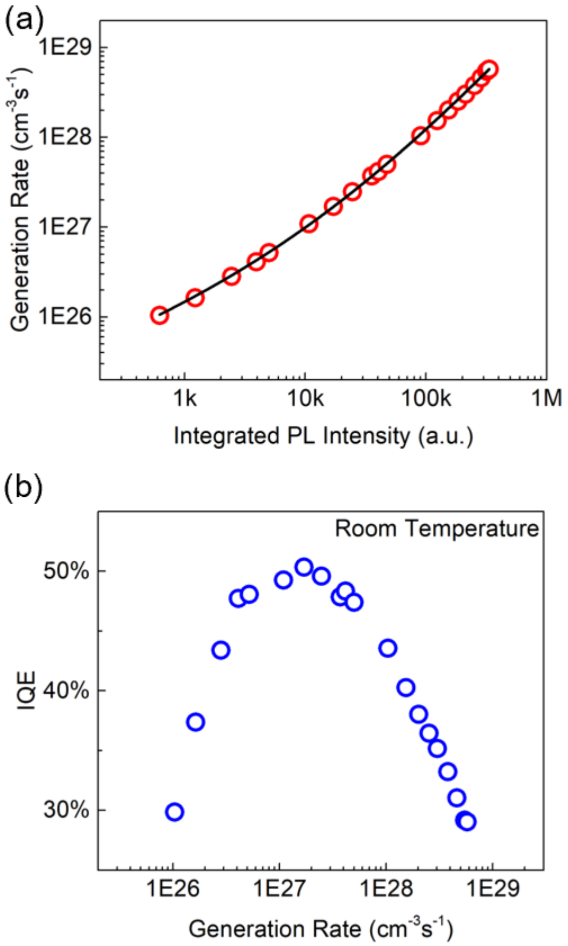

Figure 4.5. (a) Generation rate as a function of the integrated PL intensity. The line represents a fitting curve based on Equation (4.2). (b) The calculated IQE as a function of the generation rate.

This IQE is noticeably higher than the previously reported bulk AlGaN epilayers grown on sapphire and/or AlN-on-sapphire templates.[35, 48, 49] We attribute this IQE improvement mainly to the employment of the unique AlN buffer layer.

An efficiency droop is also seen at mid-excitations. Hitherto, compared to many studies on the efficiency droop of InGaN-based quantum wells and epilayers, the efficiency droop on the AlGaN-based materials is much less studied. Existing studies have suggested carrier delocalization, Auger recombination, heating effect, saturation of the radiative recombination due to the phase-space filling, and carrier leakage as the possible mechanisms for the AlGaN-based materials and devices.[35, 37, 50] Carrier leakage is more relevant to quantum wells and/or under the electrical injection, and is thus not likely related to the droop in the present study. Moreover, due to the use of a pulse laser, heating effect is also not likely the cause.

To further examine carrier delocalization, we have plotted the extracted PL peak energy and full width at half maximum (FWHM) as a function of the power density in **Figures 4.6 (a)** and **4.6 (b)**, respectively. It is seen that as the excitation increases, the PL peak energy is blue-shifted, accompanied by a reduction of FWHM. This blueshift and FWHM narrowing are consistent with the electrostatic screening of the quantum-confined Stark effect (QCSE) as the carrier density increases;[51-54] and the presence of QCSE can be attributed to the presence of compositional inhomogeneity and/or compositional fluctuations as indicated by the PL spectral linewidth (discussed earlier) and the large electric polarization fields in III-nitrides.[55]

These features are nonetheless inconsistent with carrier delocalization, in which blueshift and FHWM increase are expected.[51, 53, 54] However, considering the broad PL spectra, compositional fluctuations are expected and thus carrier delocalization could contribute to the efficiency droop. In this case, the failure in observing a clear increasing trend of FWHM could be related to the strong electric polarization fields. Previous studies have shown that the strong electric polarization fields could screen the observation of the FWHM increase.[53, 54]

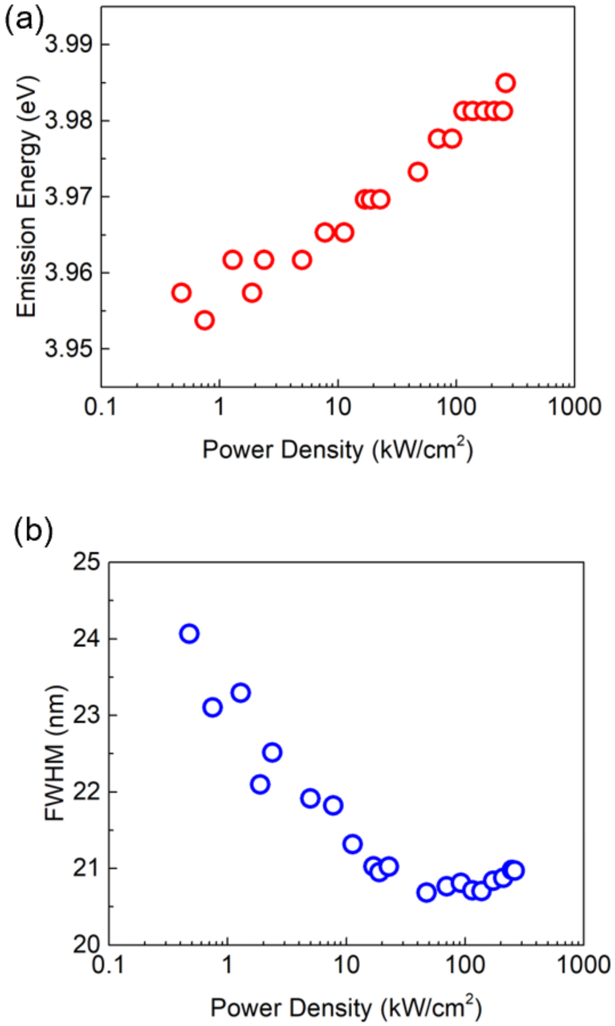

Figure 4.6. (a) The emission peak energy and (b) the FWHM as a function of the pumping power density.

Lastly, the estimated carrier density at the peak IQE is 3×10^{18} cm^{-3}, which might indicate that Auger is not likely the dominant role for the *droop onset*. If taking the lower bound *B* value for the present AlGaN epilayer (2×10^{-11} cm^{3}s^{-1}), the carrier density at the peak IQE is around 6×10^{18} cm^{-3}, again suggesting that Auger might not be the cause. Previous studies on the efficiency droop of AlGaN epilayers on sapphire have suggested that Auger only plays a role if the carrier density is 10^{20} cm^{-3}.[35] Our present study, however, cannot rule out the saturation of the radiative recombination.

4.1.4. Conclusion

In conclusion, we have performed MBE growth and characterization of AlGaN epilayer on Si. A special AlN buffer layer that is formed through a coalescence process on a nanowire template was used, and a relatively smooth AlGaN epilayer was obtained. Further combining the excitation-dependent PL and a theoretical model, the intrinsic room-temperature IQE was derived, which is peaked at ~50%, with an estimated carrier density of 3×10^{18} cm^{-3}. This IQE is significantly improved compared to the previously reported bulk AlGaN epilayers on sapphire and/or AlN-on-sapphire templates, due to the use of the unique AlN buffer layer.

References

1. T. D. Moustakas and R. Paiella, *Rep. Prog. Phys.* **80** (10), 106501 (2017).
2. M. Kneissl, T.-Y. Seong, J. Han and H. Amano, *Nat. Photonics* **13** (4), 233 (2019).
3. H. Amano, R. Collazo, C. D. Santi, S. Einfeldt, M. Funato, J. Glaab, S. Hagedorn, A. Hirano, H. Hirayama, R. Ishii, Y. Kashima, Y. Kawakami, R. Kirste, M. Kneissl, R. Martin, F. Mehnke, M. Meneghini, A. Ougazzaden, P. J. Parbrook, S. Rajan, P. Reddy, F. Römer, J. Ruschel, B. Sarkar, F. Scholz, L. J. Schowalter, P. Shields, Z. Sitar, L. Sulmoni, T. Wang, T. Wernicke, M. Weyers, B. Witzigmann, Y.-R. Wu, T. Wunderer and Y. Zhang, *J. Phys. D: Appl. Phys.* **53** (50), 503001 (2020).
4. M. Kneissl and J. Rass, *III-nitride Ultraviolet Emitters*, volume 227, Chapter 1. Springer, 2016.
5. H. Hirayama, N. Maeda, S. Fujikawa, S. Toyoda and N. Kamata, *Jpn. J. Appl. Phys.* **53** (10), 100209 (2014).
6. E. Monroy, F. Omnes and F. Calle, *Semicond. Sci. Technol.* **18** (4), R33 (2003).
7. D. Li, K. Jiang, X. Sun and C. Guo, Adv. Opt. Photonics **10** (1), 43 (2018).
8. J.-W. Min, D. Priante, M. Tangi, G. Liu, C. H. Kang, A. Prabaswara, C. Zhao, L. Al-Maghrabi, Y. Alaskar, A. M. Albadri, A. Y. Alyamani, T. K. Ng and B. S. Ooi, *J. Nanophotonics* **12** (04), 1 (2018).
9. S. Zhao and Z. Mi, *IEEE J. Quantum Electron.* **54** (6), 1 (2018).
10. S. Zhao, J. Lu, X. Hai and X. Yin, *Micromachines (Basel)* **11** (2), 125 (2020).
11. Y. S. Wu, J.-H. Cheng, W. C. Peng and H. Ouyang, *Appl. Phys. Lett.* **90** (25), 251110 (2007).

12. Y. Sun, T. Yu, H. Zhao, X. Shan, X. Zhang, Z. Chen, X. Kang, D. Yu and G. Zhang, *J. Appl. Phys.* **106** (1), 013101 (2009).

13. E. Cicek, R. McClintock, C. Y. Cho, B. Rahnema and M. Razeghi, *Appl. Phys. Lett.* **103** (18),181113 (2013).

14. S. Raghavan and J. M. Redwing, *J. Appl. Phys.* **96** (5), 2995 (2004).

15. A. Bardhan, N. Mohan, H. Chandrasekar, P. Ghosh, D. V. Sridhara Rao and S. Raghavan, *J. Appl. Phys.* **123** (16), 165108 (2018).

16. A. Bourret, A. Barski, J. L. Rouvière, G. Renaud and A. Barbier, *J. Appl. Phys.* **83** (4), 2003 (1998).

17. S. Yamaguchi, M. Kosaki, Y. Watanabe, Y. Yukawa, S. Nitta, H. Amano and I. Akasaki, *Appl. Phys. Lett.* **79** (19), 3062 (2001).

18. S. Fujikawa and H. Hirayama, *Appl. Phys. Express* **4** (6), 061002 (2011).

19. T. Mino, H. Hirayama, T. Takano, K. Tsubaki and M. Sugiyama, *Appl. Phys. Express* **4** (9), 092104 (2011).

20. Y. Zhang, S. Gautier, C.-Y. Cho, E. Cicek, Z. Vashaei, R. McClintock, C. Bayram, Y. Bai and M. Razeghi, *Appl. Phys. Lett.* **102** (1), 011106 (2013).

21. B. T. Tran and H. Hirayama, *Sci. Rep.* **7** (1), 12176 (2017).

22. J. Shen, X. Yang, D. Liu, Z. Cai, L. Wei, N. Xie, F. Xu, N. Tang, X. Wang, W. Ge and B. Shen, *Appl. Phys. Lett.* **117** (2), 022103 (2020).

23. B. T. Tran, N. Maeda, M. Jo, D. Inoue, T. Kikitsu and H. Hirayama, *Sci. Rep.* **6** (1), 35681 (2016).

24. Y. Huang, J. Liu, X. Sun, X. Zhan, Q. Sun, H. Gao, M. Feng, Y. Zhou, M. Ikeda and H. Yang, *CrystEngComm* **22** (7), 1160 (2020).

25. P. Saengkaew, A. Dadgar, J. Blaesing, T. Hempel, P. Veit, J. Christen and A. Krost, *J. Cryst. Growth* **311** (14), 3742 (2009).

26. M. A. Mastro, C. R. Eddy, D. K. Gaskill, N. D. Bassim, J. Casey, A. Rosenberg, R. T. Holm, R. L. Henry and M. E. Twigg, *J. Cryst. Growth* **287** (2), 610 (2006).

27. Z. Li, L. Liu, Y. Huang, Q. Sun, M. Feng, Y. Zhou, H. Zhao and H. Yang, *Appl. Phys. Express* **10** (7), 072101 (2017).

28. K. Cheng, M. Leys, J. Derluyn, K. Balachander, S. Degroote, M. Germain and G. Borghs, *Phys. Status Solidi C* **5** (6), 1600 (2008).

29. M. Feng, Z. Li, J. Wang, R. Zhou, Q. Sun, X. Sun, D. Li, H. Gao, Y. Zhou, S. Zhang, D. Li, L. Zhang, J. Liu, H. Wang, M. Ikeda, X. Zheng and H. Yang, *ACS Photonics* **5** (3), 699 (2018).

30. J. Cheng, X. Yang, L. Sang, L. Guo, J. Zhang, J. Wang, C. He, L. Zhang, M. Wang, F. Xu, N. Tang, Z. Qin, X. Wang and B. Shen, *Sci. Rep.* **6** (1), 23020 (2016).

31. Y. Li, W. Wang, Y. Lin, X. Li, L. Huang, Y. Zheng, Z. Zhang and G. Li, *Mater. Lett.* **207**, 133 (2017).

32. X. Yin, Q. Zhang and S. Zhao, *Cryst. Growth Des.* **in press** (2021).

33. Z. Bryan, I. Bryan, J. Xie, S. Mita, Z. Sitar and R. Collazo, *Appl. Phys. Lett.* **106** (14), 142107 (2015).

34. K. Ban, J.-i. Yamamoto, K. Takeda, K. Ide, M. Iwaya, T. Takeuchi, S. Kamiyama, I. Akasaki and H. Amano, *Appl. Phys. Express* **4** (5), 052101 (2011).

35. Ž. Podlipskas, R. Aleksiejūnas, A. Kadys, J. Mickevičius, J. Jurkevičius, G. Tamulaitis, M. Shur, M. Shatalov, J. Yang and R. Gaska, *Journal of Physics D: Applied Physics* **49** (14), 145110 (2016).

36. C. Frankerl, M. P. Hoffmann, F. Nippert, H. Wang, C. Brandl, N. Tillner, H.-J. Lugauer, R. Zeisel, A. Hoffmann and M. J. Davies, *J. Appl. Phys.* **126** (7), 075703 (2019).

37. F. Nippert, M. Tollabi Mazraehno, M. J. Davies, M. P. Hoffmann, H.-J. Lugauer, T. Kure, M. Kneissl, A. Hoffmann and M. R. Wagner, *Appl. Phys. Lett.* **113** (7), 071107 (2018).

38. M. Shatalov, W. Sun, R. Jain, A. Lunev, X. Hu, A. Dobrinsky, Y. Bilenko, J. Yang, G. A. Garrett, L. E. Rodak, M. Wraback, M. Shur and R. Gaska, *Semicond. Sci. Technol.* **29** (8), 084007 (2014).

39. M. A. Moram and M. E. Vickers, *Rep. Prog. Phys.* **72** (3), 036502 (2009).

40. W. Kong, W. Y. Jiao, J. C. Li, K. Collar, T. H. Kim, J. H. Leach and A. S. Brown, *Appl. Phys. Lett.* **107** (3), 032102 (2015).

41. E. Bellet-Amalric, C. Adelmann, E. Sarigiannidou, J. L. Rouvière, G. Feuillet, E. Monroy and B. Daudin, *J. Appl. Phys.* **95** (3), 1127 (2004).

42. J. Bläsing, A. Krost, J. Hertkorn, F. Scholz, L. Kirste, A. Chuvilin and U. Kaiser, *J. Appl. Phys.* **105** (3), 033504 (2009).

43. I. Vurgaftman and J. R. Meyer, *J. Appl. Phys.* **94** (6), 3675 (2003).

44. S. Zhao, S. Y. Woo, S. M. Sadaf, Y. Wu, A. Pofelski, D. A. Laleyan, R. T. Rashid, Y. Wang, G. A. Botton and Z. Mi, *APL Mater.* **4** (8), 086115 (2016).

45. A. Pierret, C. Bougerol, S. Murcia-Mascaros, A. Cros, H. Renevier, B. Gayral and B. Daudin, *Nanotechnology* **24** (11), 115704 (2013).

46. D. Brunner, H. Angerer, E. Bustarret, F. Freudenberg, R. Höpler, R. Dimitrov, O. Ambacher and M. Stutzmann, *J. Appl. Phys.* **82** (10), 5090 (1997).

47. M. E. Rudinsky and S. Y. Karpov, *Phys. Status Solidi A* **217** (14), 1900878 (2019).

48. J. Mickevičius, G. Tamulaitis, M. Shur, M. Shatalov, J. Yang and R. Gaska, *Appl. Phys. Lett.* **101** (21), 211902 (2012).

49. X. Yin and S. Zhao, *Phys. Status Solidi B* **257** (12), 2000287. (2020).

50. G. Tamulaitis, J. Mickevičius, K. Kazlauskas, A. Žukauskas, M. S. Shur, J. Yang and R. Gaska, *Phys. Status Solidi C* **8** (7), 2130 (2011).

51. L. Ya-Ju, C. Ching-Hua, K. Chih Chun, L. Po Chun, L. Tien-Chang, K. Hao-Chung and W. Shing-Chung, *IEEE J. Sel. Top. Quantum Electron.* **15** (4), 1137 (2009).

52. S. Zhao, S. M. Sadaf, S. Vanka, Y. Wang, R. Rashid and Z. Mi, *Appl. Phys. Lett.* **109** (20), 201106 (2016).

53. S.-W. Chen, H. Li and T.-C. Lu, *AIP Adv.* **6** (4), 045311 (2016).

54. W.-C. Lai, C.-H. Yen and S.-J. Chang, *Appl. Phys. Express* **6** (10), 102101 (2013).

55. F. Bernardini, V. Fiorentini and D. Vanderbilt, *Phys. Rev. B* **56** (16), R10024 (1997)

4.2 Further Discussions on Internal Quantum Efficiency

4.2.1 Experimental Setup

In the PL measurements used to estimate the Al compositions and RT IQE of AlGaN epilayers, a 213 nm Q-switched diode-pumped solid-state (DPSS) laser, with a pulse width of 7 ns and a repetition rate of 100 Hz, was used. The corresponding experimental setup is shown in **Figure 4.7**. The 213 nm laser beam was focused on the sample surface through a silica focus lens, with a laser beam spot size of around 300 μm by 300 μm. The emitted light was collected by an optical fiber through a second focus lens and analyzed by a deep UV spectrometer. A neutral density filter was inserted before the sample to adjust different excitation powers on the sample surface. For the study of defect PL bands in Chapter 6, the same PL setup was used, but with a broad-band spectrometer to capture long-wavelength emissions from defects.

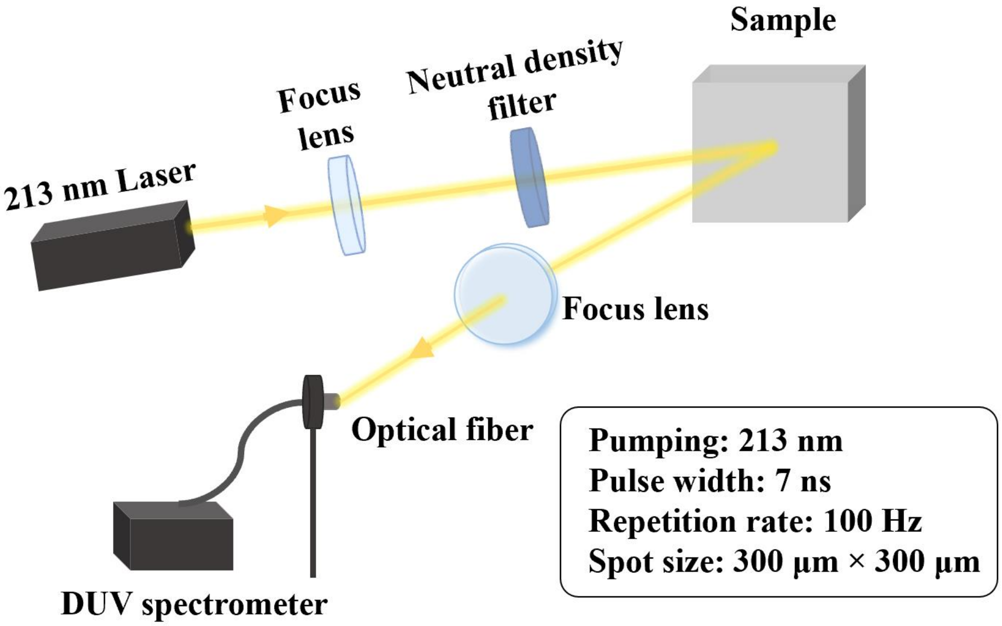

Figure 4.7. Schematic of the PL measurement setup with a 213 nm laser. The light emission is collected from the top surface of the sample.

4.2.2 B Coefficient

With the obtained fitting parameter γ, the carrier concentration n could be determined by assuming the radiative recombination coefficient B. As such, B coefficient plays a critical role in understanding carrier concentration dependent efficiency. The typical radiative recombination coefficient B values have been reported to be in the range of 2.0×10^{-11} to 1.0×10^{-10} cm^{3}s^{-1} [97, 110, 195]. Therefore, taking the B coefficient as 2.0×10^{-11} cm^{3}s^{-1} would give the worst-case scenario of the carrier concentration estimation (i.e., the upper limit). In addition, recent comparative studies on the recombination coefficients of bulk AlGaN epilayers and AlGaN QWs suggest that B coefficient is Al-content-dependent [196, 197]. The corresponding suggested B coefficient values as a function of emission wavelength are illustrated in **Figure 4.8** [197]. Thus, the Al composition of the bulk AlGaN epilayers and QWs should also be taken into consideration when choosing a proper B coefficient value for the carrier concentration calculation in this IQE analysis.

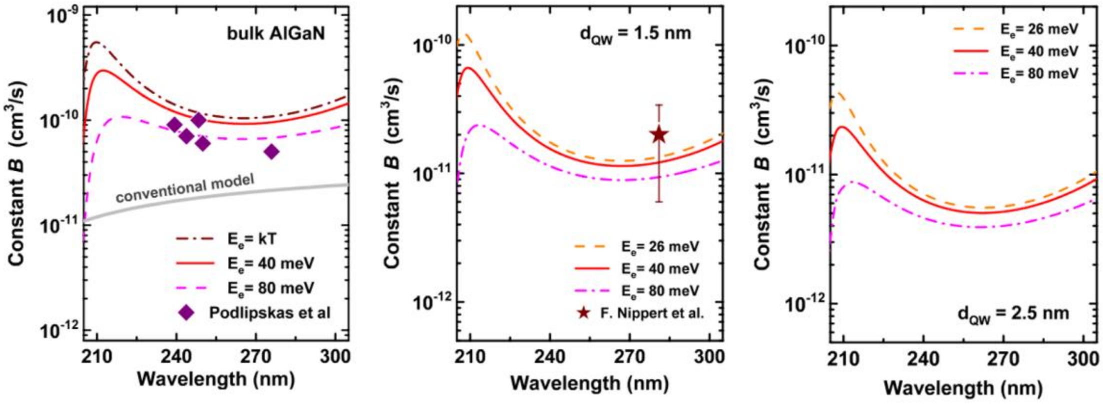

(a) (b) (c)

Figure 4.8. Radiative recombination coefficient B calculated for (a) bulk AlGaN epilayers, AlGaN QWs with the width of (b) 1.5 nm, and (c) 2.5 nm as a function of emission wavelength. Lines are calculations and the thick gray line is the result predicted by the conventional model. The symbols

in (a) and (b) are experimental points from Ref. [196] and Ref. [198], respectively. Reproduced with permission [197]. Copyright 2019, John Wiley and Sons.

It is also important to note that the obtained RT IQE values based on this model [110] are intrinsic IQE values, which do not depend on the different combination choices of the *A*, *B*, and *C* coefficients. In other words, different groups of the coefficients *A*, *B*, and *C* could give equally good fitting in this model, making the *B* coefficient determines the rest (i.e., *A* and *C* coefficients) valid. It is also worth noting that the *A* coefficient is the nonradiative recombination coefficient, which is closely related to the TDD level of the material. As shown in **Figure 4.9**, with the determined *A* coefficient values, one can roughly estimate the TDD levels of the AlGaN epilayers. The model accuracy will be more dependent on the parameters assumed in the experimentally dependent generation rate calculation as well as the recombination coefficient *B* value chosen, as long as an excellent fitting is achieved.

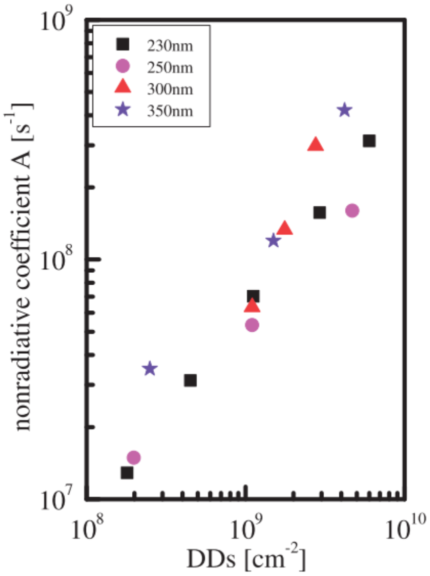

Figure 4.9. Nonradiative recombination coefficient *A* as a function of dislocation densities in AlGaN epilayers. Reproduced with permission [97]. Copyright 2008, IOP Publishing.

Chapter 5

Optical Quality and Stimulated Emission of Optically Pumped 298 nm Laser on Sapphire

To date, the research of AlGaN UV lasers mainly relies on MOCVD. Compared with MOCVD, MBE offers several advantages such as ultrahigh vacuum and separate controls on the substrate temperature and source temperatures; however, deep UV lasing with MBE-grown AlGaN is barely reported [66]. In addition, the RT IQE of AlGaN epilayers grown by MBE is often estimated via temperature-dependent PL intensity that assumes the LT IQE as unity [199, 200]; however, this is not necessarily a valid assumption [198].

In this Chapter, we follow the track of MBE-grown AlGaN and report the stimulated deep UV emission from AlGaN/AlN DH. Power-dependent PL was combined with a theoretical Shockley-Read-Hall (SRH) model to derive the RT IQE, which is argued to be sufficient in determining RT IQE [110, 192, 201].

5.1 Manuscript

The following manuscript was published in *Physics Status Solidi B* (X. Yin and S. Zhao, "Optical Quality and Stimulated Emission of Molecular Beam Epitaxy Grown AlGaN in the Deep Ultraviolet," *physica status solidi (b),* vol. 257, no. 12, pp. 2000287, 2020, doi: 10.1002/pssb.202000287).

This manuscript studies the optical quality and stimulated emission of AlGaN DH on sapphire, with a lasing wavelength of 298 nm and threshold of 950 kW/cm^2. The relatively large lasing threshold is mainly limited by the high TDDs resulted from the lattice mismatch with sapphire substrate.

Optical Quality and Stimulated Emission of Molecular Beam Epitaxy Grown AlGaN in the Deep Ultraviolet

*Xue Yin and Songrui Zhao**

3480 University Street, Montreal, Quebec H3A 0E9, Canada

E-mail: songrui.zhao@mcgill.ca

Abstract: In this work, the optical quality and stimulated emission of aluminum gallium nitride (AlGaN)/AlN double heterostructure grown by molecular beam epitaxy in the deep ultraviolet (UV) are reported. The room temperature internal quantum efficiency at a carrier density of 1×10^{18} cm^{-3} is around 12%, mainly limited by dislocations. For such as-grown wafers, spectral narrowing and nonlinearity of the light output were measured from the wafer edge, with the transverse-electric (TE)-polarized component becoming dominant as the excitation increases. With cleaving, edge-emitting lasing at 298 nm is measured, with an estimated threshold of 0.95 MW cm^{-2}.

Keywords: aluminum gallium nitride (AlGaN), internal quantum efficiency, stimulated emission, ultraviolet

5.1.1. Introduction

Aluminum gallium nitride (AlGaN) alloys, due to their direct, tunable, and ultrawide bandgap energies (≈3.4 – 6.2 eV), have received wide attention in the past for the development of semiconductor-based ultraviolet (UV) light-emitting devices, including light-emitting diodes (LEDs) and lasers, which are pivotal for future generation UV light-emitting technologies, for applications related to high-density data storage, non-line-of-sight (NLOS) communications, biochemical/chemical sensing, UV curving, UV spectroscopy, just to mention a few.[1-8] The main drive to develop AlGaN-based UV light-emitting technologies is to make compact, efficient, and environmental-friendly UV light sources, compared to today's dominant UV light-emitting technologies which mainly rely on low and medium pressure mercury UV lamps and excimer lasers based on fluoride mixtures.

Albeit several major technological hurdles, including high dislocation and defect densities in AlGaN epilayers, difficulty in obtaining AlGaN layers with sufficient p-type conduction as the Al content increases, asymmetric carrier transport induced carrier leakage, unfavorable optical and electrical polarizations, and small refractive index differences,[3] tremendous progress has been made in AlGaN UV LED and lasers by metalorganic chemical vapor deposition (MOCVD). For example, AlGaN quantum well (QW) deep UV LEDs with external quantum efficiencies in the range of 10-20% have been developed.[9-11] In contrast, however, the development of AlGaN-based deep UV lasers is much slower, and the majority studies focus on optically pumped AlGaN QW lasers.[12-17] It is not until very recently that the electrically-pumped AlGaN QW deep UV laser operating at 271.8 nm was achieved,[18] after the clamping of the lasing wavelength at 336 nm for more than one decade.[19-20]

Different from MOCVD, molecular beam epitaxy (MBE) offers ultra-high vacuum environment that could minimize impurity incorporation, as well as separate controls on the substrate and source temperatures and lower growth rate, which can provide excellent control on the heterointerface properties. In addition, recent studies also suggest that MBE may favor p-type dopant (Mg) incorporation,[21-22] which is beneficial for electrically injected light-emitting devices with high Al content AlGaN alloys. In recent years, AlGaN QW UV LEDs grown by MBE have been developed.[23-26] Moreover, InGaN QW lasers by MBE in the visible spectral range have also been reported.[27] However, comparing that many research groups have reported deep UV lasing using MOCVD-grown AlGaN, few groups have demonstrated deep UV lasing using MBE-grown AlGaN.[28-29] In addition, the room temperature internal quantum efficiency (IQE) of AlGaN epilayers grown by MBE is often evaluated by the temperature-dependent photoluminescence (PL) intensity,[30-31] assuming that the low-temperature IQE is unity, which is, however, not necessarily a valid assumption.[32]

In this article, we follow the track of MBE-grown AlGaN. We first investigate the IQE of AlGaN/AlN double heterostructure (DH) through analyzing the room temperature power dependent PL intensity combining with the Shockley-Read-Hall (SRH) model, which is argued to be sufficient in determining the room temperature IQE.[33-35] We further show lasing in the deep UV from the MBE-grown AlGaN/AlN DH at room temperature. Different from the previous work,[28] here, we use the AlN-on-sapphire template and a thin (200 nm) AlN buffer layer, to reduce the growth duration for the desired structures. The as-grown wafer shows a spectral linewidth narrowing and nonlinearity of the light output, indicating a light amplification. Lasing action was measured from the cleaved wafer at 298 nm, with an estimated threshold of 0.95 MW cm^{-2}. In the current study, the lasing threshold is presumably mainly limited by large dislocation densities, as suggested by the relatively large nonradiative recombination coefficient (≈5.8×10^{8} s^{-1}) derived from the power-dependent PL experiments and the SRH model.

5.1.2. Experimental

The AlGaN/AlN DH was grown by radio-frequency (RF) plasma-assisted MBE on the AlN-on-sapphire template. Before loading the substrate to the MBE chamber, standard solvent cleaning was performed, followed by hydrofluoric acid etching. After an *in situ* thermal outgas of the substrate, a 200 nm thick AlN layer was grown. The growth condition included a growth temperature of 750 ℃, a nitrogen flow rate of 0.3 sccm, and an Al flux of 4×10^{-8} Torr. This was followed by the growth of a 100 nm thick AlGaN active layer under a growth temperature of 690 ℃, a nitrogen flow rate of 0.3 sccm, and Al and Ga fluxes of 1.5×10^{-8} and 9×10^{-8} Torr, respectively. In the end, a 20 nm thick AlN layer was grown on the top, with the growth condition similar to that of the bottom AlN layer. Such a structure is schematically shown in **Figure 5.1 (a)**. **Figure 5.1 (b)** shows the reflection high-energy electron diffraction (RHEED) pattern during the growth of the AlGaN active layer. It is seen that the streaky RHEED was captured along $\langle 11\bar{2}0\rangle$ direction, suggesting a two-dimensional (2D) growth of the AlGaN layer under the metal-rich condition.[36]

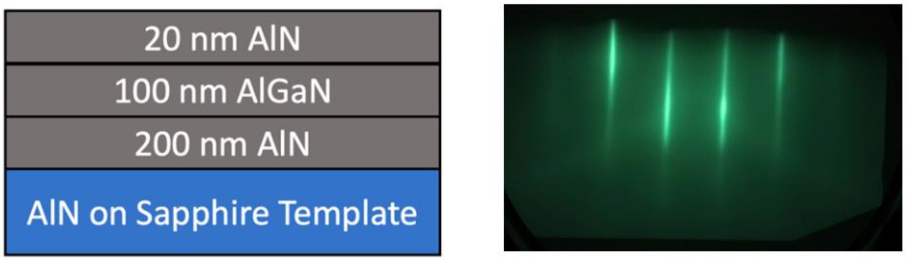

(a) (b)

Figure 5.1. (a) Schematic of the AlGaN/AlN DH. (b) The RHEED pattern taken along $\langle 11\bar{2}0\rangle$ direction during the growth of the AlGaN layer under the metal-rich growth condition.

The optical quality of the AlGaN/AlN DH was examined at room temperature by a 213 nm laser, with a pulse width of 7 ns and a repetition rate of 100 Hz. The laser light was focused to the sample surface through a focus lens, and the emitted light was collected from the sample surface using a focus lens, which was further coupled to an optical fiber and a deep UV spectrometer.

The stimulated emission of the AlGaN/AlN DH was studied by a Nd: YAG 266 nm laser, with a pulse width of 7 ns and a repetition frequency of 10 Hz, at room temperature. The normal incident laser beam was shaped into a rectangle by a cylinder lens, with an estimated beam size of 0.5 by 5 mm. The optical emission was collected from the wafer edge by an optical fiber that was coupled to a deep UV spectrometer. In addition, a Glan-Taylor prism polarizer was inserted between the wafer edge and the optical fiber, to examine if there was any excitation power dependent optical polarization.

5.1.3. Results and Discussion

Figure 5.2 (a) shows the peak power dependent PL spectra measured at room temperature. It is seen that a PL peak at around 295 nm is measured; as the excitation power increases, the PL peak is blueshifted. Using the PL peak position, the Al content in the AlGaN layer can be estimated via Vegard's law,

$$E_g(Al_xGa_{1-x}N\ ) = (1-x)E_g(GaN) + xE_g(AlN) - x(1-x)C_B, \tag{5.1}$$

where $E_g(Al_xGa_{1-x}\mathrm{N}\ )$ is the PL peak energy converted from the PL peak position under an excitation of 3.2 kW cm^{-2}, $E_g(GaN)$ and $E_g(AlN)$ are the respective bandgap energies of GaN and AlN, and C_B is the bowing parameter. By assuming C_B to be 0.7 eV, [37-38] the Al content is estimated to be around 0.33.

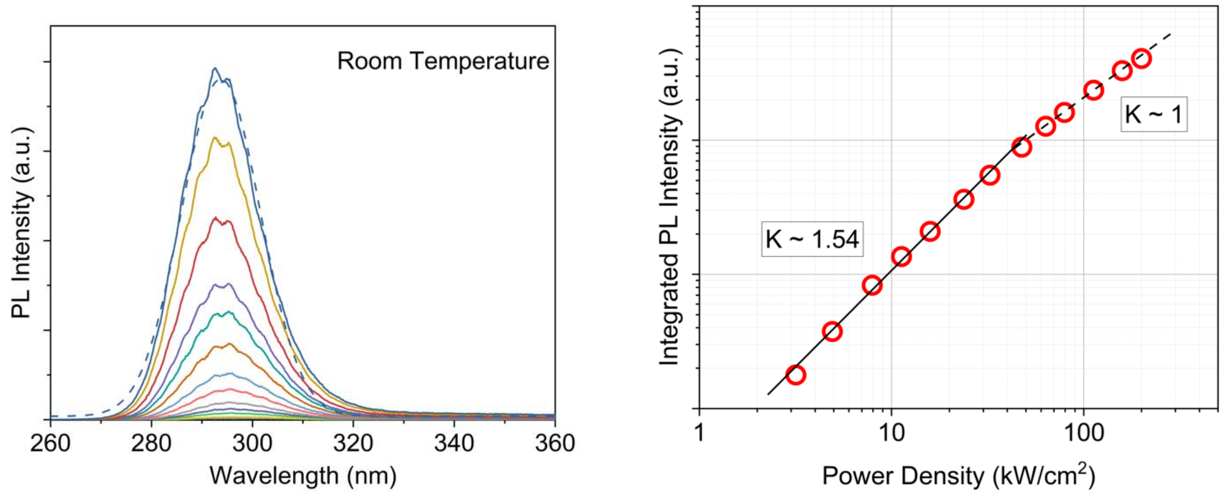

(a) (b)

Figure 5.2. (a) The PL spectra measured from 3.2 to 200 kW cm^{-2} at room temperature. (b) The integrated PL intensity as a function of the excitation power density. The emission is collected from the top surface.

The dashed curve in **Figure 5.2 (a)** is a fitting curve by a single Gaussian peak to the PL spectrum under a peak powder density of 200 kW cm^{-2}. It is seen that the PL spectrum can be fitted well. Using this approach, we obtained the integrated PL intensity (I_{PL}) under different excitations. **Figure 5.2 (b)** shows I_{PL} as a function of the peak power density in a logarithmic plot. A transition from the nonradiative recombination dominated regime to the radiative recombination dominated regime can be told by the slope change from $k \approx 1.54$ to $k \approx 1$.

We then analyzed the IQE using the SRH model.[33-34, 39] At steady state, carrier generation rate can be linked to the recombination coefficients via,

$$G = R = An + Bn^2 + Cn^3, \tag{5.2}$$

where G represents the generation rate; R is the recombination rate; n is the carrier concentration; and A, B and C represent the SRH nonradiative recombination coefficient, the bimolecular radiative recombination coefficient, and the higher-order nonradiative recombination coefficient, respectively. Further expressing I_{PL} as $I_{PL} = \gamma B n^2$, G can be written as,

$$G = \frac{A}{\sqrt{B\gamma}}\sqrt{I_{PL}} + \frac{1}{\gamma} I_{PL} + \frac{C}{\sqrt{(B\gamma)^3}}\sqrt{I_{PL}{}^3}, \tag{5.3}$$

where γ is a fitting parameter related to the PL collection efficiency and the active region volume. Separately, G can be determined experimentally by,

$$G = \frac{P_{Laser}(1-R_F)\alpha}{A_{spot} h\nu}, \tag{5.4}$$

where $A_{spot} = 9.0 \times 10^4\ \mu\mathrm{m}^2$ is the spot size of the laser beam, $h\nu = 5.82$ eV is the photon energy of the 213 nm excitation laser, P_{Laser} is the peak power under different excitations, $\alpha = 2.5 \times 10^5\ \mathrm{cm}^{-1}$ is the absorption coefficient of the AlGaN layer, and $R_F = 18\%$ is the Fresnel reflection, estimated through the Fresnel's law.[40]

Therefore, by fitting the experimentally determined G versus I_{PL} with Eq. (3), one can determine A, C, and n; and the IQE can be further calculated via IQE = Bn^2/G. The typical range for B is from $2.0 \times 10^{-11}\ \mathrm{cm}^3\ \mathrm{s}^{-1}$ to $1.0 \times 10^{-10}\ \mathrm{cm}^3\ \mathrm{s}^{-1}$.[33-34, 39] If taking the lower bound value of B ($2.0 \times 10^{-11}\ \mathrm{cm}^3\ \mathrm{s}^{-1}$) and hence the lower bound of the room temperature IQE for a comparison purpose to the previous studies,[34, 39] the best fitting gives $A = 2.9 \times 10^8\ \mathrm{s}^{-1}$, $C = 3.9 \times 10^{-31}\ \mathrm{cm}^6\ \mathrm{s}^{-1}$, and an IQE of ≈7% at a carrier density of $1\times10^{18}\ \mathrm{cm}^{-3}$.

Recent comparative studies on the recombination coefficients between the thick AlGaN epilayers and QWs suggest an Al-content-dependent B coefficient; and for thick AlGaN epilayers emitting at around 295 nm, the B coefficient is suggested to be $\approx 8.0 \times 10^{-11}\ \mathrm{cm}^3\ \mathrm{s}^{-1}$.[41, 42] Using this B value, the best fitting gives $A = 5.8 \times 10^8\ \mathrm{s}^{-1}$ and $C = 3.1 \times 10^{-30}\ \mathrm{cm}^6\ \mathrm{s}^{-1}$. The calculated IQE as a function of n is shown in **Figure 5.3**. The relatively low IQE (≈12%) at a carrier density of $1\times10^{18}\ \mathrm{cm}^{-3}$ is limited by the relatively large nonradiative recombination coefficient A, which is higher than the previously reported AlGaN QWs emitting at around 300 nm by MOCVD.[39] The relatively large *A* coefficient in the current study is mainly limited by a high density of threading dislocations, estimated in the range of $2 – 6 \times 10^9$ cm^{-2}. Moreover, the large *C* coefficient might be attributed to carrier delocalization, Auger recombination, and other effects.[41, 42]

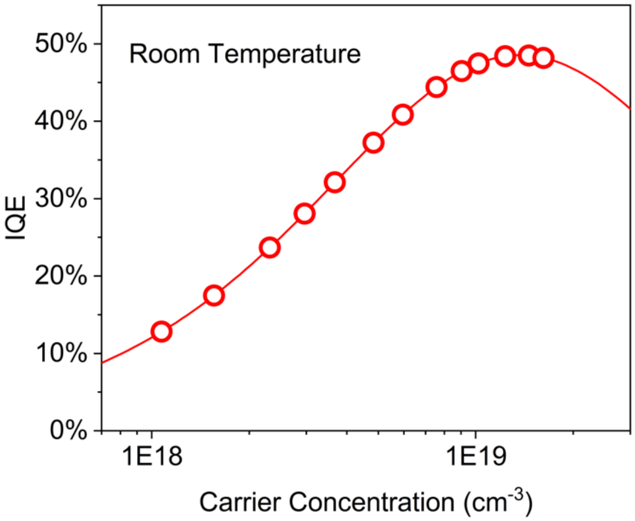

Figure 5.3. The calculated IQE as a function of the carrier concentration. The solid curve is an extrapolated curve based on the derived coefficients.

To examine, if there is any light amplification of the AlGaN/AlN DH, the as-grown wafer was further pumped by the 266 nm laser. The solid and dashed curves in **Figure 5.4 (a)** represent the transverse-electric (TE)- and transverse-magnetic (TM)-polarized light emission spectra, respectively. The extracted light intensity for both components is shown in the upper panel of **Figure 5.4 (b)**. A nonlinearity of the light intensity for the TE-polarized component can be seen clearly, suggesting the presence of a light amplification; in contrast, the TM-polarized component has remained linear. This is also an indication that the light emission becomes more TE-polarized as the increase of the excitation. Moreover, as the excitation increases, the TE-polarized light exhibits a noticeable narrowing (from ≈18 nm to 5 nm), as indicated by both **Figure 5.4 (a)** and the lower panel of **Figure 5.4 (b)**. In contrast, the TM-polarized component does not exhibit a pronounced narrowing and the emission spectrum at the highest excitation power (≈23 MW cm^{-2}) has remained broad (≈12 nm). We have also examined the light emission collected from the top surface, and no light amplification was observed, further suggesting that the light amplification observed from the wafer edge is due to the in-plane optical gain as the light propagates. These features, therefore, suggest that the TE-polarized component receives a higher gain compared to the TM-polarized component and experiences an amplification, resembling the previously demonstrated optically pumped lasing from AlGaN QW structures.[12, 28, 43-46]

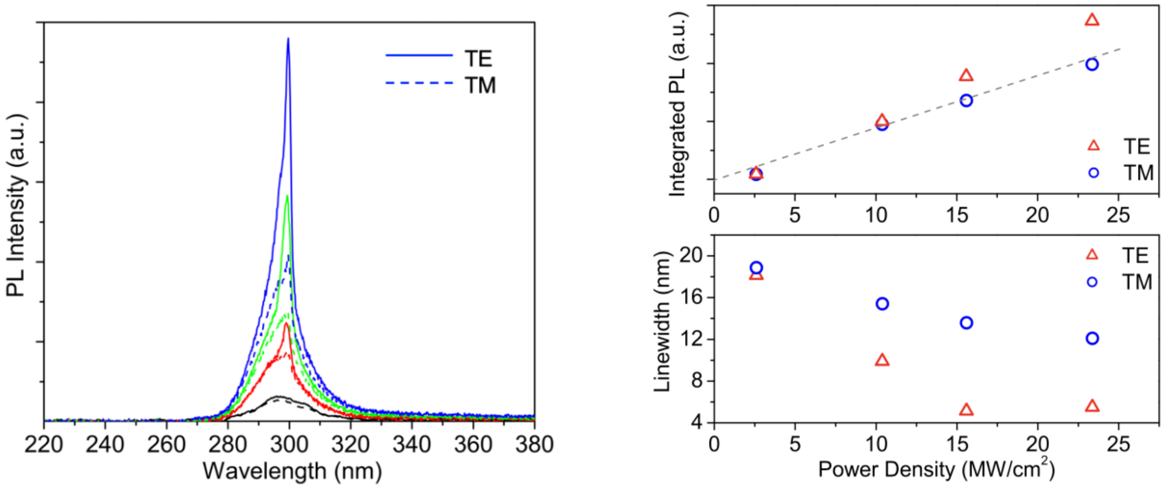

(a) (b)

Figure 5.4. (a) TE- (solid curves) and TM- (dashed curves) polarized components under the excitation power from 2.5 to 23 MW cm^{-2} on the as-grown wafer. TE and TM emissions were collected under the same excitation power. The powers are specified in the lower panel of (b). The emission was collected from the wafer edge. (b) The extracted light intensity and spectral linewidth for TE- and TM-polarized components, respectively. The dashed line is a guide for the eye.

We further measured the light emission from the cleaved wafer. The emission spectra under different excitation powers are shown in **Figure 5.5**. It is seen that a sharp peak around 298 nm appears as the increase of the excitation. The spectral linewidth reduces from around 10 nm to 2.5 nm as the excitation increases from 0.77 to 2 MW cm^{-2} (inset of **Figure 5.5**). This linewidth reduction is similar to the previously reported optically pumped AlGaN QW lasers.[12, 14, 17, 44, 46]

The lasing threshold, estimated from the *L*-*L* (light-in – light-out) curve, is around 0.95 MW cm^{-2}, shown by the inset of **Figure 5.5**. After the threshold, the light output increases linearly. The large threshold in the current study could be ascribed to the relatively large dislocation densities, as suggested by the relatively large nonradiative recombination coefficient.

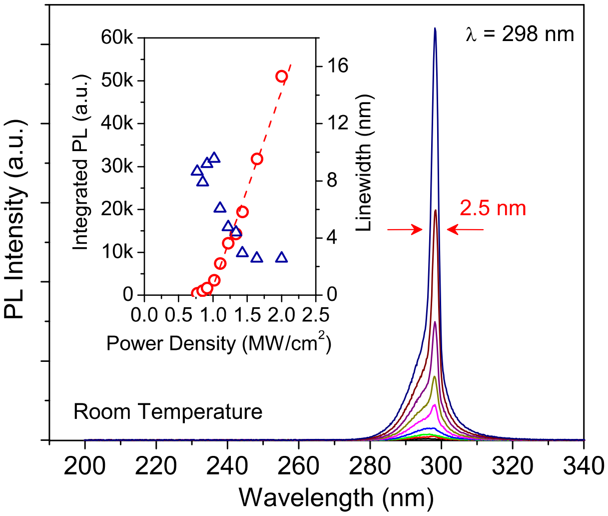

Figure 5.5. Emission spectra under the excitation power varying from 0.77 to 2 MW cm^{-2} on the cleaved sample at room temperature. The emission was collected from the wafer edge. The inset shows the integrated PL intensity and the spectral linewidth as a function of the excitation power density. The dashed line is a guide for the eye.

5.1.4. Conclusion

In conclusion, we have examined the optical quality of the MBE-grown AlGaN/AlN DH through analyzing the room temperature IQE using the power dependent PL intensity and the SRH model. The relatively low IQE at low injections is mainly limited by dislocations. Lasing at 298 nm was further measured from such AlGaN/AlN DH. The lasing threshold was estimated to be around 0.95 MW cm^{-2}. Further improvement can be obtained by using strategies such as using dislocation density filters to reduce dislocations.

References

[1] T. D. Moustakas, R. Paiella, *Rep. Prog. Phys.* **2017**, *80*, 106501.

[2] M. Kneissl, T.-Y. Seong, J. Han, H. Amano, *Nat. Photon.* **2019**, *13*, 233.

[3] M. Kneissl, J. Rass, *III-Nitride ultraviolet emitters*, Springer, **2016**.

[4] M. Kneissl, T. Kolbe, C. Chua, V. Kueller, N. Lobo, J. Stellmach, A. Knauer, H. Rodriguez, S. Einfeldt, Z. Yang, N. M. Johnson, M. Weyers, *Semicond. Sci. Technol.* **2011**, *26*, 014036.

[5] H. Hirayama, *Recent Progress in AlGaN Deep-UV LEDs*, **2018**, Ch. 7.

[6] K. B. Asif KhAn, Tom KATonA *Nat. Photon.* **2018**, *2*, 77.

[7] D. Li, K. Jiang, X. Sun, C. Guo, *Adv. Opt. Photon.* **2018**, *10*, 43.

[8] C.-H. Liao, H. Sun, X. Li in *Ultraviolet quantum well lasers*, **2019**, Ch. 6.

[9] T. Takano, T. Mino, J. Sakai, N. Noguchi, K. Tsubaki, H. Hirayama, *Appl. Phys. Express* **2017**, *10*, 031002.

[10] M. Ichikawa, A. Fujioka, T. Kosugi, S. Endo, H. Sagawa, H. Tamaki, T. Mukai, M. Uomoto, T. Shimatsu, *Appl. Phys. Express* **2016**, *9*, 072101.

[11] M. Shatalov, W. Sun, A. Lunev, X. Hu, A. Dobrinsky, Y. Bilenko, J. Yang, M. Shur, R. Gaska, C. Moe, G. Garrett, M. Wraback, *Appl. Phys. Express* **2012**, *5*, 082101.

[12] X.-H. Li, T.-T. Kao, M. M. Satter, Y. O. Wei, S. Wang, H. Xie, S.-C. Shen, P. D. Yoder, A. M. Fischer, F. A. Ponce, T. Detchprohm, R. D. Dupuis, *Appl. Phys. Lett.* **2015**, *106*, 041115.

[13] J. Yan, Y. Tian, X. Chen, Y. Zhang, J. Wang, J. Li, *Phys. Stat. Sol. (c)* **2016**, *13*, 228.

[14] W. Guo, Z. Bryan, J. Xie, R. Kirste, S. Mita, I. Bryan, L. Hussey, M. Bobea, B. Haidet, M. Gerhold, R. Collazo, Z. Sitar, *J. Appl. Phys.* **2014**, *115*, 103108.

[15] M. Lachab, K. Balakrishnan, B. Zhang, J. Dion, Q. Fareed, V. Adivarahan, A. Khan, *Appl. Phys. Express* **2011**, *4*, 082103.

[16] R. Kirste, Q. Guo, J. H. Dycus, A. Franke, S. Mita, B. Sarkar, P. Reddy, J. M. LeBeau, R. Collazo, Z. Sitar, *Appl. Phys. Express* **2018**, *11*, 082101.

[17] M. Lachab, W. Sun, R. Jain, A. Dobrinsky, M. Gaevski, S. Rumyantsev, M. Shur, M. Shatalov, *Appl. Phys. Express* **2017**, *10,* 012702.

[18] Z. Zhang, M. Kushimoto, T. Sakai, N. Sugiyama, L. J. Schowalter, C. Sasaoka, H. Amano, *Appl. Phys. Express* **2019**, *12*, 124003.

[19] H. Yoshida, Y. Yamashita, M. Kuwabara, H. Kan, *Appl. Phys. Lett.* **2008**, *93*, 241106.

[20] H. Yoshida, Y. Yamashita, M. Kuwabara, H. Kan, *Nat. Photon.* **2008**, *2*, 551.

[21] B. P. Gunning, C. A. M. Fabien, J. J. Merola, E. A. Clinton, W. A. Doolittle, S. Wang, A. M. Fischer, F. A. Ponce, *J. Appl. Phys.* **2015**, *117*, 045710.

[22] S. Zhao, A. T. Connie, M. H. Dastjerdi, X. H. Kong, Q. Wang, M. Djavid, S. Sadaf, X. D. Liu, I. Shih, H. Guo, Z. Mi, *Sci. Rep.* **2015**, *5*, 8332.

[23] S. A. Nikishin, M. Holtz, H. Temkin, *Japanese J. Appl. Phys.* **2005**, *44*, 7221.

[24] A. Pandey, W. J. Shin, J. Gim, R. Hovden, Z. Mi, *Photon. Res.* **2020**, *8*, 331.

[25] Y. Liao, C. Thomidis, C.-k. Kao, T. D. Moustakas, *Appl. Phys. Lett.* **2011**, *98,* 081110.

[26] V. N. Jmerik, T. V. Shubina, A. M. Mizerov, K. G. Belyaev, A. V. Sakharov, M. V. Zamoryanskaya, A. A. Sitnikova, V. Y. Davydov, P. S. Kop'ev, E. V. Lutsenko, N. V. Rzheutskii, A. V. Danilchik, G. P. Yablonskii, S. V. Ivanov, *J. Cryst. Growth* **2009**, *311*, 2080.

[27] C. Skierbiszewski, M. Siekacz, H. Turski, G. Muzioł, M. Sawicka, A. Feduniewicz-Żmuda, J. Smalc-Koziorowska, P. Perlin, S. Grzanka, Z. R. Wasilewski, R. Kucharski, S. Porowski, *J. Vac. Sci. Technol. B* **2012**, *30,* 02b102.

[28] V. N. Jmerik, E. V. Lutsenko, S. V. Ivanov, *Phys. Stat. Soli. (a)* **2013**, *210,* 439.

[29] S. Zhao, Z. Mi, *IEEE J. Quantum Electron.* **2018**, *54*, 1.

[30] A. Bhattacharyya, T. D. Moustakas, L. Zhou, D. J. Smith, W. Hug, *Appl. Phys. Lett.* **2009**, *94,* 181907.

[31] D. A. Laleyan, X. Liu, A. Pandey, W. J. Shin, E. T. Reid, K. Mashooq, M. Soltani, Z. Mi, *J. Cryst. Growth* **2019**, *507*, 87.

[32] F. Nippert, M. Tollabi Mazraehno, M. J. Davies, M. P. Hoffmann, H.-J. Lugauer, T. Kure, M. Kneissl, A. Hoffmann, M. R. Wagner, *Appl. Phys. Lett.* **2018**, *113,* 071107.

[33] Q. Dai, M. F. Schubert, M. H. Kim, J. K. Kim, E. F. Schubert, D. D. Koleske, M. H. Crawford, S. R. Lee, A. J. Fischer, G. Thaler, M. A. Banas, *Appl. Phys. Lett.* **2009**, *94*, 111109.

[34] Z. Bryan, I. Bryan, J. Xie, S. Mita, Z. Sitar, R. Collazo, *Appl. Phys. Lett.* **2015**, *106,* 142107.

[35] C. Frankerl, M. P. Hoffmann, F. Nippert, H. Wang, C. Brandl, N. Tillner, H.-J. Lugauer, R. Zeisel, A. Hoffmann, M. J. Davies, *J. Appl. Phys.* **2019**, *126,* 075703.

[36] A. A. Toropov, E. A. Shevchenko, T. V. Shubina, V. N. Jmerik, D. V. Nechaev, M. A. Yagovkina, A. A. Sitnikova, S. V. Ivanov, G. Pozina, J. P. Bergman, B. Monemar, *J. Appl. Phys.* **2013**, *114,* 124306.

[37] M. Henini, M. Razeghi, *Optoelectronic Devices: III Nitrides,* Elsevier, **2004**

[38] I. Vurgaftman, J. R. Meyer, *J. Appl. Phys.* **2003**, *94*, 3675.

[39] K. Ban, J.-i. Yamamoto, K. Takeda, K. Ide, M. Iwaya, T. Takeuchi, S. Kamiyama, I. Akasaki, H. Amano, *Appl. Phys. Express* **2011**, *4*, 052101.

[40] D. Brunner, H. Angerer, E. Bustarret, F. Freudenberg, R. Höpler, R. Dimitrov, O. Ambacher, M. Stutzmann, *J. Appl. Phys.* **1997**, *82*, 5090.

[41] Ž. Podlipskas, R. Aleksiejūnas, A. Kadys, J. Mickevičius, J. Jurkevičius, G. Tamulaitis, M. Shur, M. Shatalov, J. Yang, R. Gaska, *J. Phys. D: Appl. Phys*. **2016**, *49*, 145110.

[42] M. E. Rudinsky, S. Y. Karpov, *Phys. Status Solidi (A)* **2019**, 1900878.

[43] W. W. Chow, M. Kneissl, *J. Appl. Phys.* **2005**, *98*, 114502.

[44] S. V. Ivanov, D. V. Nechaev, A. A. Sitnikova, V. V. Ratnikov, M. A. Yagovkina, N. V. Rzheutskii, E. V. Lutsenko, V. N. Jmerik, *Semicond. Sci. Technol.* **2014**, *29*, 084008.

[45] V. N. Jmerik, A. M. Mizerov, A. A. Sitnikova, P. S. Kop’ev, S. V. Ivanov, E. V. Lutsenko, N. P. Tarasuk, N. V. Rzheutskii, G. P. Yablonskii, *Appl. Phys. Lett.* **2010**, *96*, 141112.

[46] V. N. Jmerik, D. V. Nechaev, S. Rouvimov, V. V. Ratnikov, P. S. Kop'ev, M. V. Rzheutski, E. V. Lutsenko, G. P. Yablonskii, M. Aljohenii, A. Aljerwii, A. Alyamani, S. V. Ivanov, *J. Mater. Res.* **2015**, *30*, 2871.

5.2 Optical Pumping Measurements Configuration

The optical pumping of the laser structure as well as the polarization properties were studied by a fourth harmonics 266 nm Nd:YAG laser, with a pulse width of 7 ns and a repetition rate of 10 Hz, at RT. A cylinder lens was placed in front of the sample to shape the laser beam into a rectangular shape with a spot size of around 0.5 mm by 5 mm. A Glan-Taylor prism polarizer was inserted between the sample edge and the optical fiber. The emitted light from the sample edge was then collected by the optical fiber that was coupled with a DUV spectrometer. The schematic of the polarization-dependent PL measurement setup is demonstrated in **Figure 5.6**.

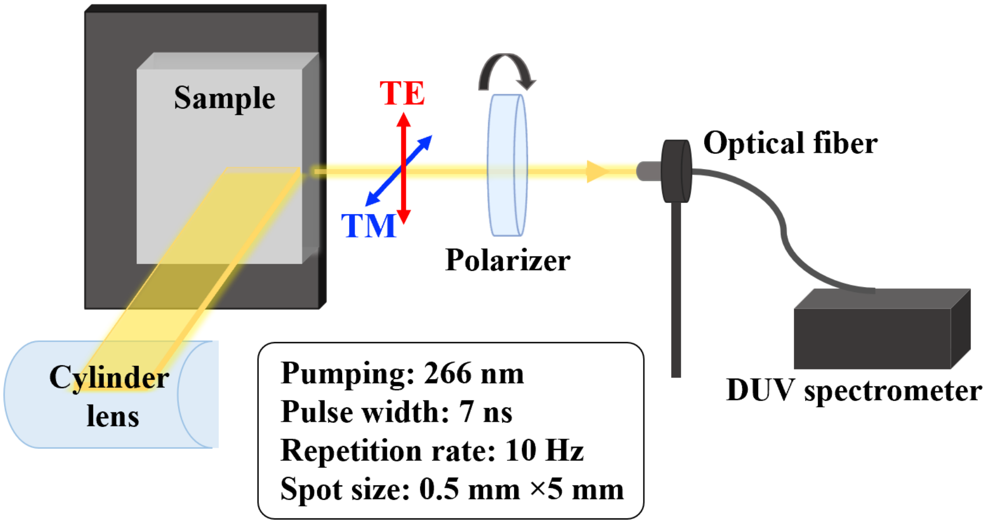

Figure 5.6. Schematic of the PL measurement setup with a 266 nm laser. The light emission is collected from the edge of the sample.

For the study of the lasing characteristics of the sample, the sample was first cleaved into laser bars. A similar experimental setup shown in **Figure 5.6** was used, but without the use of the Glan-Taylor prism polarizer.

Chapter 6

Defect Control and Threshold Reduction of Optically Pumped 287 nm Laser on Sapphire

To achieve high efficiency and low threshold AlGaN UV lasers, both point defects and TDDs play critical roles. Different from TDDs, point defects not only act as nonradiative recombination centers that significantly reduce the quantum efficiency but also cause optical losses, and severely influence the lasing threshold. Nonetheless, few studies on the role of point defects have been carried out, particularly the case for MBE-grown AlGaN lasers.

In this Chapter, we study the influence of defects on the lasing threshold and quantum efficiency, with a main focus on the role of point defects.

6.1 Manuscript

The following manuscript was published in *Physics Status Solidi B* (X. Yin and S. Zhao, "Correlation of Defects and Lasing Threshold for AlGaN Deep Ultraviolet Lasers Grown by Molecular Beam Epitaxy," *physica status solidi (b)*, vol. 258, no.11, pp. 2100201, 2021, doi: 10.1002/pssb.202100201).

The manuscript studies the role of defects on the lasing threshold of MBE-grown AlGaN DH structures. A drastic reduction in the lasing threshold (530 kW/cm^2) has been obtained at 287 nm, compared to our previous study (Chapter 5), via the control of point defects under higher growth temperature.

Correlation of Defects and Lasing Threshold for AlGaN Deep Ultraviolet Lasers Grown by Molecular Beam Epitaxy

*Xue Yin, and Songrui Zhao**

Department of Electrical and Computer Engineering, McGill University
3480 University Street, Montreal, Quebec H3A 0E9, Canada
E-mail: songrui.zhao@mcgill.ca

Abstract: Herein, aluminum gallium nitride (AlGaN)/AlN double-heterostructure (DH) laser at 287 nm with a lasing threshold of 530 kW cm^{-2} is shown. The laser structure is grown on the AlN-on-sapphire template by molecular beam epitaxy. This lasing threshold is drastically reduced compared to the previously reported AlGaN DH lasers at 297 nm with a threshold of around 1 MW cm^{-2}. The detailed studies indicate that this improvement is mainly attributed to the control of defect formation largely due to the increased growth temperature of the AlGaN active layer. The is consistent with the improved internal quantum efficiency at low excitations. Moreover, the control of Al vacancy related point defects is clearly demonstrated by the absence of defect emission in the visible band.

Keywords: aluminum gallium nitride (AlGaN), double-heterostructures, molecular beam epitaxy, point defects, ultraviolet laser

6.1.1. Introduction

Deep ultraviolet (UV) lasers have a broad range of applications, such as lithography, UV curing, sterilization, non-line-of-sight communications (NLOS), optical storage, and so on.[1, 2] In this context, significant research efforts have been devoted in developing compact and reliable semiconductor UV lasers based on aluminum gallium nitride (AlGaN) alloys, due to their tunable, direct, and ultrawide bandgap energies from 3.4 to 6.2 eV.[3-6] However, the realization of the electrically injected AlGaN-based deep UV lasers is a highly challenging task. The underlying impediments are mainly due to the poor material quality, originated from the lattice and thermal mismatches between the AlGaN epilayer and the commonly used substrates, for example, sapphire, as well as the difficulties in p-type doping as the Al composition increases, rooted in the large Mg activation energy and co-doping effects.[7-10]

Much attention has been paid to improving the material quality over the past 20 years, for example, reducing threading dislocation densities (TDDs) on sapphire substrates with various techniques, and TDDs in AlGaN epilayers on sapphire as low as around mid-10^8 cm^{-2} are obtained.[11-14] However, given the enduring challenge of p-type doping, the improved AlGaN epilayer quality is mainly tested by the optically pumped AlGaN quantum well laser structures.[12-27] Nonetheless, the optically pumped laser structures can be further used to examine and optimize the material properties as well as laser design parameters. Today, the lowest lasing thresholds of optically pumped AlGaN deep UV lasers on sapphire are around 100 kW cm^{-2}.[13, 20, 23, 26]

With the use of low-dislocation (TDD $<10^3$ cm^{-2}) bulk AlN substrates, lasing thresholds below 10 kW cm^{-2} have been achieved for the structures lasing around 263 nm.[15, 16] Remarkably, the use of bulk AlN substrates has also led to the successful fabrication of the electrically pumped AlGaN quantum well edge-emitting deep UV lasers at 271.8 nm (threshold around 25 kA cm^{-2}, pulse mode) in 2019,[28] after the shortest lasing wavelength being stuck at 336 nm for a decade.[29] Nevertheless, native bulk AlN substrates are extremely costly and have a small wafer size, making it impractical to use bulk AlN substrates for the development of AlGaN deep UV lasers for the time being. Therefore, further improving the AlGaN epilayer quality on other foreign substrates, for example, sapphire, AlN-on-sapphire template, is still of great interest, given the much lower cost and the readily availability of a large wafer size (up to 12 in.) for mass fabrication.

Moreover, just as controlling TDDs in AlGaN epilayers for the development of AlGaN deep UV lasers, controlling point defects is equally important.[16, 30, 31] This is particularly the case for the ultrawide bandgap high Al content AlGaN alloys wherein various point defects and defect complexes, such as $(V_{III}\text{-complex})^{2-}$, have been both theoretically and experimentally suggested.[8-9, 32-34] However, less attention has been paid to the point defects compared with TDDs. A better understanding of point defects as well as controlling them is clearly necessary for the AlGaN deep UV laser development.

It is also worth noting that, hitherto, the AlGaN deep UV laser structures are mainly grown by metalorganic chemical vapor deposition (MOCVD), and the studies of the AlGaN deep UV lasers grown by molecular beam epitaxy (MBE) are much less.[6]

In this work, we demonstrate AlGaN deep UV lasers on the relatively low-cost AlN-on-sapphire template by MBE. The structure lases at 287 nm with a threshold of 530 kW cm^{-2}, a drastic reduction compared to our previously reported AlGaN UV lasers at 298 nm with a threshold of near 1 MW cm^{-2}.[27] Through detailed studies, we attribute this lasing threshold reduction mainly to the reduced defect formation, due to the use of a relatively high substrate temperature for the AlGaN active region. The reduced defect formation is evidenced by the improved internal quantum efficiency (IQE) at low excitations. The drastic reduction of the Al vacancy complex related point defects is also underpinned, indicated by the absence of the photoluminescence (PL) emission in the visible band.

6.1.2. Experiments

The schematic of the AlGaN/AlN DH is shown in **Figure 6.1 (a)**, which consists of AlN buffer and cladding layers with thicknesses of 200 nm and 20 nm, respectively, as well as a 100-nm-thick AlGaN active region. The DH was grown by radio-frequency (RF) plasma-assisted MBE on the AlN-on-sapphire template. Solvent cleaning and hydrofluoric acid etching were performed before loading the wafer into the MBE growth chamber. Subsequently, the substrate underwent an *in situ* thermal outgassing for surface cleaning. Different from the previous study,[27] the AlGaN active region was grown under a substrate temperature of 720 ℃ – an increase of 30 ℃; the rest of the growth condition was identical, except that the Ga flux was increased to compensate the Ga desorption as the growth temperature increases. The growth was *in situ* monitored by reflection high-energy electron diffraction (RHEED).

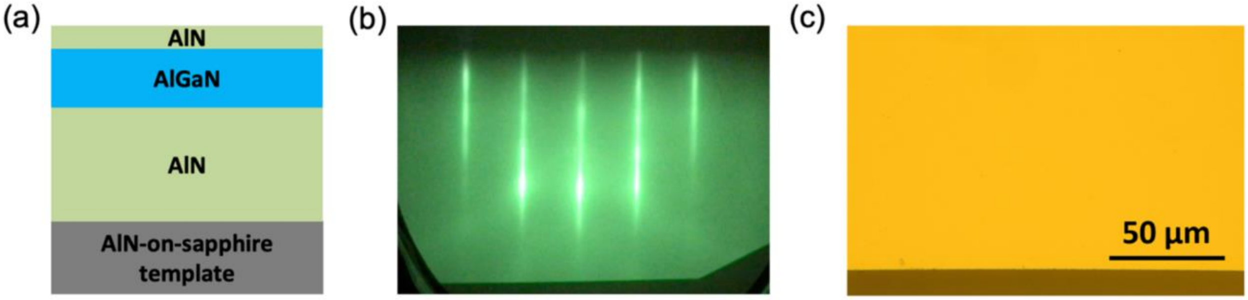

Figure 6.1. (a) The schematic of the AlGaN/AlN DH on the AlN-on-sapphire template. (b) The RHEED pattern taking during the growth of the AlGaN epilayer along the $\langle 11\bar{2}0\rangle$ direction. (c) The optical image of the as-grown wafer.

After the growth, the as-grown wafers were cleaved into laser bars, and the lasing characteristics were studied by a fourth harmonics 266 nm Nd: YAG laser at room temperature (RT). The Nd:YAG laser has a pulse width of 7 ns and a repetition rate of 10 Hz. A cylinder lens was placed in front of the sample to shape the laser beam into a rectangular shape (size around 0.5 by 5 mm). The light emission was then collected by an optical fiber from the cleaved sample edge and further detected by a deep UV spectrometer.

The RT IQE of the as-grown samples was examined by a 213 nm Q-switched diode-pumped solid state (DPSS) laser, with a pulse width of 7 ns. The laser beam was focused onto the sample surface through a silica focus lens. The emitted light from the sample surface was collected by an optical fiber through a focus lens, and analyzed by a deep UV spectrometer. A neutral density filter was used to adjust the excitation density on the sample surface. For the study of defect PL bands, the same PL setup was used, but with a broad-band spectrometer (UV-VIS).

6.1.3. Results and Discussions

Figure 6.1 (b) shows the typical RHEED pattern during the growth. A streaky RHEED pattern was observed throughout the growth, suggesting a smooth surface. The as-grown wafer was also examined under an optical microscope, and an optically smooth surface can be seen (**Figure 6.1 (c)**).

Figure 6.2 (a) shows the power-dependent PL spectra pumped by the Nd:YAG laser. It is seen that as the excitation increases, a sharp lasing peak occurs at 287 nm. The light input-light output (L-L) curve is shown in **Figure 6.2 (b)**, manifesting a lasing threshold around 530 kW cm^{-2}. The inset of **Figure 6.2 (b)** shows the L-L curve in a logarithmic scale. The two lines with a slope k=1 denote the spontaneous emission and lasing, respectively. An S-shape, which corresponds to the spontaneous emission, amplified spontaneous emission, and lasing, can be seen. The observation of the S-shape further confirms the lasing activity.[35, 36]

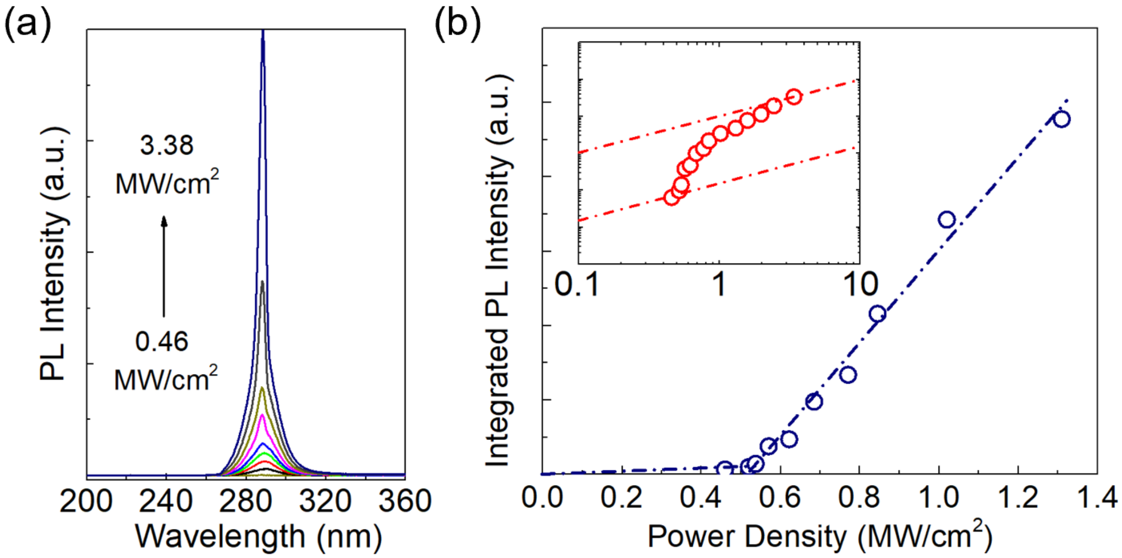

Figure 6.2. (a) The lasing spectra under different excitations. The spectra were measured at RT using edge geometry by a fourth harmonics 266 nm Nd: YAG laser. (b) The L-L curve. Inset: the L-L curve in a logarithmic scale.

Compared to our previously demonstrated AlGaN/AlN DH lasers at 298 nm,[27] the lasing threshold in this study is reduced significantly (950 kW cm^{-2} vs 530 kW cm^{-2}). The lasing threshold in this study is also comparable to the previously reported optically pumped AlGaN quantum well lasers on sapphire with similar lasing wavelengths.[12, 21-23]

To further investigate the reason of the threshold reduction, we have further compared the RT IQE of the structures grown in the present study and in the previous study.[27] IQE has been universally employed as an important material quality indicator of III-nitrides.[31, 37-40] To evaluate

RT IQE, we used a phenomenological ABC model [40] to analyze the power-dependent PL data excited by the 213 nm laser, through which the IQE can be calculated by,

$$IQE = \frac{I_{PL}}{\gamma G}, \tag{6.1}$$

where I_{PL} is the integrated PL intensity, γ is a fitting parameter, G is the generation rate. Experimentally, G can be determined via,

$$G = \frac{P_{laser}(1-R_F)\alpha}{A_{spot}h\nu}, \tag{6.2}$$

where P_{laser} is the peak pumping power under different excitations, R_F is the Fresnel reflection (18%), α is the absorption coefficient (2.35×10^5 cm^{-1}),[41] A_{spot} is the beam spot size (9.0×10^4 μm^2), and $h\nu$ is the photon energy of the 213 nm laser (5.82 eV). γ can be determined through fitting the following equation,

$$G = \frac{A}{\sqrt{B\gamma}}\sqrt{I_{PL}} + \frac{1}{\gamma}I_{PL} + \frac{C}{\sqrt{(B\gamma)^3}}\sqrt{I_{PL}^{\,3}}, \tag{6.3}$$

where A, B, and C are recombination coefficients.[40]

Figure 6.3 (a) shows the experimentally determined G as a function of I_{PL} in a logarithmic scale for both samples, together with the fitting curves using Equation (6.3). It is seen that excellent fittings are obtained, which allows us to determine γ and further allows us to determine the RT excitation-dependent IQE using Equation (6.1). **Figure 6.3 (b)** shows the calculated RT IQE as a function of the generation rate G in a semi-log scale for both samples. It is seen that at low excitations, e.g., $G = 7\times10^{26}$ cm^{-3} s^{-1}, the RT IQE of the sample grown in the present study is about 16% higher compared to the sample grown in the previous study.[27]

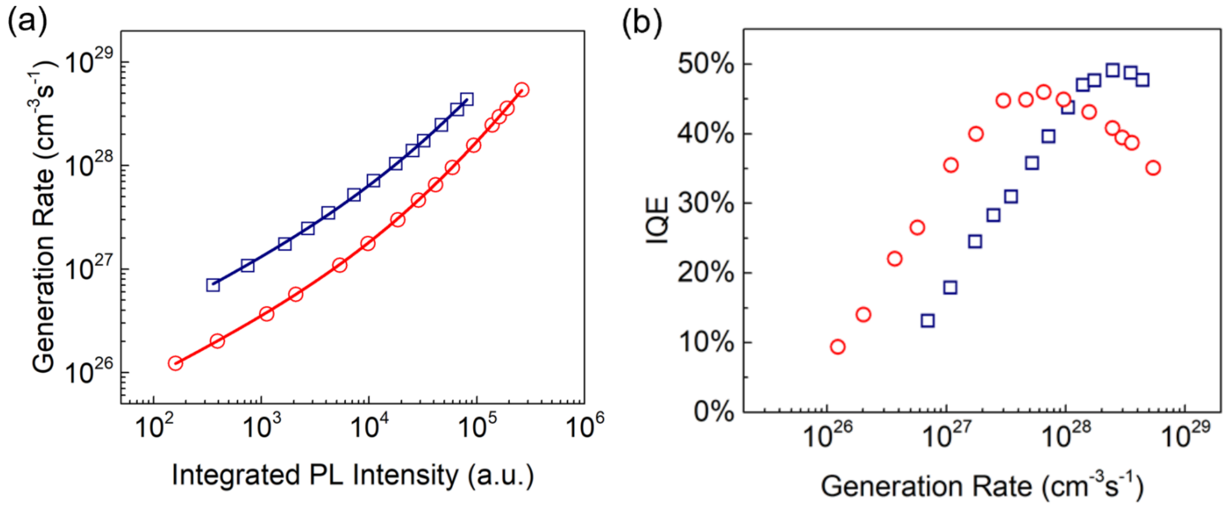

Figure 6.3. (a) Experimentally determined generation rate as a function of the integrated PL intensity. The samples were excited at RT by a 213 nm Q-switched DPSS laser. The solid lines are the fitting curves. (b) The calculated IQE as a function of the generation rate. Symbols: Circle denotes the sample grown in this work. Square denotes the sample grown in our previous study.[27]

Comparing the two AlGaN laser samples, similar cavities with similar geometries are used; optical images further indicate that the samples are optically smooth and thus similar propagation loss. Therefore, the reduced lasing threshold is likely related to the improved material quality, as reflected by the improved RT IQE at low excitations. In general, the low excitation IQE is closely related to both TDDs and point defects.[16, 31, 37-39] Therefore, the improved IQE indicates reduced TDDs or point defects, or both.

The role of point defects is identified first. In this regard, we have investigated the RT PL emission from deep levels by the 213 nm laser. As shown in **Figure 6.4 (a)**, for the sample grown in the previous study,[27] apart from the near band-edge emission at 4.20 eV, another broad emission band (peak around 2.53 eV) in the visible range (blue color) is measured in a wide range of excitation powers. Moreover, at low excitations, only the blue band emission is observed (a low excitation spectrum is shown in the inset of **Figure 6.4 (a)**). In contrast, no blue band emission is observed for the sample grown in the present study, as shown in **Figure 6.4 (b)**.

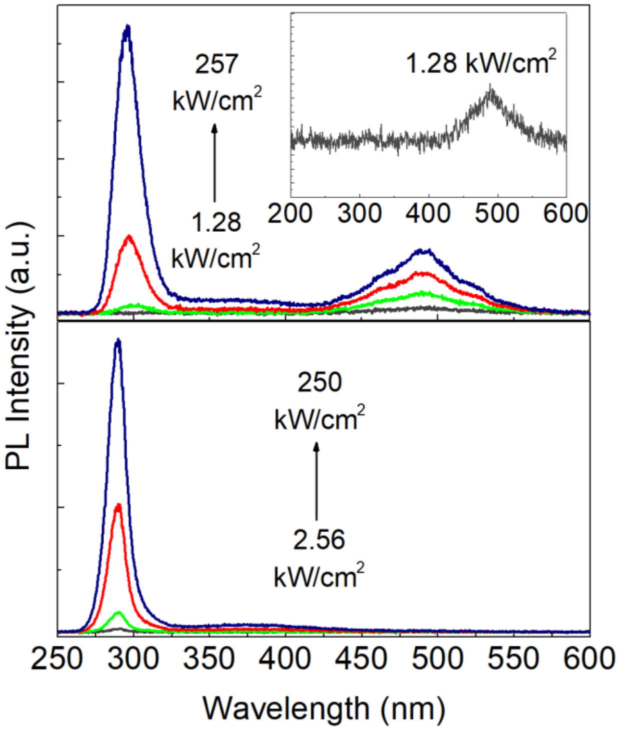

Figure 6.4. PL spectra detected by the UV-VIS spectrometer for both samples under different excitations by a 213 nm laser at RT. Upper panel: the sample grown in our previous study.[27] Lower panel: the sample grown in the present study. The inset of the upper panel shows the spectrum under a low excitation.

This blue band emission has been observed previously in AlGaN epilayers with a similar near band-edge emission energy, and is attributed to the donor-to-acceptor pair (DAP) transition involving Al vacancies and shallow donors, in specific, $(V_{Al}\text{-complex})^{2-}$.[33, 34] The absence of the blue bland emission in the sample grown in this study, therefore, is consistent with a significant suppression of unwanted impurity incorporation under high growth temperatures. Similar findings on the beneficial effects of high growth temperatures on the impurity corporation/point defects management of III-nitrides have also been reported from others, regardless of the samples grown by MBE or MOCVD.[42-45]

Regarding to the complex, it could be related to oxygen. The sources of oxygen could originate from the oxygen impurity in the nitrogen source gas, Al and Ga sources, as well as the nitrogen plasma source, as pointed out by the previous study.[42] In addition, it is noted that the large affinity of Al to oxygen further makes oxygen to be easily incorporated in AlGaN, compared to GaN.[42-43] Further pointed out by these previous studies, when the temperature is increased in the low-to-moderate range, the oxygen incorporation can be reduced in AlGaN epilayers grown by MBE in metal rich condition.[42,43] This is consistent with the absence of point defect related emission as the growth temperature increases shown in the present study. Nonetheless, using excess Ga at the growth front in metal rich condition as another mechanism to reduce oxygen incorporation should be noted as well.

We further examine the role of TDDs. For the lasing sample grown in the present study, if taking the bulk B value of 8.0×10^{-11} cm^3 s^{-1} from the recent study,[46] the A coefficient is derived to be 2.9×10^8 s^{-1}. Further following previous studies,[37, 39] and considering that the sample is nearly free of point defects, the TDD is estimated to be ~3×10^9 cm^{-2}. For the lasing sample grown in the previous study,[27] with the same B value, A is derived to be 5.8×10^8 s^{-1}. If further ignoring point defects, that is, assuming that this A value is only limited by TDD (and thus giving the upper limit of TDD), the TDD is ~6×10^9 cm^{-2}. However, from **Figure 6.4**, the observation of the blue band emission indicates the presence of point defects in the sample grown in the previous study.

This means that the TDD is less than 6×10^9 cm^{-2}. As such, the maximum TDD reduction introduced by increasing the substrate temperature comparing the two samples is around 50% or less. This could give a few percent improvement in IQE.[37, 39] Therefore, both TDD reduction and point defect control could contribute to the IQE improvement in this study. Nonetheless, it should be noted that, in general, MBE is a low-temperature growth technology compared to MOCVD, and thus the TDD reduction might not be dramatic due to the overall relatively low growth temperatures, in particular under metal rich growth regime.[39, 42]

Finally, it is noted that both samples show a similar PL linewidth that is much broader than the previously reported AlGaN epilayers wherein the compositional fluctuations are measured.[47] This indicates that, first, compositional fluctuations are present in both samples in discussion; and second, both samples could have a similar degree of carrier localization, and hence the role of carrier localization on the IQE improvement at low excitations could be excluded.

6.1.4. Conclusion

In this work, we have demonstrated AlGaN/AlN DH deep UV lasers on the AlN-on-sapphire substrate by MBE. The lasing wavelength is 287 nm, with a lasing threshold of 530 kW cm^{-2}, remarkably lower than our previous work.[27] This reduced lasing threshold is mainly attributed to the control of the defect formation, due to the elevated growth temperature of the active region. This is consistent with the increased low-excitation IQE. The drastic reduction of point defects is further clearly underpinned, indicated by the absence of defect PL bands in the visible range. Compared to the small improvement of the low-excitation IQE (16%), the reduction of lasing threshold is tremendous (reduced by several hundred kW cm^{-2}). This points out that the defects have a much more severe influence on the lasing threshold than on the IQE, as the defects not only quench the luminescence through nonradiative channels but also serve as the loss source for a laser cavity. Similar effect has been seen in the previous study.[16]

References

[1] M. Kneissl, J. Rass, *III-Nitride Ultraviolet Emitters*, Springer, Berlin, Germany **2016**.

[2] H. Amano, R. Collazo, C. D. Santi, S. Einfeldt, M. Funato, J. Glaab, S. Hagedorn, A. Hirano, H. Hirayama, R. Ishii, Y. Kashima, Y. Kawakami, R. Kirste, M. Kneissl, R. Martin, F. Mehnke, M. Meneghini, A. Ougazzaden, P. J. Parbrook, S. Rajan, P. Reddy, F. Römer, J. Ruschel, B. Sarkar, F. Scholz, L. J. Schowalter, P. Shields, Z. Sitar, L. Sulmoni, T. Wang, T. Wernicke, M. Weyers, B. Witzigmann, Y.-R. Wu, T. Wunderer, Y. Zhang, *J. Phys. D. Appl. Phys.* **2020**, *53*, 503001.

[3] T. D. Moustakas, *MRS Commun.* **2016**, *6*, 247.

[4] X. Wang, A. Yoshikawa, *Prog. Cryst. Growth Charact. Mater.* **2004**, 42, *48-49*.

[5] C.-H. Liao, H. Sun, X. Li , *in Nanoscale Semiconductor Lasers* (Eds: C. Tong, C. Jagadish), Elsevier, Amsterdam, Netherlands **2019**, Ch. 6.

[6] Q. Zhang, X. Yin, S. Zhao, *Phys. Status Solidi RRL* **2021**, 210090.

[7] K. B. Nam, M. L. Nakarmi, J. Li, J. Y. Lin, H. X. Jiang, *Appl. Phys. Lett.* **2003**, *83*, 878.

[8] R. M. N. T. Mattila, *Phys. Rev. B* **1996**, *54*, 23.

[9] N. N. M. L. Nakarmi, J. Y. Lin, and H. X. Jiang, *Appl. Phys. Lett.* **2009**, *94*, 091903.

[10] S. Zhao, Z. Mi, *Crystals* **2017**, *7*, 268.

[11] A. A. Allerman, M. H. Crawford, S. R. Lee, B. G. Clark, *J. Cryst. Growth* **2014**, *388,* 76.

[12] V. N. Jmerik, E. V. Lutsenko, S. V. Ivanov, *Phys. Status Solidi A* **2013**, *210*, 439.

[13] S. V. Ivanov, D. V. Nechaev, A. A. Sitnikova, V. V. Ratnikov, M. A. Yagovkina, N. V. Rzheutskii, E. V. Lutsenko, V. N. Jmerik, *Semicond. Sci. Technol.* **2014**, *29*, 084008.

[14] J. Jeschke, M. Martens, A. Knauer, V. Kueller, U. Zeimer, C. Netzel, C. Kuhn, F. Krueger, C. Reich, T. Wernicke, M. Kneissl, M. Weyers, *IEEE Photon. Technol. Lett.* **2015**, *27*, 1969.

[15] Q. Guo, R. Kirste, S. Mita, J. Tweedie, P. Reddy, B. Moody, Y. Guan, S. Washiyama, A. Klump, Z. Sitar, R. Collazo, *J. Appl. Phys.* **2019**, *126*, 223101.

[16] R. Kirste, Q. Guo, J. H. Dycus, A. Franke, S. Mita, B. Sarkar, P. Reddy, J. M. LeBeau, R. Collazo, Z. Sitar, *Appl. Phys. Express* **2018**, *11*, 082101.

[17] T. Wunderer, C. L. Chua, Z. Yang, J. E. Northrup, N. M. Johnson, G. A. Garrett, H. Shen, M. Wraback, *Appl. Phys. Express* **2011**, *4*, 092101.

[18] Z. Lochner, T.-T. Kao, Y.-S. Liu, X.-H. Li, M. Mahbub Satter, S.-C. Shen, P. Douglas Yoder, J.-H. Ryou, R. D. Dupuis, Y. Wei, H. Xie, A. Fischer, F. A. Ponce, *Appl. Phys. Lett.* **2013**, *102*, 101110.

[19] M. Martens, F. Mehnke, C. Kuhn, C. Reich, V. Kueller, A. Knauer, C. Netzel, C. Hartmann, J. Wollweber, J. Rass, T. Wernicke, M. Bickermann, M. Weyers, M. Kneissl, *IEEE Photon. Technol. Lett.* **2014**, *26*, 342.

[20] X.-H. Li, T. Detchprohm, T.-T. Kao, M. M. Satter, S.-C. Shen, P. Douglas Yoder, R. D. Dupuis, S. Wang, Y. O. Wei, H. Xie, A. M. Fischer, F. A. Ponce, T. Wernicke, C. Reich, M. Martens, M. Kneissl, *Appl. Phys. Lett.* **2014**, *105*, 141106.

[21] V. N. Jmerik, D. V. Nechaev, S. Rouvimov, V. V. Ratnikov, P. S. Kop'ev, M. V. Rzheutski, E. V. Lutsenko, G. P. Yablonskii, M. Aljohenii, A. Aljerwii, A. Alyamani, S. V. Ivanov, *J. Mater. Res.* **2015**, *30*, 2871.

[22] E. V. Lutsenko, N. V. Rzheutskii, V. N. Pavlovskii, G. P. Yablonskii, D. V. Nechaev, A. A. Sitnikova, V. V. Ratnikov, Y. V. Kuznetsova, V. N. Zhmerik, S. V. Ivanov, *Phys. Solid State* **2013**, *55*, 2173.

[23] J. Yan, Y. Tian, X. Chen, Y. Zhang, J. Wang, J. Li, *Phys. Status Solidi C* **2016**, *13*, 228.

[24] J. Mickevičius, J. Jurkevičius, K. Kazlauskas, A. Žukauskas, G. Tamulaitis, M. S. Shur, M. Shatalov, J. Yang, R. Gaska, *Appl. Phys. Lett.* **2012**, *101*, 041912.

[25] T. Takano, Y. Narita, A. Horiuchi, H. Kawanishi, *Appl. Phys. Lett.* **2004**, *84*, 3567.

[26] F. Asif, M. Lachab, A. Coleman, I. Ahmad, B. Zhang, V. Adivarahan, A. Khan, *J. Vac. Sci. Technol. B* **2014**, *32*, 061204.

[27] X. Yin, S. Zhao, *Phys. Status Solidi B* **2020**, *257*, 2000287.

[28] Z. Zhang, M. Kushimoto, T. Sakai, N. Sugiyama, L. J. Schowalter, C. Sasaoka, H. Amano, *Appl. Phys. Express* **2019**, *12*, 214003.

[29] H. Yoshida, Y. Yamashita, M. Kuwabara, H. Kan, *Appl. Phys. Lett.* **2008**, *93*, 241106.

[30] T. A. Henry, A. Armstrong, A. A. Allerman, M. H. Crawford, *Appl. Phys. Lett.* **2012**, *100*, 043509.

[31] Z. Bryan, I. Bryan, J. Xie, S. Mita, Z. Sitar, R. Collazo, *Appl. Phys. Lett.* **2015**, *106*, 142107.

[32] R. M. N. T. Mattila, *Phys. Rev. B* **1997**, *55*, 15.

[33] M. L. N. K. B. Nam, J. Y. Lin, and H. X. Jiang, *Appl. Phys. Lett.* **2005**, *86*, 222108.

[34] M. L. N. N. Nepal, J. Y. Lin, and H. X. Jiang, *Appl. Phys. Lett.* **2006**, *89*, 092107.

[35] S. Zhao, X. Liu, S. Y. Woo, J. Kang, G. A. Botton, Z. Mi, *Appl. Phys. Lett.* **2015**, *107*, 043101.

[36] S. Zhao, X. Liu, Y. Wu, Z. Mi, *Appl. Phys. Lett.* **2016**, *109*, 191106.

[37] K. Ban, J.-i. Yamamoto, K. Takeda, K. Ide, M. Iwaya, T. Takeuchi, S. Kamiyama, I. Akasaki, H. Amano, *Appl. Phys. Express* **2011**, *4*, 052101.

[38] Q. Dai, M. F. Schubert, M. H. Kim, J. K. Kim, E. F. Schubert, D. D. Koleske, M. H. Crawford, S. R. Lee, A. J. Fischer, G. Thaler, M. A. Banas, *Appl. Phys. Lett.* **2009**, *94*, 111109.

[39] H. Amano, *J. Phys. Conf. Ser.* **2011**, *326*, 012002.

[40] J. Lu, Y. Zhong, S. Zhao, *J. Vac. Sci. Technol. B* **2021**, *39*, 022803.

[41] J. F. Muth, J. D. Brown, M. A. L. Johnson, Z. Yu, R. M. Kolbas, J. W. Cook, J. F. Schetzina, *MRS Internet J. Nitride Semicond. Res.* **2014**, *4*, 502.

[42] C. R. Elsass, T. Mates, B. Heying, C. Poblenz, P. Fini, P. M. Petroff, S. P. DenBaars, J. S. Speck, *Appl. Phys. Lett.* **2000**, *77*, 3167.

[43] G. Koblmüller, R. M. Chu, A. Raman, U. K. Mishra, J. S. Speck, *J. Appl. Phys.* **2010**, *107*, 043527.

[44] J. Mickevičius, K. Nomeika, M. Dmukauskas, A. Kadys, S. Nargelas, R. Aleksiejūnas, *Vacuum* **2021**, *183*, 109871.

[45] S. F. Chichibu, T. Onuma, K. Hazu, A. Uedono, *Phys. Status Solidi C* **2013**, *10*, 501.

[46] M. E. Rudinsky, S. Y. Karpov, *Phys. Status Solidi A* **2019**, 217, 1900878.

[47] Ž. Podlipskas, R. Aleksiejūnas, A. Kadys, J. Mickevičius, J. Jurkevičius, G. Tamulaitis, M. Shur, M. Shatalov, J. Yang, R. Gaska, *J. Phys. D: Appl. Phys.* **2016**, *49*, 145110.

Chapter 7

Design and Simulation Towards Electrical Injected AlGaN UV Lasers

Even though the material quality of MBE-grown AlGaN on sapphire has been further improved by point defect control, leading to a low lasing threshold under optical pumping, the future achievement of feasible and highly efficient MBE-grown AlGaN LDs under electrical injection requires careful engineering related to charge carriers. Proper band engineering of the laser structure, especially the p-doped region, to mitigate asymmetric charge carrier distribution, resulted from the larger effective mass of holes than electrons, is of critical importance. Moreover, the Mg-induced optical loss from the UV absorbing p-region should be well controlled while optimizing the optical confinement of the active region.

In this Chapter, we design and simulate a unique AESL-EBL for enhancing hole injection via the assistance of hot holes. Mg-induced optical loss in such laser structure has been reduced to around 1 cm^{-1} by adjusting the layer thickness.

7.1 Manuscript

The following manuscript was published in *IEEE Journal of Quantum Electronics* (X. Yin and S. Zhao, "Improving Charge Carrier Transport Properties in AlGaN Deep Ultraviolet Light Emitters Using Al-Content Engineered Superlattice Electron Blocking Layer," *IEEE Journal of Quantum Electronics*, vol. 59, no. 1, pp. 1-6, 2023, doi: 10.1109/jqe.2023.3234991).

This manuscript studies the charge carrier transport properties of AlGaN deep UV LDs on sapphire with an insertion of the AESL-EBL.

Improving Charge Carrier Transport Properties in AlGaN Deep Ultraviolet Light Emitters using Al-Content Engineered Superlattice Electron Blocking Layer

*Xue Yin and Songrui Zhao**

Department of Electrical and Computer Engineering, McGill University, Montréal, QC H3A 0E9 Canada

Abstract: In this study, we investigate a unique Al-content engineered superlattice electron blocking layer (AESL-EBL) for improving the charge carrier transport properties of AlGaN quantum well (QW) deep ultraviolet (DUV) light-emitting diode (LED) structures. LED structures without EBL, with conventional bulk EBL (BEBL), and superlattice EBL (SL-EBL) are used for comparison. It is found that the LED structure with the AESL-EBL can exhibit superior electron blocking and hole injection, leading to reduced efficiency droop and improved light output power, compared to LED structures without EBL and with BEBL. Notably, the LED structure with AESL-EBL also outperforms the LED structure with SL-EBL, benefitting from the Al-content engineered SL. In the end, such an ASEL-EBL is applied to a DUV laser diode, and by optimizing the device structure low Mg-induced internal loss of around 1 cm^{-1} can be obtained.

Index Terms: AlGaN, electron blocking layer, superlattice, hole injection, hot hole, optical confinement.

7.1.1. Introduction

AlGaN-based deep ultraviolet (DUV) light-emitting devices, such as light-emitting diodes (LEDs) and lasers, have attracted considerable attention over the past two decades due to their widespread applications in disinfection, curing, optical communication, sensing, and so on [1]-[5]. They are emerging as high-efficient, environmental-friendly, and compact alternatives to conventional DUV technologies, such as low- and medium-pressure mercury lamps, as well as gas and solid-state lasers [1], [2]. Nevertheless, the efficiencies of the state-of-the-art AlGaN DUV LEDs have remained low, in particular for light emission wavelengths below the human exposure safe wavelength (e.g., 230-240 nm or shorter) [1], [3], [6]-[11]. Moreover, the shortest wavelength of electrically injected AlGaN quantum well (QW) lasers has been stuck at 336 nm [12] for a decade until the recently reported 271.8 nm laser in 2019 [13].

To achieve electrically injected AlGaN DUV light-emitting devices, improving carrier transport is of critical importance. Different from optical excitation wherein the excess carriers can be excited nearly simultaneously in the active region, for the electrically injected devices, charge carriers need to transport to the active region. Nonetheless, the transport of electrons and holes are highly asymmetric in high Al-content AlGaN alloys, which is one of the major roadblocks to high injection efficiency. This is fundamentally limited by the large hole effective mass of high Al-content AlGaN alloys (e.g., 2.7 m_0 for AlN [14]). Due to the large hole effective mass, the commonly used p-type dopant magnesium (Mg) has an activation energy of several hundred meV [14], [15], leading to an extremely low hole concentration p_0 at room temperature. Moreover, also because of the large effective mass, the room temperature hole mobility μ_p is also significantly lower than that of electrons. The low $p_0 \cdot \mu_p$ product makes the high injection regime easy to reach at low injection levels [16], [17], being a prominent cause of the electron leakage in AlGaN DUV

LEDs. The electron leakage significantly degrades the LED device performance. It also makes the development of AlGaN DUV lasers challenging. In general, due to the large effective mass of both holes and electrons in AlGaN alloys, the required carrier density for population inversion is on the order of 10^{19} cm^{-3}; the presence of electron leakage makes this high carrier density difficult to reach. This situation is drastically different from conventional III-V materials wherein the charge carrier transport is more symmetric [18], and highlights the necessity of improving the charge carrier transport properties for AlGaN-based optoelectronic device development.

In this context, the major approaches include incorporating electron blocking layers (EBLs) [19]-[25] and the implementation of tunnel junctions [26]-[30]. Whereas the tunnel junction utilizes tunneling to improve carrier injection, EBL engineers the energy band diagram substantially to minimize the electron leakage from the QW while maintaining the hole transport to the QW, i.e., reducing the potential barrier height for hole injection to the QW. In this regard, various EBLs such as bulk EBL (BEBL) with insertion layers [22], [31]-[33], graded EBL (GEBL) [20], [34]-[36], and superlattice EBL (SL-EBL) [24], [37]-[39] have been investigated. SL-EBL is among the most promising candidates for enhancing hole injection, due to its additional benefits such as doping effect that enhances acceptor activation [40], [41], and charge carrier transport mechanism via both thermionic emission process and tunneling. In recent years, researchers have also combined SL with GEBL, i.e., graded SL-EBL (GSL-EBL) [21], [23], to further improve hole injection.

Apart from achieving reduced hole potential barrier height, the other strategy to boost hole injection is to accelerate holes, taking the advantage of favorable electric polarization fields, through which holes could gain additional kinetic energies when travel across the p-region, i.e., “hot” holes are generated. For example, a hole accelerator, which consists of a 3-nm-thick p-

AlGaN inserted in a 200-nm-thick p-GaN, was proposed by Zhang et al. to promote hole transport in indium gallium nitride (InGaN)/GaN blue LEDs [42]. Chu et al. have also suggested the insertion of thin AlN layers between the last quantum barrier (LQB) and p-EBL to achieve hot holes in AlGaN-based DUV LEDs [32]. Moreover, the p-AlInGaN/AlGaN short-period SL-EBL has also been investigated for hot hole generation in order to improve hole transport in near-UV LEDs [39].

In this work, we introduce a unique Al-content engineered superlattice p-EBL (AESL-EBL) in AlGaN DUV-emitting QW LED structures. It is noted that, given the commonly observed compositional fluctuations in the epitaxial AlGaN alloys, such an Al-content engineered EBL could be much easier to obtain compared to regular SL-EBL (e.g., GSL-EBL) wherein a precise control on Al content is needed. Our study shows that the Al-content engineered SL-EBL enhances both electron blocking and hot hole generation, leading to significantly reduced efficiency droop and drastically improved light output power, compared to LED structures without EBL, with BEBL, and with SL-EBL. In the end, we have also evaluated the possibility of applying such an Al-content engineered SL-EBL to DUV laser diodes.

7.1.2. Structures and Parameters

Figure 7.1 shows the device structure, which consists of a 200-nm-thick n-AlN buffer layer, a 90-nm-thick n-$Al_{0.7}Ga_{0.3}N$ cladding layer, and three pairs of undoped $Al_{0.42}Ga_{0.58}N$ (3 nm)/$Al_{0.53}Ga_{0.47}N$ (9 nm) QWs, followed by a p-EBL, a 120-nm-thick p-$Al_{0.7}Ga_{0.3}N$ cladding layer with the insertion of 10-nm-thick p-$Al_{0.4}Ga_{0.6}N$ electron leakage test single QW, a 100-nm-thick p-$Al_{0.5}Ga_{0.5}N$ layer, and a 10-nm-thick p-GaN contact layer, on a 105-μm-thick AlN-on-sapphire template. The silicon (Si) and Mg doping in both types of layers were set to be

5×10^{19} cm^{-3}, except for the p-GaN contact layer which was 1×10^{20} cm^{-3}. The size of the device was 200 µm × 200 µm. The inset of **Figure 7.1** shows different p-EBL designs, with LED A: no EBL; LED B: p-$Al_{0.72}Ga_{0.28}N$ BEBL; LED C: 3-period $Al_{0.6}Ga_{0.4}N$ (2nm)/$Al_{0.8}Ga_{0.2}N$ (2nm) SL-EBL; LED D: AESL-EBL. In all p-EBLs, the thickness was 14 nm, with an average Al content of 0.72.

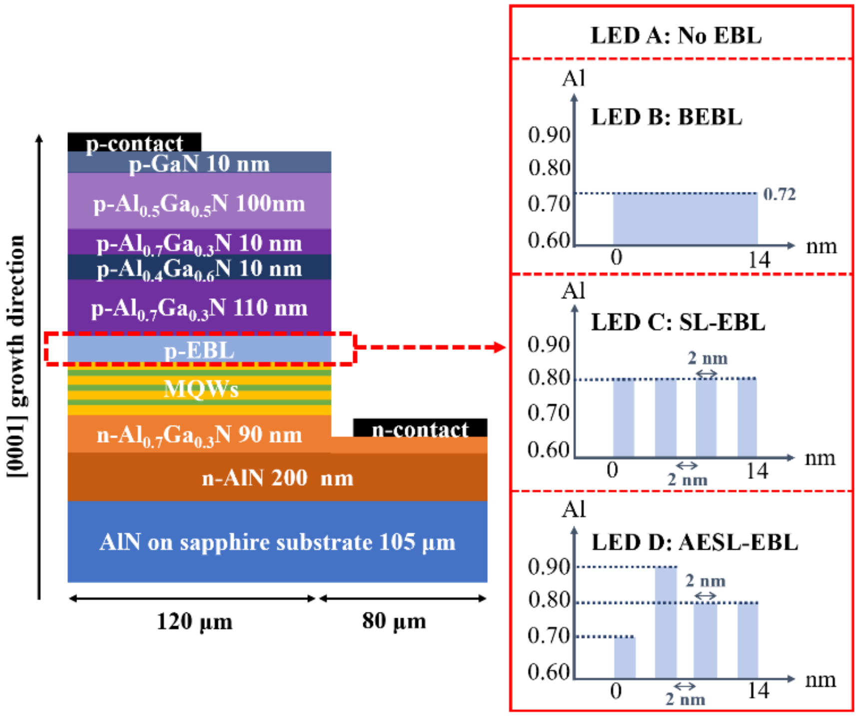

Figure 7.1. Schematic of AlGaN DUV LED structures studied in this work.

The electrical and optical properties of different designs were investigated via the Crosslight Advanced Physical Models of Semiconductor Devices (APSYS). The band-offset ratio between conduction band and valence band $\Delta E_c/\Delta E_v$ was 0.65/0.35 [43]. The energy bandgap of AlGaN alloys was estimated via, $E_g(Al_xGa_{1-x}N) = x\cdot E_g(AlN) + (1-x)\cdot E_g(GaN) - b\cdot x(1-x)$, where x is the Al content, $E_g(AlN)$ and $E_g(GaN)$ were assumed to be 6.25 eV and 3.510 eV, respectively, and the bowing parameter b was 0.7 [44]. Shockley-Read-Hall recombination, bimolecular radiative recombination, and Auger recombination coefficients were assumed to be 1×10^{8} /s, 2×10^{-11} cm^3/s, and 1×10^{-30} cm^6/s, respectively. The ionization energy of Si donor was 40 meV [1], [45], whereas the Mg acceptor ionization energy was linearly varied from 170 meV (for GaN) to 470 meV (for AlN) [14], [43]. Moreover, electron and hole mobilities were calculated by the Cauchy-Thomas approximation [46], [47],

$$\mu_i(N) = \mu_{min,i} + \frac{\mu_{max,i} - \mu_{min,i}}{1 + (\frac{N}{N_{ref,i}})^{a,i}}$$

where *i* represents electrons (holes), μ_{max}, μ_{min}, N_{ref}, a are the fitting parameters that depend on the semiconductor system, and *N* is the layer doping concentration. For electrons in AlGaN alloys, parameters μ_{max}, μ_{min}, N_{ref}, and a were assumed to be 306 cm^2/Vs , 132 cm^2/Vs , 1.0×10^{17} cm^{-3}, and 0.29, respectively [48], [49]. In terms of holes in AlGaN, the respective values were 2 cm^2/Vs, 2 cm^2/Vs, 3.0×10^{17} cm^{-3}, and 0.395 [48], [49]. In addition, the quantum tunneling model across p-EBL was employed in LED C and LED D [22]. The electric polarization fields were also considered. Given the compensation effects in epitaxial device structures, the polarization screening factor was set to 0.5. The internal loss and temperature were assumed to be 2000 m^{-1} and 300 K, respectively.

7.1.3. Results and Discussion

Figure 7.2 illustrates the energy band diagrams (solid lines) and quasi-Fermi levels (quasi-E_f, dash lines) for different LED structures under a forward injection current density of 200A/cm^2. $\emptyset_e$ ($\emptyset_h$) is the effective electron (hole) potential barrier height and is defined as the energy difference between the conduction (valence) band edge and quasi-E_f. It is seen that LED D with an AESL-EBL exhibits the highest electron potential barrier height of 377 meV, significantly higher compared to LED A (185 meV), LED B (233 meV), and LED C (283 meV), indicating less electron leakage and better confinement of electrons in the active region.

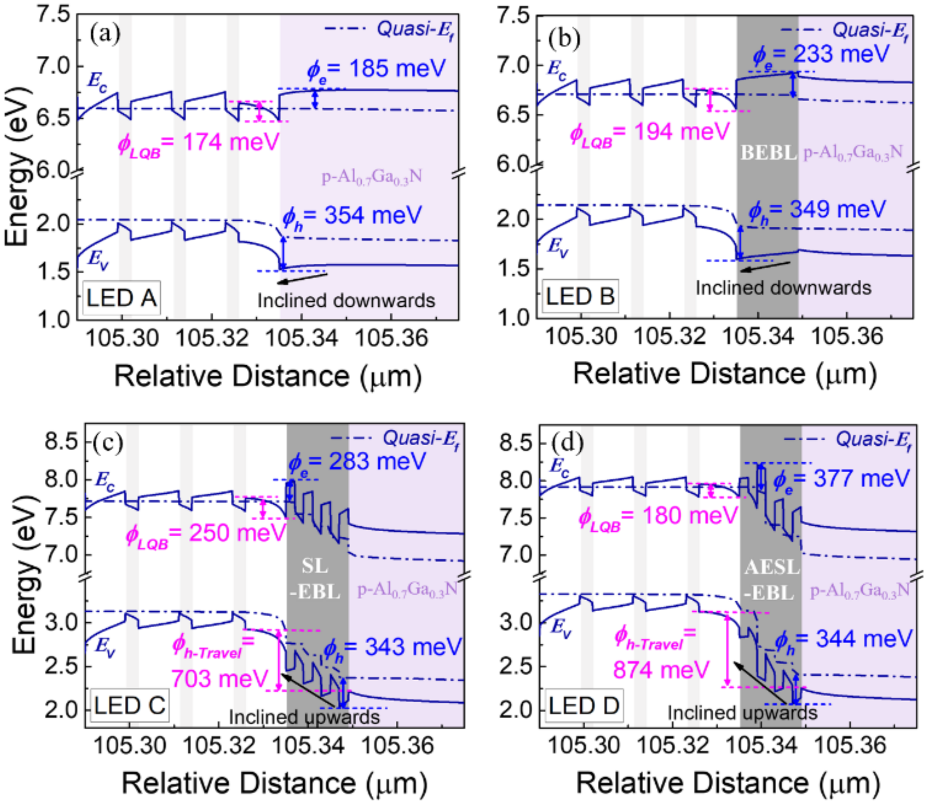

Figure 7.2. Energy band diagrams for (a) LED A, (b) LED B, (c) LED C, and (d) LED D at 200 A/cm². E_c, E_V, and quasi-E_f represent conduction band edge, valence band edge, and quasi-Fermi level, respectively. $\emptyset_e$ and $\emptyset_h$ denote the respective effective potential barrier heights for electrons and holes. $\emptyset_{LQB}$ denotes the bend bending at the LQB/p-region interface. $\emptyset_{h-Travel}$ represents the energy level difference between the p-EBL/p-$Al_{0.7}Ga_{0.3}N$ and LQW/LQB interfaces in the valence band. More details are described in the main text.

The large barrier height in LED D is first attributed to the high Al content in the second SL barrier (2-nm-thick p-$Al_{0.9}Ga_{0.1}N$) that noticeably increases the electron potential barrier height.

Second, the use of a relatively low Al content of 0.7 in the first SL barrier significantly reduces $\emptyset_{LQB}$, which represents the band bending at the LQB/p-region interface due to the polarization induced positive sheet charges. It is seen that $\emptyset_{LQB}$ of LED D (180 meV) is lower than that of LED B (194 meV) and LED C (250 meV), and comparable to that of LED A (174 meV). The slightly large $\emptyset_{LQB}$ in LED D compared to LED A is due to the electric polarization field induced by high Al-content SL barriers. As the band bending at the LQB/p-region interface leads to reduced electron potential barrier height, the reduction of the band bending thus helps to effectively lift the electron potential barrier height. Moreover, the reduction of the band bending at the LQB/p-region interface also reduces electron accumulation at the interface, further mitigating electron leakage from the active region.

The effective hole potential barrier heights are estimated to be 354 meV, 349 meV, 343 meV, and 344 meV for LED A, LED B, LED C, and LED D, respectively. This indicates a slightly enhanced hole transport in LEDs C and D, compared to LEDs A and B. In addition, LEDs C and D show an overall upwards inclination of valence bands (marked by arrows), different from the downwards inclination in LEDs A and B. Such an upwards inclination is a result of the strong electric polarization field in the SL, which is in the same direction of the applied electric field. As such, holes will gain additional kinetic energies from the electric polarization field when travel through the p-EBL, i.e., hot holes are generated [32], [42], enhancing their transport to the QW active region.

We have further estimated the kinetic energy that hot holes gained when travel across the p-EBL into the MQWs region in LED C and LED D. This kinetic energy is denoted as $\emptyset_{h-Travel}$, and can be estimated by the energy level difference between the p-EBL/p-$Al_{0.7}Ga_{0.3}N$ interface and the last quantum well (LQW)/LQB interface in the valence band [32]. It is seen that holes in

LED D gain a significantly higher kinetic energy of 874 meV compared to that of LED C (703 meV), attributed to the larger electric polarization field generated in the Al-content engineered SL, compared to that in regular SL. This suggests that holes in LED D are expected to be more kinetic compared to holes in LED C, making LED D potentially outperform LED C.

Here, it is worth mentioning that, although SL-EBL does not necessarily provide hot holes, by exploiting the large electric polarization field, hot holes can be generated. Moreover, further engineering the Al content in the SL can remarkably enhance such an effect.

The corresponding current densities for LED A and LEDs B to D as a function of the relative distance at a forward current density of 200 A/cm^2 are shown in **Figure 7.3 (a)** and **Figure 7.3 (b)**, respectively. The electron and hole current densities are represented by solid and dot lines, respectively. Remarkably reduced electron leakage and enhanced hole injection are clearly presented in LED D, compared to the rest three LED structures. Besides, the sharp decrease of the electron current density and the increase of the hole current density in the p-$Al_{0.4}Ga_{0.6}N$ test QW are only observed in LEDs A and B, suggesting excellent carrier confinement in the LED structures with SL-EBLs. More importantly, compared to LED C, LED D shows both promoted electron blocking and hole injection in the p-EBL and active region, due to the Al-content engineered SL as described earlier along with **Figure 7.2**.

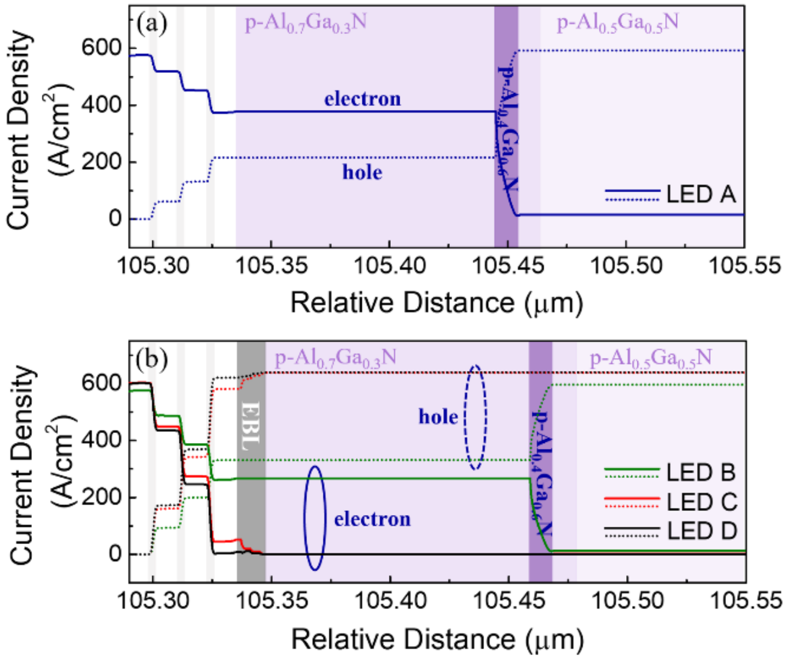

Figure 7.3. Current density as a function of the relative distance for (a) LED A and (b) LEDs B to D at 200 A/cm^2. The solid and dot lines represent the electron and hole current densities of the four LEDs, respectively.

We have further investigated the distribution of electron and hole concentrations of all LED structures at 200 A/cm^2. As shown in **Figure 7.4 (a)**, LED D (the structure with AESL-EBL) demonstrates the highest electron concentration in all QWs, surpassing all other LED structures. **Figure 7.4 (b)** illustrates the electron concentration accumulated at the LQB/p-region interface. It is seen that the electron accumulation at the LQB/p-region interface in LED D is reduced nearly by half, compared to that in LED C. This is mainly attributed to the alleviated band bending in LED D, due to the use of Al-content engineered SL as described earlier in **Figure 7.2**.

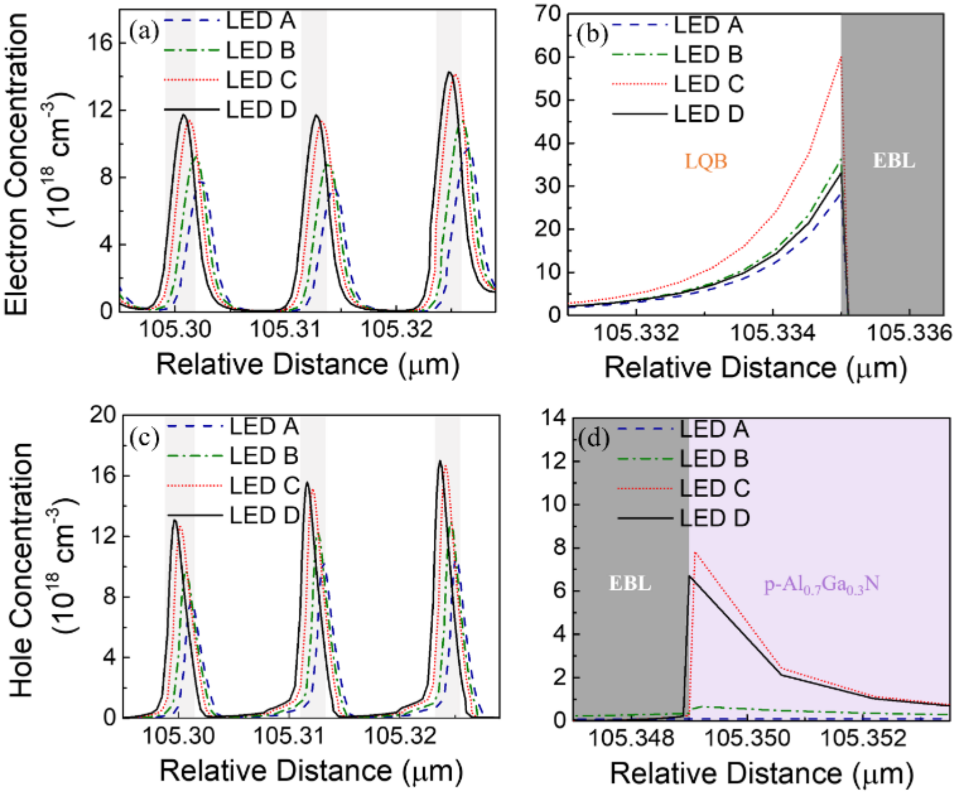

Figure 7.4. (a) Electron concentrations in the active region for the four LED structures. (b) Electron concentrations at the LQB/p-region interface. (c) Hole concentrations in the active region for the four LED structures. (d) Hole concentrations at the p-EBL/p-Al$_{0.7}$Ga$_{0.3}$N interface. The injection current density is 200 A/cm^2. Note that, in terms of LED A without EBL, the EBL label in Figure 7.4 (b) and Figure 7.4 (d) refers to the p-Al$_{0.7}$Ga$_{0.3}$N layer.

Similarly, LED D also demonstrates the highest hole concentrations in all QWs, surpassing all other LED structures, as shown in **Figure 7.4 (c)**. In addition, comparing LED D to LED C, less accumulation of holes at the p-EBL/p-Al$_{0.7}$Ga$_{0.3}$N interface is seen in LED D in **Figure 7.4 (d)**, again suggesting the improvement of hole transport using Al-content engineered SL than regular SL-EBL. Nonetheless, it is noted that LED structures with SL-EBLs do show more hole accumulation at the interface, due to band discontinuity and polarization induced negative sheet charges. In fact, identical phenomena are also observed for electrons at the LQB/p-region interface. However, given the significantly increased barrier heights for electron blocking and hot hole generation, devices with SL-EBLs still outperform devices without EBL and with BEBL.

The radiative recombination rate is further investigated for all LED structures as a function of the relative distance at a forward current density of 200 A/cm^2. The results of LED A and LEDs B to D are shown in **Figure 7.5 (a)** and **Figure 7.5 (b)**, respectively. It is seen that LED D exhibits the highest radiative recombination rate in all QWs, with more than a 2× enhancement compared to LED A. Moreover, compared to LED C, the parasitic emission in the EBL region is also drastically reduced in LED D, reflecting a superior electron blocking and hole injection improvement using the Al-content engineered SL. It is also noted that, due to the electron leakage, light emission from the test $Al_{0.4}Ga_{0.6}N$ QW is seen in both LED A and LED B; in contrast, LED C and LED D do not show any carrier recombination from such a test QW.

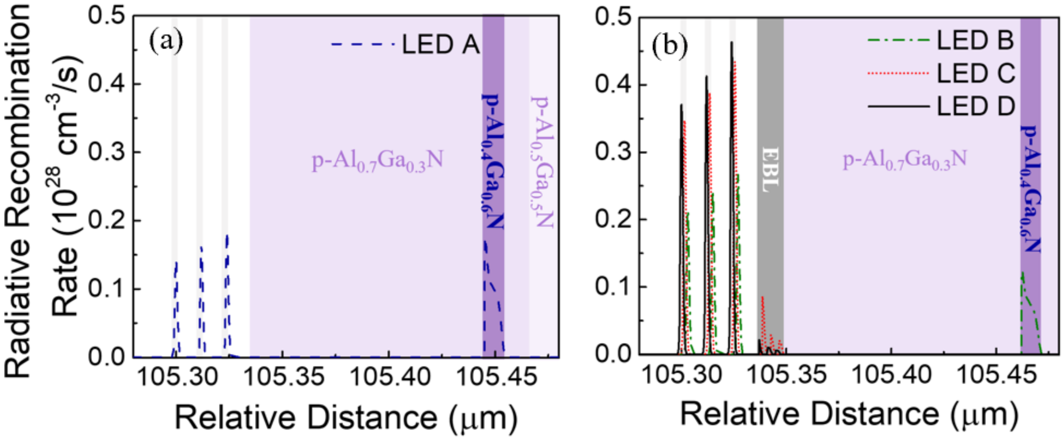

Figure 7.5. Radiative recombination rate as a function of the relative distance for (a) LED A and (b) LEDs B to D at 200 A/cm^2.

Figure 7.6 (a) shows the simulated electroluminescence (EL) intensity at a forward current density of 200 A/cm^2. It is seen that all the four LEDs show emission wavelengths at around 268 nm. Among these LEDs, LED D shows the highest peak intensity. **Figure 7.6 (b)** shows the calculated internal quantum efficiency (IQE) for the four LED structures. LED D shows the highest peak IQE of 52.5%. It is also seen that the efficiency droop decreases from 26% in LED A to 5.7% in LED D. The efficiency droop onset current density is also increased from 17 A/cm^2 in LED A to 49 A/cm^2 in LED D. Consequently, LED D exhibits the highest output power amongst all LED structures, with a near 3× enhancement compared to LED A at a forward current density of 200 A/cm^2, as shown in **Figure 7.6 (c)**.

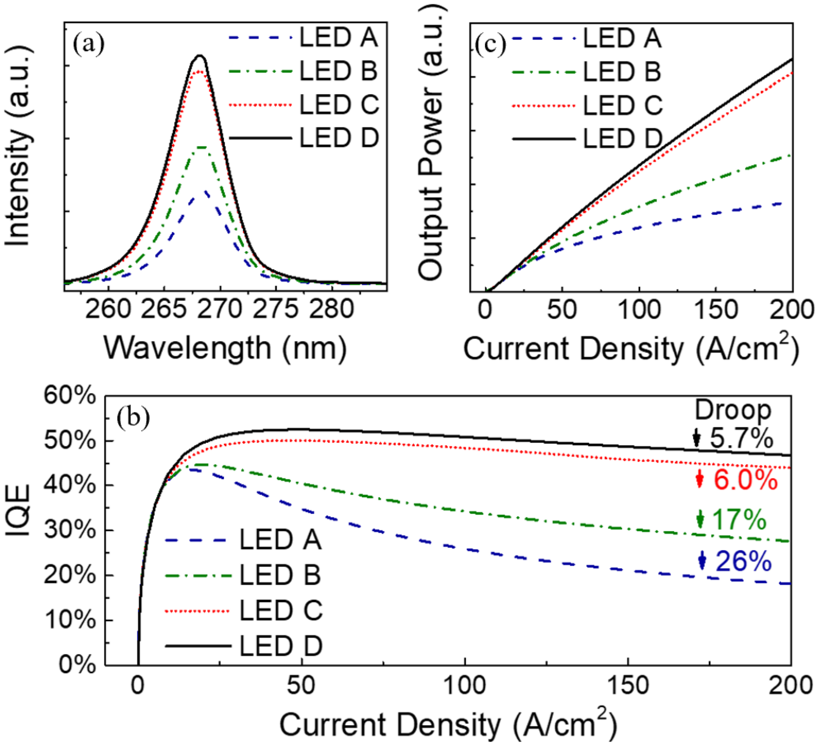

Figure 7.6. (a) Simulated EL spectra for four LED structures at 200 A/cm^2. (b) IQE and (c) output power as a function of current density for the four LED structures.

In the end, we evaluate the possibility of applying such AESL-EBL into DUV laser diodes, as high p-type doping in the EBL could cause a severe Mg-induced internal loss. In this case, we consider a laser diode structure based on LED D with varying cladding layer thicknesses, aiming to minimize the loss. The Mg-induced loss can be estimated via $\alpha = \alpha^{Mg} \times \Gamma$ [50], where α^{Mg} is the absorption coefficient and assumed to be 50 cm^{-1} [50] and 10^5 cm^{-1} [51] for AlGaN:Mg (for high Al content AlGaN alloys) and GaN:Mg, respectively. Γ is the optical confinement factor, which in this study was estimated by Crosslight Photonic Integrated Circuit Simulator in 3D (PICS3D) with parameters mentioned in section 2. With obtaining Γ, Mg-induced loss can be estimated.

The optimized structure is shown in the top panel of **Figure 7.7**, which consists of a 200-nm-thick n-AlN buffer layer, a 350-nm-thick n-$Al_{0.7}Ga_{0.3}N$ cladding layer, three pairs of intrinsic $Al_{0.42}Ga_{0.58}N$ (3 nm)/$Al_{0.53}Ga_{0.47}N$ (9 nm) QWs, sandwiched by two 50-nm-thick $Al_{0.53}Ga_{0.47}N$ waveguide layers, followed by a p-AESL-EBL, 220-nm-thick p-$Al_{0.7}Ga_{0.3}N$ and 100-nm-thick p-$Al_{0.5}Ga_{0.5}N$ layers, and a 10-nm-thick p-GaN cap layer, on a 105-µm-thick AlN-on-sapphire template. The bottom panel of **Figure 7.7** shows the refractive index of the structure as a function of the relative distance and the optical field distribution of the fundamental mode. The corresponding enlarged scale for the AESL-EBL region is shown in the inset. It is seen that the mode has been well-confined in the active region, with a sharp mode profile. A Γ of ~10.9% is obtained from three pairs of QWs, whereas Γ for p-AESL-EBL, p-$Al_{0.7}Ga_{0.3}N$, p-$Al_{0.5}Ga_{0.5}N$, and p-GaN regions are ~1.9%, 2.8%, 2.0×10^{-2} %, and 2.5×10^{-5} %, respectively. This gives a total Mg-induced loss in the p-region of around 2.4 cm^{-1}, with ~1 cm^{-1} contributed from the p-AESL-EBL region. Such an Mg-induced loss in the p-region is comparable to or lower than the previous report

[52]. It is further noted that Mg-δ-doping or modulation-doping can be potentially used to further reduce the Mg-induced loss while maintaining the conductivity [53], [54].

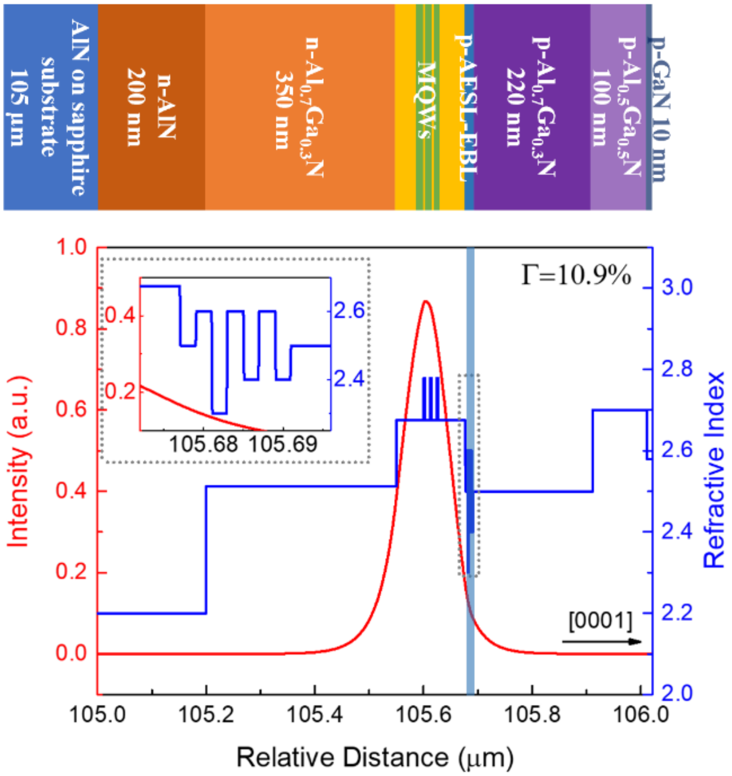

Figure 7.7. Top panel: The schematic of the AlGaN QW DUV laser structure with the Al-content engineered SL-EBL. Bottom panel: The corresponding optical field distribution and refractive index. The inset shows the EBL region.

7.1.4. Conclusion

In summary, a unique Al-content engineered SL-EBL has been numerically investigated, aiming to engineer charge carrier transport in AlGaN DUV light-emitting devices. It is found that such an EBL can significantly increase the electron potential barrier height compared to regular SL-EBL by nearly 100 meV, whereas the kinetic energy gain for hole transport can be improved by nearly 200 meV. Both the electron and hole accumulations at the respective LQB/p-region and p-EBL/p-$Al_{0.7}Ga_{0.3}N$ interfaces can also be alleviated, compared to using the regular SL-EBL. Consequently, the carrier injection into the QW active region is improved. The LED structure with the Al-content engineered SL-EBL exhibits superior performance compared to other LED structures in this study, including radiative recombination rates in the QW active regions, output power, internal quantum efficiency, and efficiency droop reduction. We have lastly examined Mg-induced internal loss in a laser structure using such a p-AESL-EBL, and it is found that by optimizing layer thickness low Mg-induced loss can be achieved.

References

[1] H. Amano *et al.*, “The 2020 UV emitter roadmap,” *J. Phys. D: Appl. Phys.,* vol. 53, no. 50, pp. 503001, 2020.

[2] C.-H. Liao, H. Sun, and X. Li, "Ultraviolet quantum well lasers," *Nanoscale Semiconductor Lasers,* Netherlands: Elsevier, 2019, Ch.6, pp. 139-163.

[3] H. Hirayama, "Recent progress in AlGaN deep-UV LEDs," *Light-Emitting Diode - An Outlook On the Empirical Features and Its Recent Technological Advancements*, United Kingdom: IntechOpen, 2018, Ch.7, pp. 127-158.

[4] S. M. N. Hasan, W. You, M. S. I. Sumon, and S. Arafin, “Recent progress of electrically pumped AlGaN diode lasers in the UV-B and -C bands,” *Photonics*, vol. 8, no. 7, pp.267, 2021.

[5] Q. Zhang, X. Yin, and S. Zhao, “Recent progress on aluminum gallium nitride deep ultraviolet lasers by molecular beam epitaxy,” *Phys. Status Solidi RRL*, vol. 15, no.7, pp. 2100090, 2021.

[6] H. Hirayama, Y. Tsukada, T. Maeda, and N. Kamata, “Marked enhancement in the efficiency of deep-ultraviolet AlGaN light-emitting diodes by using a multiquantum-barrier electron blocking layer,” *Appl. Phys. Express*, vol. 3, no. 3, pp. 031002, 2010.

[7] H. Hirayama, S. Fujikawa, N. Noguchi, J. Norimatsu, T. Takano, K. Tsubaki, and N. Kamata, “222-282 nm AlGaN and InAlGaN-based deep-UV LEDs fabricated on high-quality AlN on sapphire,” *Phys. Status Solidi A*, vol. 206, no. 6, pp. 1176-1182, 2009.

[8] D. Liu, S. J. Cho, J. Park, J. Gong, J.-H. Seo, R. Dalmau, D. Zhao, K. Kim, M. Kim, A. R. K. Kalapala, J. D. Albrecht, W. Zhou, B. Moody, and Z. Ma, “226 nm AlGaN/AlN UV

LEDs using p-type Si for hole injection and UV reflection," *Appl. Phys. Lett.*, vol. 113, no. 1, pp. 011111, 2018.

[9] C. G. Moe, S. Sugiyama, J. Kasai, J. R. Grandusky, and L. J. Schowalter, "AlGaN light-emitting diodes on AlN substrates emitting at 230 nm," *Phys. Status Solidi A*, vol. 215, no. 10, pp. 1700660, 2018.

[10] F. Mehnke, L. Sulmoni, M. Guttmann, T. Wernicke, and M. Kneissl, "Influence of light absorption on the performance characteristics of UV LEDs with emission between 239 and 217 nm," *Appl. Phys. Express,* vol. 12, no. 1, pp. 012008, 2019.

[11] A. Yoshikawa, R. Hasegawa, T. Morishita, K. Nagase, S. Yamada, J. Grandusky, J. Mann, A. Miller, and L. J. Schowalter, "Improve efficiency and long lifetime UVC LEDs with wavelengths between 230 and 237 nm," *Appl. Phys. Express*, vol. 13, no. 2, pp. 022001, 2020.

[12] H. Yoshida, Y. Yamashita, M. Kuwabara, and H. Kan, "Demonstration of an ultraviolet 336 nm AlGaN multiple-quantum-well laser diode," *Appl. Phys. Lett.,* vol. 93, no. 24, pp. 241106, 2008.

[13] Z. Zhang *et al.*, "A 271.8 nm deep-ultraviolet laser diode for room temperature operation," *Appl. Phys. Express,* vol. 12, no. 12, pp. 124003, 2019.

[14] K. B. Nam, M. L. Nakarmi, J. Li, J. Y. Lin, and H. X. Jiang, "Mg acceptor level in AlN probed by deep ultraviolet photoluminescence," *Appl. Phys. Lett.,* vol. 83, no. 5, pp. 878-880, 2003.

[15] V. P. John Simon, Chuanxin Lian, Huili Xing, Debdeep Jena, "Polarization-induced hole doping in wide–band-gap uniaxial semiconductor heterostructures," *Science*, vol. 327, no.5961, pp. 60-64, 2010.

[16] G.-B. Lin, D. Meyaard, J. Cho, E. Fred Schubert, H. Shim, and C. Sone, “Analytic model for the efficiency droop in semiconductors with asymmetric carrier-transport properties based on drift-induced reduction of injection efficiency,” *Appl. Phys. Lett.*, vol. 100, no. 16, pp. 161106, 2012.

[17] X. Hai, R. T. Rashid, S. M. Sadaf, Z. Mi, and S. Zhao, “Effect of low hole mobility on the efficiency droop of AlGaN nanowire deep ultraviolet light emitting diodes,” *Appl. Phys. Lett.*, vol. 114, no. 10, pp. 101104, 2019.

[18] J. H. Park, D. Y. Kim, E. F. Schubert, J. Cho, and J. K. Kim, “Fundamental limitations of wide-bandgap semiconductors for light-emitting diodes,” *ACS Energy Lett.*, vol. 3, no. 3, pp. 655-662, 2018.

[19] Z. Ren *et al.*, “Band engineering of III-nitride-based deep-ultraviolet light-emitting diodes: a review,” *J. Phys. D: Appl. Phys.*, vol. 53, no. 7, pp. 2001110, 2020.

[20] Z.-H. Zhang *et al.*, “Increasing the hole energy by grading the alloy composition of the p-type electron blocking layer for very high-performance deep ultraviolet light-emitting diodes,” *Photonics Res.*, vol. 7, no. 4, pp. B1-B6, 2019.

[21] B. So *et al.*, “Improved carrier injection of AlGaN-based deep ultraviolet light emitting diodes with graded superlattice electron blocking layers,” *RSC Adv.*, vol. 8, no. 62, pp. 35528-35533, 2018.

[22] Z.-H. Zhang *et al.*, “Hole transport manipulation to improve the hole injection for deep ultraviolet light-emitting diodes,” *ACS Photonics*, vol. 4, no. 7, pp. 1846-1850, 2017.

[23] Y.-H. Shih *et al.*, “Design of hole-blocking and electron-blocking layers in $Al_xGa_{1-x}N$-based UV light-emitting diodes,” *IEEE Trans. Electron Devices*, vol. 63, no. 3, pp. 1141-1147, 2016.

[24] H. Hirayama, Y. Tsukada, T. Maeda, and N. Kamata, “Marked enhancement in the efficiency of deep-ultraviolet AlGaN light-emitting diodes by using a multiquantum-barrier electron blocking layer,” *IEEE* Trans. Electron Devices, vol. 3, no. 3, pp. 031002, 2010.

[25] Z. Liu, H. Yu, Z. Ren, J. Dai, C. Chen, and H. Sun, “Polarization-engineered AlGaN last quantum barrier for efficient deep-ultraviolet light-emitting diodes,” *Semicond. Sci. Technol.*, vol. 35, no. 7, pp. 075021, 2020.

[26] Y. Zhang *et al.*, “ Demonstration of N-polar III-nitride tunnel junction LED,” *ACS Photonics*, vol. 7, no. 7, pp. 1723-1728, 2020.

[27] A. Pandey, J. Gim, R. Hovden, and Z. Mi, “An AlGaN tunnel junction light emitting diode operating at 255 nm,” *Appl. Phys. Lett.*, vol. 117, no. 24, pp. 241101, 2020.

[28] Y. Zhang *et al.*, “Tunnel-injected sub 290 nm ultra-violet light emitting diodes with 2.8% external quantum efficiency,” *Appl. Phys. Lett.*, vol. 112, no. 7, pp. 071107, 2018.

[29] R. Arefin *et al.*, “ Theoretical analysis of tunnel-injected sub-300 nm AlGaN laser diodes,” *IEEE J. Quantum Electron.*, vol. 56, no. 6, pp. 1-10, 2020.

[30] S. M. Sadaf *et al.*, “ An AlGaN core-Shell tunnel junction nanowire light-emitting diode operating in the ultraviolet-C band,” *Nano Lett.*, vol. 17, no. 2, pp. 1212-1218, 2017.

[31] L. Li, Y. Miyachi, M. Miyoshi, and T. Egawa, “Ultrathin inserted AlGaN/InAlN heterojunction for performance improvement in AlGaN-based deep ultraviolet light-emitting diodes,” *Appl. Phys. Express*, vol. 12, no. 1, pp. 011010, 2019.

[32] C. Chu *et al.*, “On the origin of enhanced hole injection for AlGaN-based deep ultraviolet light-emitting diodes with AlN insertion layer in p-electron blocking layer,” *Opt. Express*, vol. 27, no. 12, pp. A620-A628, 2019.

[33] C. Chu *et al.*, “On the $Al_xGa_{1-x}N/Al_yGa_{1-y}N/Al_xGa_{1-x}N$ (x>y) p-electron blocking layer to improve the hole injection for AlGaN based deep ultraviolet light-emitting diodes,” *Superlattices Microstruct.*, vol. 113, pp. 472-477, 2018.

[34] J.-Y. Chang, H.-T. Chang, Y.-H. Shih, F.-M. Chen, M.-F. Huang, and Y.-K. Kuo, “Efficient carrier confinement in deep-ultraviolet light-emitting diodes with composition-graded configuration,” *IEEE Trans. Electron Devices*, vol. 64, no. 12, pp. 4980-4984, 2017.

[35] X. Fan *et al.*, “Efficiency improvements in AlGaN-based deep ultraviolet light-emitting diodes using inverted-V-shaped graded Al composition electron blocking layer,” *Superlattices Microstruct.*, vol. 88, pp. 467-473, 2015.

[36] B. So, J. Kim, E. Shin, T. Kwak, T. Kim, and O. Nam, “Efficiency improvement of deep-ultraviolet light emitting diodes with gradient electron blocking layers ,” *Phys. Status Solidi A*, vol. 215, no. 10, pp. 1700677, 2018.

[37] Z. H. Zhang *et al.*, “ Nearly efficiency-droop-free AlGaN-based ultraviolet light-emitting diodes with a specifically designed superlattice p-type electron blocking layer for high Mg doping efficiency,” *Nanoscale Res. Lett.*, vol. 13, no. 1, pp. 122, 2018.

[38] P. Sun *et al.*, “Advantages of AlGaN-based deep ultraviolet light-emitting diodes with a superlattice electron blocking layer,” *Superlattices Microstruct.*, vol. 85, pp. 59-66, 2015.

[39] L. He *et al.*, “Efficient carrier transport for 368 nm ultraviolet LEDs with a p-AlInGaN/AlGaN short-period superlattice electron blocking layer,” *J. Mater. Chem. C*, vol. 9, no. 25, pp. 7893-7899, 2021.

[40] E. F. Schubert, W. Grieshaber, and I. D. Goepfert, “Enhancement of deep acceptor activation in semiconductors by superlattice doping,” *Appl. Phys. Lett.*, vol. 69, no. 24, pp. 3737-3739, 1996.

[41] P. Kozodoy, M. Hansen, S. P. DenBaars, and U. K. Mishra, “Enhanced Mg doping efficiency in $Al_{0.2}Ga_{0.8}N$/GaN superlattices,” *Appl. Phys. Lett.*, vol. 74, no. 24, pp. 3681-3683, 1999.

[42] Z.-H. Zhang *et al.*, “A hole accelerator for InGaN/GaN light-emitting diodes,” *Appl. Phys. Lett.*, vol. 105, no. 15, pp. 153503, 2014.

[43] J. Piprek, and Z. M. Simon Li, “Sensitivity analysis of electron leakage in III-nitride light-emitting diodes,” *Appl. Phys. Lett.*, vol. 102, no. 13, pp. 131103, 2013.

[44] I. Vurgaftman, and J. R. Meyer, “Band parameters for nitrogen-containing semiconductors,” *J. Appl. Phys.*, vol. 94, no. 6, pp. 3675-3696, 2003.

[45] R. Collazo *et al.*, “Progress on n-type doping of AlGaN alloys on AlN single crystal substrates for UV optoelectronic applications,” *Phys. Status Solidi C*, vol. 8, no. 7-8, pp. 2031-2033, 2011.

[46] D. M. Caughey, R. E. Thomas, “Carrier mobilities in silicon empirically related to doping and field,” *Proc. IEEE*, vol. 55, no. 12, pp. 2192-2193, 1967.

[47] T. T. Mnatsakanov, M. E. Levinshtein, L.I. Pomortseva, S. N. Yurkov, G. S. Simin, M. A. Khan, “Carrier mobility model for GaN,” *Solid State Electron.*, vol. 47, no.1, pp. 111–115, 2003.

[48] R. K. Mondal, V. Chatterjee, and S. Pal, “Efficient carrier transport for AlGaN-based deep-UV LEDs with graded superlattice p-AlGaN ,” *IEEE Trans. Electron Devices*, vol. 67, no. 4, pp. 1674-1679, 2020.

[49] T.-H. Wang, and J.-L. Xu, “Advantage of InGaN-based light-emitting diodes with trapezoidal electron blocking layer,” *Mater. Sci. Semicond. Process.*, vol. 29, pp. 95-101, 2015.

[50] M. Martens *et al.*, “The effects of magnesium doping on the modal loss in AlGaN-based deep UV lasers,” *Appl. Phys. Lett.*, vol. 110, no. 8, pp. 081103, 2017.

[51] C. S. M. Kuramoto, N. Futagawa, M. Nido, and A. A. Yamaguchi, “Reduction of internal loss and threshold current in a laser diode with a ridge by selective re-growth (RiS-LD),” *Phys. Status Solidi A*, vol. 2, no. 192, pp. 329–334, 2002.

[52] R. Arefin, W. You, S. H. Ramachandra, S. M. N. Hasan, H. Jung, M. Awwad, and S. Arafin, “Theoretical analysis of tunnel-injected sub-300 nm AlGaN laser diodes,” *IEEE J. Quantum Electron.*, vol. 56, no. 6, pp. 1-10, 2020.

[53] K. H. K. M. L. Nakarmi, J. Li, J. Y. Lin, and H. X. Jiang, “Enhanced p-type conduction in GaN and AlGaN by Mg-δ-doping,” *Appl. Phys. Lett.*, vol. 82, no. 18, pp. 3041, 2003.

[54] K. Mehta *et al.*, “Lateral current spreading in III-N ultraviolet vertical-cavity surface-emitting lasers using modulation-doped short period superlattices,” *IEEE J. Quantum Electron.*, vol. 54, no. 4, pp. 1-7, 2018.

7.2 Further Discussions on Device Simulation

Here, some details of the Crosslight simulation in the previous section are further described. First, the current density, plotted in the y-axis of **Figure 7.3**, is the local current density spreading in the simulated devices regarding different distances. All the figures in Chapter 7 are generated at a current density of 200 A/cm^2, which is the average current density on the electrode. Such average current density is the total current density divided by the defined contact size. Therefore, the local current density shown in the y-axis of **Figure 7.3** would be somewhere below or above the average current density of 200 A/cm^2. Details of the current density calculations can be found in Chapter 5 of the Crosslight software general manual [202]. Moreover, the simulated IQE in **Figure 7.6 (b)** differs from the radiative IQE mentioned in the other Chapters. Such simulated IQE considers both injection efficiency and radiative IQE via the SRH model. The recombination coefficients A, B, and C were assumed to be 1×10^{8} s^{-1}, 2×10^{-11} cm^3 s^{-1}, and 1×10^{-30} cm^6 s^{-1}, respectively, in the SRH model [97, 110]. In addition, the post-processing command "layer_conf" in Crosslight Software was used to calculate the optical confinement factor in **Figure 7.7**. In the end, it is also noted that the original material library from Crosslight Software is based on devices grown on GaN buffer layer and the base lattice will be that of GaN. Here, we changed the base buffer layer and base lattice to AlN in our case.

Chapter 8

Conclusion and Future Work

8.1 Conclusion

In this dissertation, we have investigated the molecular beam epitaxy of AlGaN epilayers for the development of semiconductor UV lasers on low-cost sapphire and Si substrates. Moreover, a novel design is proposed aiming to improve the charge carrier transport for electrically injected devices.

In specific, we have demonstrated a new approach to grow AlN epilayers on Si, which leads to high quality AlGaN epilayers on Si by using such AlN epilayers as buffer layers. The IQE obtained from the bulk AlGaN epilayers is significantly improved compared to the counterparts on sapphire and/or AlN-on-sapphire substrates. In parallel, we have further demonstrated optically pumped lasing from the MBE-grown AlGaN/AlN DH on the AlN-on-sapphire substrate, with a lasing threshold of 950 kW/cm^2. Further reduced lasing threshold is obtained by controlling the point defects, and lasing at 287 nm, with a threshold of 530 kW/cm^2, is measured. The research in this dissertation also represents the first MBE-grown laser structure that shows clear lasing evidence. Towards the electrically injected devices, we have proposed a unique AESL-EBL design, which can significantly enhance the electron blocking ability without compromising hole injection, assisted by the hot hole effect. By further optimizing the layer thickness, low Mg-doping induced optical loss can be obtained. Compared to the regular SL-EBL designs, wherein a precise control of the Al content is needed, this design could be more practical due to the relaxation of the Al content control.

8.2 Future Work

8.2.1 Optical Confinement Optimization

In Chapters 3 and 4, we have developed a new AlN buffer layer technology on Si and successfully demonstrated high quality AlGaN epilayers on top with various Al compositions. However, to achieve UV lasing on Si, optical confinement needs to be carefully optimized, as the bottom GaN nanowires and Si substrate could result in severe absorption of UV photons.

Taking AlGaN/AlN DH laser structures on the AlN template on Si as an example, one route is to adjust the layer thickness of the AlGaN active region. The optical field confinement of such structures could be improved in the active region if the active region thickness is optimized. A separate route is to engineer the thickness of the GaN nanowire and AlN buffer layer to achieve similar results; however, this would require additional work on the optimization of the AlN template growth condition.

An alternative approach to overcome the UV photons absorption from the bottom GaN nanowires and Si substrate is through substrate removal and transfer technology and/or etching. For instance, Si substrate can be mechanically lapped and then removed via reactive ion etching (RIE) in SF_6 plasma [203], which has a high selectivity between Si and AlGaN alloys. This could be followed by transferring the laser structure to a carrier wafer and KOH etching of the GaN nanowires. Careful calibration is required to minimize potential defects resulted in such a fabrication process.

It is noted that, to date, the AlGaN-based UV laser is still under development. Although it is ideal to eventually design the laser structure to achieve single transverse mode lasing, AlGaN-based UV laser has not reached that level yet. The design focus of the optical confinement optimization is mainly based on the conventional ridge-waveguide geometry in this dissertation.

8.2.2 Multiple Distributed Polarization Doping Segments

Following our progress on the optically pumped AlGaN/AlN DH lasers on sapphire in Chapters 5 and 6, the implementation of the DPD method in p-region could be a promising route towards electrical injection with enhanced hole injection efficiency and conductivity.

In this regard, we propose an electrical injected AlGaN UV laser structure with multiple DPD segments, as shown in **Figure 8.1 (a)**. Different from the conventional DPD methods [18, 124, 156-158], such multiple DPD segments offer additional advantages besides hole injection improvement: (1) Enhanced optical field confinement in the active region could be achieved via the use of 1st and 2nd DPD segments with relatively high Al contents, leading to a narrower field profile. (2) Better control on the optical loss with overall reduced DPD thickness compared to the conventional DPD structures (e.g., ~350 nm) [18, 132, 157] and, particularly, less mode leakage into the UV absorbing layers. The corresponding field distribution of the AlGaN deep UV laser structure is demonstrated in **Figure 8.1 (b)**. By engineering the layer thickness and Al contents of three different DPD segments, an optimized optical field confinement factor of ~12.2% could be obtained from a single QW active region, together with a minimized mode leakage ($\sim 1.8\times10^{-5}$ %) into the UV absorbing 3rd DPD segment and p-GaN regions.

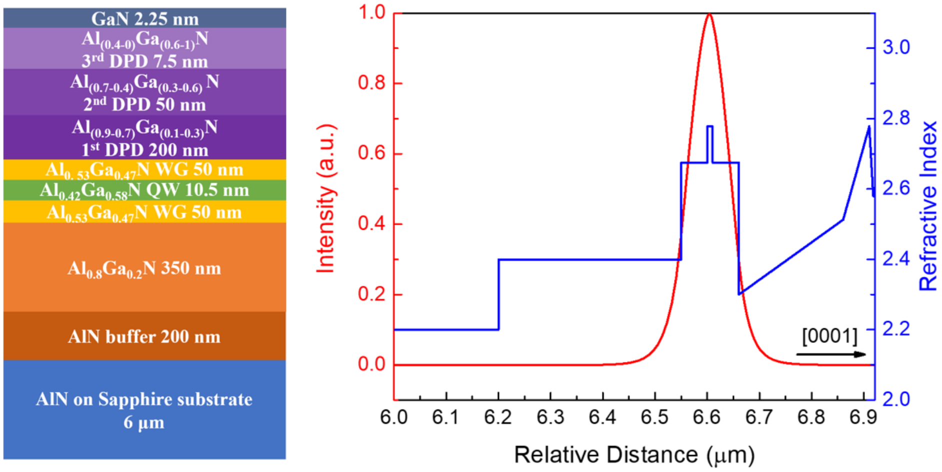

(a) (b)

Figure 8.1. (a) Schematic of the AlGaN deep UV laser structure with multiple DPD segments and (b) the corresponding optical field distribution and refractive index as a function of the relative distance.

8.2.3 Polarization Engineered Tunnel Junctions

Besides multiple DPD segments, introducing polarization engineered TJs [178] could be a separate route towards electrically injected AlGaN UV LDs. To date, (In)GaN is widely investigated as the intermediate tunneling layer (ITL) for AlGaN-based TJs [163, 165, 166, 168, 178]. However, the high absorption coefficients of such an ITL can lead to a significant optical loss [168]. To address this issue, AlGaN ITL could be a potential candidate. However, TJs with AlGaN ITL are rarely studied and a large depletion width of around 10 nm was reported when using AlGaN as the ITL [164], limiting the tunneling efficiency.

In future work, we propose AlGaN QWs as the ITL for the polarization engineered AlGaN-based TJs, with a combination of the DPD method on both sides of the junctions. The schematic and energy band diagram of such a structure is shown in **Figure 8.2**. First, due to the insertion of

$Al_xGa_{1-x}N/Al_yGa_{1-y}N$ QWs with low (e.g., $x < 0.5$) and high (e.g., $y > 0.5$) Al contents to replace conventional (In)GaN ITL, considerable optical loss reduction could be expected. Secondly, such AlGaN QWs also create strong polarization-induced surface charges at the $Al_xGa_{1-x}N/Al_yGa_{1-y}N$ interface, beneficial to the band tilting of the ITL region and tunnel distance reduction. The corresponding positive and negative surface charges are represented by the "+" and "-" signs, respectively, in **Figure 8.2**. Thirdly, the utilization of the DPD method on both sides of the TJs by grading the AlGaN layers could lead to a significant reduction of the space charge region, due to the generation of 3D hole/electron gas that pushes the Fermi level closer to valence/conduction band edge. It is also worth noting that, compared to MOCVD, MBE is more suitable for growing high quality TJs, due to its ability to favor p-type dopant incorporation as well as to achieve sharp doping profiles and interfaces, as mentioned in Section 1.3 [178].

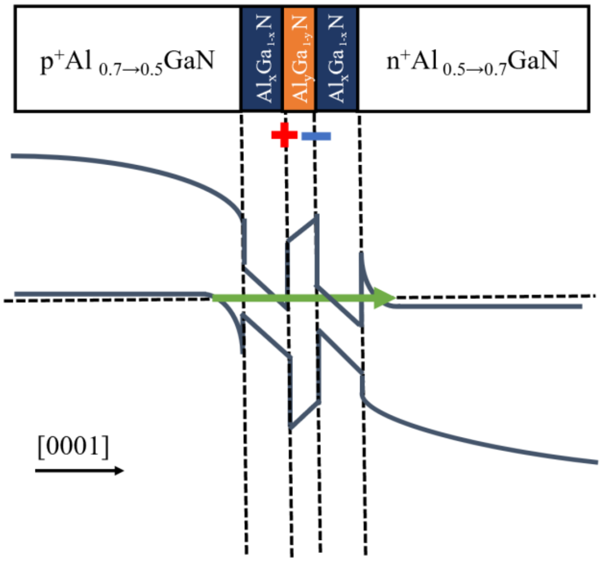

Figure 8.2. Schematic and the energy band diagram of the polarization engineered TJ with AlGaN QWs as the ITL at equilibrium. Growth direction is also labeled. Here, $x < 0.5$ and $y > 0.5$.

References

[1] T. Wernicke, L. Sulmoni, C. Kuhn, G. Tränkle, M. Weyers, and M. Kneissl, "Group III-Nitride-Based UV Laser Diodes," in *Semiconductor Nanophotonics*, (Springer Series in Solid-State Sciences, 2020, ch. Chapter 13, pp. 505-548.

[2] H. Amano *et al.*, "The 2020 UV Emitter Roadmap," *J. Phys. D: Appl. Phys.,* vol. 53, no. 50, pp. 503001, 2020, doi: 10.1088/1361-6463/aba64c.

[3] M. Kneissl, "III-Nitride Ultraviolet Emitters," *Springer Series in Materials Science,* vol. 227, 2016.

[4] Y. Muramoto, M. Kimura, and S. Nouda, "Development and Future of Ultraviolet Light-Emitting Diodes: UV-LED will Replace the UV Lamp," *Semicond. Sci. Technol.,* vol. 29, no. 8, 2014, doi: 10.1088/0268-1242/29/8/084004.

[5] D. Li, K. Jiang, X. Sun, and C. Guo, "AlGaN Photonics: Recent Advances in Materials and Ultraviolet Devices," *Adv. Opt. Photonics,* vol. 10, no. 1, 2018, doi: 10.1364/aop.10.000043.

[6] S. Zhao, H. P. T. Nguyen, M. G. Kibria, and Z. Mi, "III-Nitride Nanowire Optoelectronics," *Prog. Quantum. Electron.,* vol. 44, pp. 14-68, 2015, doi: 10.1016/j.pquantelec.2015.11.001.

[7] S. Zhao, J. Lu, X. Hai, and X. Yin, "AlGaN Nanowires for Ultraviolet Light-Emitting: Recent Progress, Challenges, and Prospects," *Micromachines (Basel),* vol. 11, no. 2, pp. 125, Jan 23 2020, doi: 10.3390/mi11020125.

[8] Q. Zhang, X. Yin, and S. Zhao, "Recent Progress on Aluminum Gallium Nitride Deep Ultraviolet Lasers by Molecular Beam Epitaxy," *physica status solidi (RRL) – Rapid Research Letters,* vol.15, no.7, pp.2100090, 2021, doi: 10.1002/pssr.202100090.

[9] R. Kirste, B. Sarkar, P. Reddy, Q. Guo, R. Collazo, and Z. Sitar, "Status of the Growth and Fabrication of AlGaN-based UV Laser Diodes for Near and Mid-UV Wavelength," *J. Mater. Res.*, vol. 36, no. 23, pp. 4638-4664, 2021, doi: 10.1557/s43578-021-00443-8.

[10] S. M. N. Hasan, W. You, M. S. I. Sumon, and S. Arafin, "Recent Progress of Electrically Pumped AlGaN Diode Lasers in the UV-B and -C Bands," *Photonics,* vol. 8, no. 7, 2021, doi: 10.3390/photonics8070267.

[11] S. Masui, Y. Matsuyama, T. Yanamoto, T. Kozaki, S.-i. Nagahama, and T. Mukai, "365 nm Ultraviolet Laser Diodes Composed of Quaternary AlInGaN Alloy," *Jpn. J. Appl. Phys.*, vol. 42, no. Part 2, No. 11A, pp. L1318-L1320, 2003, doi: 10.1143/jjap.42.L1318.

[12] D. W. T. Michael Kneissl, Mark Teepe, et al., "Ultraviolet AlGaN Multiple-Quantum-Well Laser Diodes," *Appl. Phys. Lett.*, no. 82, pp. 4441, 2003, doi: 10.1063/1.1585135.

[13] K. Iida *et al.*, "350.9 nm UV Laser Diode Grown on Low-Dislocation-Density AlGaN," *Jpn. J. Appl. Phys.*, vol. 43, no. No. 4A, pp. L499-L500, 2004, doi: 10.1143/jjap.43.L499.

[14] Z. Y. Michael Kneissl, Mark Teepe, et al., "Ultraviolet Semiconductor Laser Diodes on Bulk AlN," *J. Appl. Phys.*, no. 101, pp. 123103 2007, doi: 10.1063/1.2747546.

[15] H. Yoshida, Y. Yamashita, M. Kuwabara, and H. Kan, "A 342-nm Wltraviolet AlGaN Multiple-Quantum-Well Laser Diode," *Nat. Photonics,* vol. 2, no. 9, pp. 551-554, 2008, doi: 10.1038/nphoton.2008.135.

[16] H. Yoshida, Y. Yamashita, M. Kuwabara, and H. Kan, "Demonstration of an Ultraviolet 336 nm AlGaN Multiple-Quantum-Well Laser Diode," *Appl. Phys. Lett.*, vol. 93, no. 24, 2008, doi: 10.1063/1.3050539.

[17] Y. Aoki, M. Kuwabara, Y. Yamashita, Y. Takagi, A. Sugiyama, and H. Yoshida, "A 350-nm-Band GaN/AlGaN Multiple-Quantum-Well Laser Diode on Bulk GaN," *Appl. Phys. Lett.*, vol. 107, no. 15, 2015, doi: 10.1063/1.4933257.

[18] Z. Zhang *et al.*, "A 271.8 nm Deep-Ultraviolet Laser Diode for Room Temperature Operation," *Appl. Phys. Express*, vol. 12, no. 12, 2019, doi: 10.7567/1882-0786/ab50e0.

[19] M. Kneissl, "III-Nitride Ultraviolet Emitters," *Springer, Berlin, Germany*, 2016.

[20] I. Vurgaftman and J. R. Meyer, "Band Parameters for Nitrogen-Containing Semiconductors," *J. Appl. Phys.*, vol. 94, no. 6, pp. 3675-3696, 2003, doi: 10.1063/1.1600519.

[21] J. Li, J Wang, X. Yi, Z. Liu, T. Wei, J. Yan, B. Xue, "III-Nitrides Light Emitting Diodes: Technology and Applications," *Science Press*, 2020.

[22] O. Ambacher *et al.*, "Two Dimensional Electron Gases Induced by Spontaneous and Piezoelectric Polarization in Undoped and Doped AlGaN/GaN Heterostructures," *J. Appl. Phys.*, vol. 87, no. 1, pp. 334-344, 2000, doi: 10.1063/1.371866.

[23] V. Fiorentini, F. Bernardini, and O. Ambacher, "Evidence for Nonlinear Macroscopic Polarization in III–V Nitride Alloy Heterostructures," *Appl. Phys. Lett.*, vol. 80, no. 7, pp. 1204-1206, 2002, doi: 10.1063/1.1448668.

[24] V. F. Fabio Bernardini, "Spontaneous Polarization and Piezoelectric Constants of III-V Nitrides," *Phys. Rev. B.*, vol. 56, no. 16, pp. R10 024-R10 027, 1997.

[25] J. M. O Ambacher, C Miskys, A Link, M Hermann, M Eickhoff, M Stutzmann, F Bernardini, V Fiorentini, V Tilak, B Schaff and L F Eastman, "Pyroelectric Properties of Al(In)GaN/GaN Heteroand Quantum Well Structures," *J. Phys.: Condens. Matter*, vol. 14, pp. 3399–3434, 2002, doi: 10.1088/0953-8984/14/13/302.

[26] O. Ambacher *et al.*, "Two-Dimensional Electron Gases Induced by Spontaneous and Piezoelectric Polarization Charges in N- and Ga-Face AlGaN/GaN Heterostructures," *J. Appl. Phys.*, vol. 85, no. 6, pp. 3222-3233, 1999, doi: 10.1063/1.369664.

[27] G. R. Booker and B. A. Joyce, "A study of Nucleation in Chemically Grown Epitaxial Silicon Films using Molecular Beam Techniques," *Philos. Mag. Lett.*, vol. 14, no. 128, pp. 301-315, 1966, doi: 10.1080/14786436608219013.

[28] B. A. Joyce, R. R. Bradley, and G. R. Booker, "A Study of Nucleation in Chemically Grown Epitaxial Silicon Films using Molecular Beam Techniques III. Nucleation Rate Measurements and the Effect of Oxygen on Initial Growth Behaviour," *Philos. Mag. Lett.*, vol. 15, no. 138, pp. 1167-1187, 1967, doi: 10.1080/14786436708222757.

[29] Joyce, B. A., J. H. Neave, and B. E. Watts, "The Influence of Substrate Surface Conditions on the Nucleation and Growth of Epitaxial Silicon Films," *Surf. Sci. Rep.* , no. 15, pp. 1-13, 1969, doi: 10.1016/0039-6028(69)90062-4.

[30] A. Y. Cho, "Morphology of Epitaxial Growth of GaAs by a Molecular Beam Method: The Observation of Surface Structures," *J. Appl. Phys.*, vol. 41, no. 7, pp. 2780-2786, 1970, doi: 10.1063/1.1659315.

[31] J. R. A. A. Y. CHO, "Molecular beam epitaxy," *Progress in Solid-State Chemistry*, vol. 10, 1975.

[32] https://www.veeco.com/products/genxplor-rd-mbe-system/.

[33] B. P. Gunning *et al.*, "Comprehensive Study of the Electronic and Optical Behavior of Highly Degenerate P-Type Mg-Doped GaN and AlGaN," *J. Appl. Phys.*, vol. 117, no. 4, 2015, doi: 10.1063/1.4906464.

[34] S. Zhao *et al.*, "Aluminum Nitride Nanowire Light Emitting Diodes: Breaking the Fundamental Bottleneck of Feep Ultraviolet Light Sources," *Sci. Rep.*, vol. 5, pp. 8332, Feb 16 2015, doi: 10.1038/srep08332.

[35] E. Iliopoulos and T. D. Moustakas, "Growth Kinetics of AlGaN Films by Plasma-Assisted Molecular-Beam Epitaxy," *Appl. Phys. Lett.*, vol. 81, no. 2, pp. 295-297, 2002, doi: 10.1063/1.1492853.

[36] D. V. Nechaev, P. N. Brunkov, S. I. Troshkov, V. N. Jmerik, and S. V. Ivanov, "Pulsed Growth Techniques in Plasma-Assisted Molecular Beam Epitaxy of $Al_xGa_{1-x}N$ layers with Medium Al Content (x=0.4–0.6)," *J. Cryst. Growth*, vol. 425, pp. 9-12, 2015, doi: 10.1016/j.jcrysgro.2015.03.055.

[37] S. V. Novikov, C. R. Staddon, J. Whale, A. J. Kent, and C. T. Foxon, "Growth of Free-Standing Wurtzite AlGaN by MBE using a Highly Efficient RF Plasma Source," *Journal of Vacuum Science & Technology B, Nanotechnology and Microelectronics: Materials, Processing, Measurement, and Phenomena,* vol. 34, no. 2, 2016, doi: 10.1116/1.4940155.

[38] S. V. Novikov, A. J. Kent, and C. T. Foxon, "Molecular Beam Epitaxy as a Growth Technique for Achieving Free-Standing Zinc-Blende GaN and Wurtzite $Al_xGa_{1-x}N$," *Prog. Cryst. Growth Charact. Mater.*, vol. 63, no. 2, pp. 25-39, 2017, doi: 10.1016/j.pcrysgrow.2017.04.001.

[39] D. A. Laleyan *et al.*, "Molecular Beam Epitaxy and Characterization of $Al_{0.6}Ga_{0.4}N$ Epilayers," *J. Cryst. Growth,* vol. 507, pp. 87-92, 2019, doi: 10.1016/j.jcrysgro.2018.10.048.

[40] B. T. Tran, H. Hirayama, N. Maeda, M. Jo, S. Toyoda, and N. Kamata, "Direct Growth and Controlled Coalescence of Thick AlN Template on Micro-circle Patterned Si Substrate," *Sci. Rep.*, vol. 5, pp. 14734, Oct 6 2015, doi: 10.1038/srep14734.

[41] H. Sun *et al.*, "Structural Properties, Crystal Quality and Growth Modes of MOCVD-Grown AlN with TMAl Pretreatment of Sapphire Substrate," *J. Phys. D: Appl. Phys.*, vol. 50, no. 39, 2017, doi: 10.1088/1361-6463/aa8503.

[42] G. Koblmueller, R. Averbeck, L. Geelhaar, H. Riechert, W. Hösler, and P. Pongratz, "Growth Diagram and Morphologies of AlN Thin Films Grown by Molecular Beam Epitaxy," *J. Appl. Phys.*, vol. 93, no. 12, pp. 9591-9596, 2003, doi: 10.1063/1.1575929.

[43] G. Koblmüller, S. Fernández-Garrido, E. Calleja, and J. S. Speck, "In Situ Investigation of Growth Modes during Plasma-Assisted Molecular Beam Epitaxy of (0001) GaN," *Appl. Phys. Lett.*, vol. 91, no. 16, 2007, doi: 10.1063/1.2789691.

[44] M. Feng *et al.*, "Room-Temperature Electrically Injected AlGaN-Based Near-Ultraviolet Laser Grown on Si," *ACS Photonics,* vol. 5, no. 3, pp. 699-704, 2018, doi: 10.1021/acsphotonics.7b01215.

[45] X. Yin, Q. Zhang, and S. Zhao, "Molecular Beam Epitaxial Growth of AlN Thin Films on Si Through Exploiting Low Al Adatom Migration and the Nitrogen-Rich Environment on a Nanowire Template," *Crystal Growth & Design*, vol. 21, no. 7, pp. 3645-3649, 2021, doi: 10.1021/acs.cgd.1c00327.

[46] X. Yin and S. Zhao, "High Internal Quantum Efficiency AlGaN Epilayer Grown by Molecular Beam Epitaxy on Si Substrate," *ECS Journal of Solid State Science and Technology,* vol. 10, no. 7, 2021, doi: 10.1149/2162-8777/ac0f15.

[47] X. Yin and S. Zhao, "Optical Quality and Stimulated Emission of Molecular Beam Epitaxy Grown AlGaN in the Deep Ultraviolet," *physica status solidi (b),* vol. 257, no.12, p. 2000287, 2020, doi: 10.1002/pssb.202000287.

[48] X. Yin and S. Zhao, "Correlation of Defects and Lasing Threshold for AlGaN Deep Ultraviolet Lasers Grown by Molecular Beam Epitaxy," *physica status solidi (b),* vol. 258, no. 11, pp.2100201, 2021, doi: 10.1002/pssb.202100201.

[49] C.-H. Liao, H. Sun, and X. Li, "Ultraviolet Quantum Well Lasers," in *Nanoscale Semiconductor Lasers*, 2019, pp. 139-163.

[50] R. Dingle, K. L. Shaklee, R. F. Leheny, and R. B. Zetterstrom, "Stimulated Emission and Laser Action in Gallium Nitride," *Appl. Phys. Lett.,* vol. 19, no. 1, pp. 5-7, 1971, doi: 10.1063/1.1653730.

[51] S. S. I. Akasaki, H. Sakai, T. Tanaka, M. Koike and H. Amano, "Shortest Wavelength Semiconductor Laser Diode," *Electron. Lett.*, vol. 32, no. 12, 1996.

[52] S. Teramura *et al.*, "High Crystallinity and Highly Relaxed $Al_{0.60}Ga_{0.40}N$ Films Using Growth Mode Control Fabricated on a Sputtered AlN Template with High‐Temperature Annealing," *physica status solidi (a),* vol. 217, no. 14, 2020, doi: 10.1002/pssa.201900868.

[53] X.-H. Li *et al.*, "Low-Threshold Stimulated Emission at 249 nm and 256 nm from AlGaN-Based Multiple-Quantum-Well Lasers Grown on Sapphire Substrates," *Appl. Phys. Lett.*, vol. 105, no. 14, 2014, doi: 10.1063/1.4897527.

[54] M. V. Rzheutski *et al.*, "Ultraviolet Stimulated Emission in AlGaN Layers Grown on Sapphire Substrates using Ammonia and Plasma‐Assisted Molecular Beam Epitaxy," *physica status solidi (a)*, vol. 217, no. 14, pp. 1900927, 2020, doi: 10.1002/pssa.201900927.

[55] P. Chen *et al.*, "Epitaxial Growth and Optically Pumped Stimulated Emission in AlGaN/InGaN Ultraviolet Multi-Quantum-Well Structures," *J. Electron. Mater.*, vol. 49, no. 4, pp. 2326-2331, 2020, doi: 10.1007/s11664-019-07932-x.

[56] J. Jeschke, A. Mogilatenko, C. Netzel, U. Zeimer, and M. Weyers, "Influence of Silicon Doping on Internal Quantum Efficiency and Threshold of Optically Pumped Deep UV AlGaN Quantum Well Lasers," *Semicond. Sci. Technol.*, vol. 34, no. 1, 2019, doi: 10.1088/1361-6641/aaee51.

[57] C. Kuhn *et al.*, "Influence of Waveguide Strain and Surface Morphology on AlGaN-Based Deep UV Laser Characteristics," *J. Phys. D: Appl. Phys.*, vol. 51, no. 41, 2018, doi: 10.1088/1361-6463/aadb84.

[58] J. Yan, Y. Tian, X. Chen, Y. Zhang, J. Wang, and J. Li, "Deep Ultraviolet Lasing from AlGaN Multiple-Quantum-Well Structures," *Phys. Status Solidi C*, vol. 13, no. 5-6, pp. 228-231, 2016, doi: 10.1002/pssc.201510192.

[59] Y. Tian, Y. Zhang, J. Yan, X. Chen, J. Wang, and J. Li, "Stimulated Emission at 272 nm from an $Al_xGa_{1-x}N$-Based Multiple-Quantum-Well Laser with Two-Step Etched Facets," *RSC Advances*, vol. 6, no. 55, pp. 50245-50249, 2016, doi: 10.1039/c6ra11612d.

[60] X.-H. Li *et al.*, "Demonstration of Transverse-Magnetic Deep-Ultraviolet Stimulated Emission from AlGaN Multiple-Quantum-Well Lasers Grown on a Sapphire Substrate," *Appl. Phys. Lett.*, vol. 106, no. 4, pp. 041115, 2015, doi: 10.1063/1.4906590.

[61] V. N. Jmerik *et al.*, "Structural and Optical Properties of PAMBE AlGaN Quantum Well Heterostructures Grown on c-Al_2O_3 By using Flux- and Temperature-Modulated Techniques," *J. Mater. Res.*, vol. 30, no. 19, pp. 2871-2880, 2015, doi: 10.1557/jmr.2015.220.

[62] J. Jeschke *et al.*, "UV-C Lasing From AlGaN Multiple Quantum Wells on Different Types of AlN/Sapphire Templates," *IEEE Photon. Technol. Lett.*, vol. 27, no. 18, pp. 1969-1972, 2015, doi: 10.1109/lpt.2015.2448127.

[63] S. V. Ivanov *et al.*, "Plasma-Assisted Molecular Beam Epitaxy of Al(Ga)N Layers and Quantum Well Structures for Optically Pumped Mid-UV Lasers on c-Al_2O_3," *Semicond. Sci. Technol.*, vol. 29, no. 8, 2014, doi: 10.1088/0268-1242/29/8/084008.

[64] F. Asif *et al.*, "Deep Ultraviolet Photopumped Stimulated Emission from Partially Relaxed AlGaN Multiple Quantum Well Heterostructures Grown on Sapphire Substrates," *Journal of Vacuum Science & Technology B, Nanotechnology and Microelectronics: Materials, Processing, Measurement, and Phenomena,* vol. 32, no. 6, 2014, doi: 10.1116/1.4898694.

[65] E. V. Lutsenko *et al.*, "Spontaneous and Stimulated Emission in the Mid-Ultraviolet Range of Quantum-Well Heterostructures Based on AlGaN Compounds Grown by Molecular Beam Epitaxy on c-Sapphire Substrates," *Phys. Solid State* , vol. 55, no. 10, pp. 2173-2181, 2013, doi: 10.1134/s106378341310020x.

[66] V. N. Jmerik, E. V. Lutsenko, and S. V. Ivanov, "Plasma-Assisted Molecular Beam Epitaxy of AlGaN Heterostructures for Deep-Ultraviolet Optically Pumped Lasers," *physica status solidi (a),* vol. 210, no. 3, pp. 439-450, 2013, doi: 10.1002/pssa.201300006.

[67] V. N. Jmerik *et al.*, "Low-Threshold 303 nm Lasing in AlGaN-Based Multiple-Quantum Well Structures with an Asymmetric Waveguide Grown by Plasma-Assisted Molecular

Beam Epitaxy on c-Sapphire," *Appl. Phys. Lett.*, vol. 96, no. 14, 2010, doi: 10.1063/1.3373834.

[68] M. Shatalov, M. Gaevski, V. Adivarahan, and A. Khan, "Room-Temperature Stimulated Emission from AlN at 214 nm," *Jpn. J. Appl. Phys.*, vol. 45, no. No. 49, pp. L1286-L1288, 2006, doi: 10.1143/jjap.45.L1286.

[69] R. Kirste *et al.*, "6 kW/cm2 UVC Laser Threshold in Optically Pumped Lasers Achieved by Controlling Point Defect Formation," *Appl. Phys. Express*, vol. 11, no. 8, pp. 082101, 2018, doi: 10.7567/apex.11.082101.

[70] Q. Guo *et al.*, "Design of AlGaN-based Quantum Structures for Low Threshold UVC Lasers," *J. Appl. Phys.*, vol. 126, no. 22, 2019, doi: 10.1063/1.5125256.

[71] M. Lachab *et al.*, "Optical Polarization Control of Photo-Pumped Stimulated Emissions at 238 nm from AlGaN Multiple-Quantum-Well Laser Structures on AlN Substrates," *Appl. Phys. Express*, vol. 10, no. 1, 2017, doi: 10.7567/apex.10.012702.

[72] J. Xie *et al.*, "Lasing and Longitudinal Cavity Modes in Photo-Pumped Deep Ultraviolet AlGaN Heterostructures," *Appl. Phys. Lett.*, vol. 102, no. 17, 2013, doi: 10.1063/1.4803689.

[73] Z. Lochner *et al.*, "Deep-Ultraviolet Lasing at 243 nm from Photo-Pumped AlGaN/AlN Heterostructure on AlN Substrate," *Appl. Phys. Lett.*, vol. 102, no. 10, 2013, doi: 10.1063/1.4795719.

[74] T. Wunderer *et al.*, "Pseudomorphically Grown Ultraviolet C Photopumped Lasers on Bulk AlN Substrates," *Appl. Phys. Express*, vol. 4, no. 9, 2011, doi: 10.1143/apex.4.092101.

[75] L. van Deurzen, R. Page, V. Protasenko, K. Nomoto, H. Xing, and D. Jena, "Optically Pumped Deep-UV Multimode Lasing in AlGaN Double Heterostructure Grown by

Molecular Beam Homoepitaxy," *AIP Advances,* vol. 12, no. 3, 2022, doi: 10.1063/5.0085365.

[76] S. Nakamura *et al.*, "Room ‐ Temperature Continuous ‐ Wave Operation of InGaN Multi ‐ Quantum ‐ Well Structure Laser Diodes," *Appl. Phys. Lett.*, vol. 69, no. 26, pp. 4056-4058, 1996, doi: 10.1063/1.117816.

[77] T. Y. Shin-ichi NAGAHAMA, Masahiko SANO and Takashi MUKAI, "Ultraviolet GaN Single Quantum Well Laser Diodes," *Jpn. J. Appl. Phys.*, vol. 40, pp. L785-L787, 2001, doi: 10.1143/JJAP.40.L785.

[78] S.-i. Nagahama, T. Yanamoto, M. Sano, and T. Mukai, "Study of GaN-based Laser Diodes in Near Ultraviolet Region," *Jpn. J. Appl. Phys.*, vol. 41, no. Part 1, No. 1, pp. 5-10, 2002, doi: 10.1143/jjap.41.5.

[79] D. W. T. Michael Kneissl, Mark Teepe, et al., "Continuous-Wave Operation of Ultraviolet InGaN/InAlGaN Multiple-Quantum-Well Laser Diodes," *Appl. Phys. Lett*, no. 82, p. 2386, 2003, doi: 10.1063/1.1568160.

[80] J. Edmond *et al.*, "High Efficiency GaN-Based LEDs and Lasers on SiC," *J. Cryst. Growth,* vol. 272, no. 1-4, pp. 242-250, 2004, doi: 10.1016/j.jcrysgro.2004.08.056.

[81] Z. Zhang *et al.*, "Continuous-Wave Lasing of AlGaN-Based Ultraviolet Laser Diode at 274.8 nm by Current Injection," *Appl. Phys. Express,* vol. 15, no. 4, pp. 041007, 2022, doi: 10.35848/1882-0786/ac6198.

[82] Z. Zhang *et al.*, "Key Temperature-Dependent Characteristics of AlGaN-Based UV-C Laser Diode and Demonstration of Room-Temperature Continuous-Wave Lasing," *Appl. Phys. Lett.*, vol. 121, no. 22, 2022, doi: 10.1063/5.0124480.

[83] T. Sakai *et al.*, "On-Wafer Fabrication of Etched-Mirror UV-C Laser Diodes with the ALD-Deposited DBR," *Appl. Phys. Lett.*, vol. 116, no. 12, 2020, doi: 10.1063/1.5145017.

[84] M. Kneissl *et al.*, "Ultraviolet Semiconductor Laser Diodes on Bulk AlN," *J. Appl. Phys.*, vol. 101, no. 12, 2007, doi: 10.1063/1.2747546.

[85] S. Tanaka *et al.*, "AlGaN-Based UV-B Laser Diode with a High Optical Confinement Factor," *Appl. Phys. Lett.,* vol. 118, no. 16, 2021, doi: 10.1063/5.0046224.

[86] H. Tsuzuki *et al.*, "Novel UV Devices on High-Quality AlGaN using Grooved Underlying Layer," *J. Cryst. Growth,* vol. 311, no. 10, pp. 2860-2863, 2009, doi: 10.1016/j.jcrysgro.2009.01.031.

[87] H. Yoshida, M. Kuwabara, Y. Yamashita, Y. Takagi, K. Uchiyama, and H. Kan, "AlGaN-Based Laser Diodes for the Short-Wavelength Ultraviolet Region," *Nat. Photon.* , vol. 11, no. 12, pp. 125013, 2009, doi: 10.1088/1367-2630/11/12/125013.

[88] H. Tsuzuki *et al.*, "High-Performance UV Emitter grown on High-Crystalline-Quality AlGaN Underlying Layer," *physica status solidi (a),* vol. 206, no. 6, pp. 1199-1204, 2009, doi: 10.1002/pssa.200880784.

[89] M. H. Crawford, A. A. Allerman, A. M. Armstrong, M. L. Smith, and K. C. Cross, "Laser Diodes with 353 nm Wavelength Enabled by Reduced-Dislocation-Density AlGaN Templates," *Appl. Phys. Express,* vol. 8, no. 11, 2015, doi: 10.7567/apex.8.112702.

[90] K. Nagata *et al.*, "Injection Efficiency in AlGaN‐Based UV Laser Diodes," *physica status solidi c,* vol. 8, no. 7-8, pp. 2384-2386, 2011, doi: 10.1002/pssc.201001008.

[91] S. Tanaka *et al.*, "AlGaN-Based UV-B Laser Diode with a Wavelength of 290 nm on 1 μm Periodic Concavo–Convex Pattern AlN on a Sapphire Substrate," *Appl. Phys. Express,* vol. 14, no. 5, pp. 055505, 2021, doi: 10.35848/1882-0786/abf763.

[92] S. I. Tomoya Omori, Shunya Tanaka, Shinji Yasue, Kosuke Sato *et al.*, "Internal Loss of AlGaN-Based Ultraviolet-B Band Laser Diodes with P-Type AlGaN Cladding Layer using Polarization Doping," *Appl. Phys. Express*, vol. 13, pp. 071008, 2020, doi: 10.35848/1882-0786/ab9e4a.

[93] M. Iwaya *et al.*, "Recent Development of UV-B Laser Diodes," *Jpn. J. Appl. Phys.*, vol. 61, no. 4, pp. 040501, 2022, doi: 10.35848/1347-4065/ac3be8.

[94] F. Liang *et al.*, "AlGaN-Based Schottky Barrier Deep Ultraviolet Photodetector Grown on Si Substrate," *Opt. Express*, vol. 28, no. 12, pp. 17188-17195, 2020, doi: 10.1364/oe.389767.

[95] Y. Huang *et al.*, "Crack-Free High Quality 2 μm-Thick $Al_{0.5}Ga_{0.5}N$ Grown on a Si Substrate with a Superlattice Transition Layer," *CrystEngComm*, vol. 22, no. 7, pp. 1160-1165, 2020, doi: 10.1039/c9ce01677e.

[96] K. Ding, V. Avrutin, Ü. Özgür, and H. Morkoç, "Status of Growth of Group III-Nitride Heterostructures for Deep Ultraviolet Light-Emitting Diodes," *Crystals*, vol. 7, no.10, pp. 300, 2017, doi: 10.20944/preprints201709.0013.v1.

[97] K. Ban *et al.*, "Internal Quantum Efficiency of Whole-Composition-Range AlGaN Multiquantum Wells," *Appl. Phys. Express*, vol. 4, no. 5, 2011, doi: 10.1143/apex.4.052101.

[98] K. Cheng *et al.*, "AlGaN-based Heterostructures Grown on 4 Inch Si(111) by MOVPE," *Phys. Status Solidi C*, vol. 5, no. 6, pp. 1600-1602, 2008, doi: 10.1002/pssc.200778518.

[99] P. Saengkaew *et al.*, "Low-Temperature/High-Temperature AlN Superlattice Buffer Layers for High-Quality $Al_xGa_{1-x}N$ on Si (111)," *J. Cryst. Growth*, vol. 311, no. 14, pp. 3742-3748, 2009, doi: 10.1016/j.jcrysgro.2009.04.038.

[100] J. B. a. A. Reiher, A. Dadgar, A. Diez, A. Krost, "Efficient Stress Relief in GaN Heteroepitaxy on Si(1 1 1) using Low-Temperature AlN Interlayers," *J. Cryst. Growth*, vol. 248, pp. 563–567, 2003.

[101] X. Pan *et al.*, "Surface Characterization of AlGaN Grown on Si (111) Substrates," *J. Cryst. Growth,* vol. 331, no. 1, pp. 29-32, 2011, doi: 10.1016/j.jcrysgro.2011.07.011.

[102] Y. N. M. Sergey Yu. Karpov, "Dislocation Effect on Light Emission Efficiency in Gallium Nitride," *Appl. Phys. Lett.*, vol. 81, pp. 4721–4723, 2002, doi: 10.1063/1.1527225.

[103] P. Saengkaew *et al.*, "MOVPE Growth of High-Quality $Al_{0.1}Ga_{0.9}N$ on Si(111) Substrates for UV-LEDs," *Phys. Status Solidi C,* vol. 6, no. S2, pp. S455-S458, 2009, doi: 10.1002/pssc.200880917.

[104] X.-H. Li *et al.*, "Demonstration of Transverse-Magnetic Deep-Ultraviolet Stimulated Emission from AlGaN Multiple-Quantum-Well Lasers Grown on a Sapphire Substrate," *Appl. Phys. Lett.*, vol. 106, no. 4, 2015, doi: 10.1063/1.4906590.

[105] A. A. Allerman, M. H. Crawford, S. R. Lee, and B. G. Clark, "Low Dislocation Density AlGaN Epilayers by Epitaxial Overgrowth of Patterned Templates," *J. Cryst. Growth,* vol. 388, pp. 76-82, 2014, doi: 10.1016/j.jcrysgro.2013.11.052.

[106] Y. Zhang *et al.*, "Near Milliwatt Power AlGaN-based Ultraviolet Light Emitting Diodes Based on Lateral Epitaxial Overgrowth of AlN on Si(111)," *Appl. Phys. Lett.,* vol. 102, no. 1, 2013, doi: 10.1063/1.4773565.

[107] T. Mino, H. Hirayama, T. Takano, K. Tsubaki, and M. Sugiyama, "Characteristics of Epitaxial Lateral Overgrowth AlN Templates on (111)Si Substrates for AlGaN Deep-UV LEDs Fabricated on Different Direction Stripe Patterns," *Phys. Status Solidi C,* vol. 9, no. 3-4, pp. 802-805, 2012, doi: 10.1002/pssc.201100380.

[108] E. Cicek, R. McClintock, C. Y. Cho, B. Rahnema, and M. Razeghi, "$Al_xGa_{1-x}N$-Based Solar-Blind Ultraviolet Photodetector Based on Lateral Epitaxial Overgrowth of AlN on Si Substrate," *Appl. Phys. Lett.*, vol. 103, no. 18, 2013, doi: 10.1063/1.4828497.

[109] B. T. Tran and H. Hirayama, "Growth and Fabrication of High External Quantum Efficiency AlGaN-Based Deep Ultraviolet Light-Emitting Diode Grown on Pattern Si Substrate," *Sci. Rep.*, vol. 7, no. 1, pp. 12176, Sep 22 2017, doi: 10.1038/s41598-017-11757-1.

[110] Z. Bryan, I. Bryan, J. Xie, S. Mita, Z. Sitar, and R. Collazo, "High Internal Quantum Efficiency in AlGaN Multiple Quantum Wells Grown on Bulk AlN Substrates," *Appl. Phys. Lett.*, vol. 106, no. 14, 2015, doi: 10.1063/1.4917540.

[111] Z. Li *et al.*, "High-Power AlGaN-Based Near-Ultraviolet Light-Emitting Diodes Grown on Si(111)," *Appl. Phys. Express*, vol. 10, no. 7, 2017, doi: 10.7567/apex.10.072101.

[112] R. M. N. T. Mattila, "Ab Initio Study of Oxygen Point Defects in GaAs, GaN, and AlN," *Phys. Rev. B.*, vol. 54, no.23, pp.16676, 1996, doi.org/10.1103/PhysRevB.54.16676.

[113] R. M. N. T. Mattila, "Point-Defect Complexes and Broadband Luminescence in GaN and AlN," *Phys. Rev. B.*, vol. 55, no. 15, pp. 9571, 1997, doi.org/10.1103/PhysRevB.55.9571.

[114] M. L. N. K. B. Nam, J. Y. Lin, and H. X. Jiang, "Deep Impurity Transitions Involving Cation Vacancies and Complexes in AlGaN Alloys," *Appl. Phys. Lett.*, vol. 86, pp. 222108, 2005, doi: 10.1063/1.1943489.

[115] M. L. N. N. Nepal, J. Y. Lin, and H. X. Jiang, "Photoluminescence Studies of Impurity Transitions in AlGaN Alloys," *Appl. Phys. Lett.*, vol. 89, pp. 092107, 2006, doi: 10.1063/1.2337856.

[116] N. N. M. L. Nakarmi, J. Y. Lin, and H. X. Jiang, "Photoluminescence Studies of Impurity Transitions in Mg-Doped AlGaN Alloys," *Appl. Phys. Lett.*, vol. 94, 2009, doi: 10.1063/1.3094754.

[117] R. Collazo *et al.*, "Progress on n-Type Doping of AlGaN Alloys on AlN Single Crystal Substrates for UV Optoelectronic Applications," *Phys. Status Solidi C*, vol. 8, no. 7-8, pp. 2031-2033, 2011, doi: 10.1002/pssc.201000964.

[118] C. J. Zollner *et al.*, "Highly Conductive n-$Al_{0.65}Ga_{0.35}N$ Grown by MOCVD Using Low V/III Ratio," *Crystals*, vol. 11, no. 8, 2021, doi: 10.3390/cryst11081006.

[119] J. Wang *et al.*, "High Conductivity n-$Al_{0.6}Ga_{0.4}N$ by Ammonia-Assisted Molecular Beam Epitaxy for Buried Tunnel Junctions in UV Emitters," *Opt. Express*, vol. 29, no. 25, pp. 40781-40794, 2021, doi: 10.1364/oe.436153.

[120] D. J. Chadi and K. J. Chang, "Theory of the Atomic and Electronic Structure of DX Centers in GaAs and $Al_xGa_{1-x}As$ Alloys," *Phys. Rev. Lett.*, vol. 61, no. 7, pp. 873-876, Aug 15 1988, doi: 10.1103/PhysRevLett.61.873.

[121] F. Mehnke *et al.*, "Electronic Properties of Si-Doped $Al_xGa_{1-x}N$ with Aluminum Mole Fractions Above 80%," *J. Appl. Phys.*, vol. 120, no. 14, 2016, doi: 10.1063/1.4964442.

[122] X. T. Trinh, D. Nilsson, I. G. Ivanov, E. Janzén, A. Kakanakova-Georgieva, and N. T. Son, "Stable and Metastable Si Negative-U Centers in AlGaN and AlN," *Appl. Phys. Lett.*, vol. 105, no. 16, 2014, doi: 10.1063/1.4900409.

[123] K. B. Nam, M. L. Nakarmi, J. Li, J. Y. Lin, and H. X. Jiang, "Mg Acceptor Level in AlN Probed by Deep Ultraviolet Photoluminescence," *Appl. Phys. Lett.*, vol. 83, no. 5, pp. 878-880, 2003, doi: 10.1063/1.1594833.

[124] V. P. John Simon, Chuanxin Lian, Huili Xing, Debdeep Jena, "Polarization-Induced Hole Doping in Wide–Band-Gap Uniaxial Semiconductor Heterostructures," *Sci,* vol. 327, no.5961, pp. 60-64, 2010, doi: 10.1126/science.1183226.

[125] S. Nikishin, A. Bernussi, and S. Karpov, "Towards Efficient Electrically-Driven Deep UVC Lasing: Challenges and Opportunities," *Nanomaterials (Basel),* vol. 13, no. 1, pp.185, 2022, doi: 10.3390/nano13010185.

[126] P. Bagheri *et al.*, "Doping and Compensation in Heavily Mg Doped Al-Rich AlGaN Films," *Appl. Phys. Lett.*, vol. 120, no. 8, 2022, doi: 10.1063/5.0082992.

[127] W. Luo *et al.*, "Enhanced p-Type Conduction in AlGaN Grown by Metal-Source Flow-Rate modulation epitaxy," *Appl. Phys. Lett.*, vol. 113, no. 7, 2018, doi: 10.1063/1.5040334.

[128] T. Kinoshita, T. Obata, H. Yanagi, and S.-i. Inoue, "High P-Type Conduction in High-Al Content Mg-doped AlGaN," *Appl. Phys. Lett.*, vol. 102, no. 1, 2013, doi: 10.1063/1.4773594.

[129] R. Z. P. Chena, Z.M. Zhaoa, D.J. Xia, B. Shena, Z.Z. Chena, Y.G. Zhoua, S.Y. Xiea, W.F. Lub, Y.D. Zhenga, "Investigation of Mg Doping in High-Al Content P-Type $Al_xGa_{1-x}N$ ($0.3 < x < 0.5$)," *Appl. Phys. Lett.*, vol. 86, pp. 082107, 2005, doi: 10.1063/1.1867565.

[130] K. Ebata, J. Nishinaka, Y. Taniyasu, and K. Kumakura, "High Hole Concentration in Mg-Doped AlN/AlGaN Superlattices with High Al Content," *Jpn. J. Appl. Phys.*, vol. 57, no. 4S, 2018, doi: 10.7567/jjap.57.04fh09.

[131] R. D. a. B. Moody, "Polarization-Induced Doping in Graded AlGaN Epilayers Grown on AlN Single Crystal Substrates," *ECS Transactions,* vol. 86, no. 12, pp. 31-40, 2018, doi: 10.1149/08612.0031ecst.

[132] Z. Zhang *et al.*, "Space Charge Profile Study of AlGaN-Based p-Type Distributed Polarization Doped Claddings without Impurity Doping for UV-C Laser Diodes," *Appl. Phys. Lett.,* vol. 117, no. 15, 2020, doi: 10.1063/5.0027789.

[133] X. Qiu and H. Jiang, "Highly Conductive and 260 nm Transparent p-Type $Al_{0.6}Ga_{0.4}N$ Achieved Utilizing Interface Doping Effects," *Crystal Growth & Design,* vol. 21, no. 4, pp. 2389-2397, 2021, doi: 10.1021/acs.cgd.1c00020.

[134] X. Qiu, Y. Chen, E. Han, Z. Lv, Z. Song, and H. Jiang, "High Doping Efficiency in p-Type Al-Rich AlGaN by Modifying the Mg Doping Planes," *Materials Advances,* vol. 1, no. 1, pp. 77-85, 2020, doi: 10.1039/d0ma00026d.

[135] C. Stampfl and C. G. Van de Walle, "Theoretical Investigation of Native Defects, Impurities, and Complexes in Aluminum Nitride," *Phys. Rev. B.,* vol. 65, no. 15, 2002, doi: 10.1103/PhysRevB.65.155212.

[136] P. Sun *et al.*, "Advantages of AlGaN-Based Deep Ultraviolet Light-Emitting Diodes with a Superlattice Electron Blocking Layer," *Superlattices Microstruct.* , vol. 85, pp. 59-66, 2015, doi: 10.1016/j.spmi.2015.05.010.

[137] Y.-H. Shih *et al.,* "Design of Hole-Blocking and Electron-Blocking Layers in $Al_xGa_{1-x}N$-Based UV Light-Emitting Diodes," *IEEE Trans. Electron Devices,* vol. 63, no. 3, pp. 1141-1147, 2016, doi: 10.1109/ted.2016.2520998.

[138] B. So, J. Kim, E. Shin, T. Kwak, T. Kim, and O. Nam, "Efficiency Improvement of Deep-Ultraviolet Light Emitting Diodes with Gradient Electron Blocking Layers," *physica status solidi (a),* vol. 215, no. 10, 2018, doi: 10.1002/pssa.201700677.

[139] X. Fan *et al.*, "Efficiency improvements in AlGaN-Based Deep Ultraviolet Light-Emitting Diodes using Inverted-V-Shaped Graded Al Composition Electron Blocking Layer," *Superlattices Microstruct.*, vol. 88, pp. 467-473, 2015, doi: 10.1016/j.spmi.2015.10.003.

[140] J.-Y. Chang, H.-T. Chang, Y.-H. Shih, F.-M. Chen, M.-F. Huang, and Y.-K. Kuo, "Efficient Carrier Confinement in Deep-Ultraviolet Light-Emitting Diodes With Composition-Graded Configuration," *IEEE Trans. Electron Devices,* vol. 64, no. 12, pp. 4980-4984, 2017, doi: 10.1109/ted.2017.2761404.

[141] Z.-H. Zhang *et al.*, "Hole Transport Manipulation To Improve the Hole Injection for Deep Ultraviolet Light-Emitting Diodes," *ACS Photonics,* vol. 4, no. 7, pp. 1846-1850, 2017, doi: 10.1021/acsphotonics.7b00443.

[142] B. So *et al.*, "Improved Carrier Injection of AlGaN-Based Deep Ultraviolet Light Emitting Diodes with Graded Superlattice Electron Blocking Layers," *RSC Advances,* vol. 8, no. 62, pp. 35528-35533, 2018, doi: 10.1039/c8ra06982d.

[143] Z.-H. Zhang *et al.*, "Increasing the Hole Energy by Grading the Alloy Composition of the p-Type Electron Blocking Layer for Very High-Performance Deep Ultraviolet Light-Emitting Diodes," *Photonics Research*, vol. 7, no. 4, pp. B1-B6, 2019, doi: 10.1364/prj.7.0000b1.

[144] Z. H. Zhang *et al.*, "Nearly Efficiency-Droop-Free AlGaN-Based Ultraviolet Light-Emitting Diodes with a Specifically Designed Superlattice p-Type Electron Blocking Layer for High Mg Doping Efficiency," *Nanoscale Res Lett*, vol. 13, no. 1, pp. 122, 2018, doi: 10.1186/s11671-018-2539-9.

[145] C. Chu *et al.*, "On the $Al_xGa_{1-x}N/Al_yGa_{1-y}N/Al_xGa_{1-x}N$ (x>y) p-Electron Blocking Layer to Improve the Hole Injection for AlGaN Based Deep Ultraviolet Light-Emitting Diodes," *Superlattices Microstruct.*, vol. 113, pp. 472-477, 2018, doi: 10.1016/j.spmi.2017.11.029.

[146] C. Chu *et al.*, "On the Origin of Enhanced Hole Injection for AlGaN-Based Deep Ultraviolet Light-Emitting Diodes with AlN Insertion Layer in p-Electron Blocking Layer," *Opt. Express*, vol. 27, no. 12, pp. A620-A628, Jun 10 2019, doi: 10.1364/OE.27.00A620.

[147] L. Li, Y. Miyachi, M. Miyoshi, and T. Egawa, "Ultrathin Inserted AlGaN/InAlN Heterojunction for Performance Improvement in AlGaN-Based Deep Ultraviolet Light-Emitting Diodes," *Appl. Phys. Express*, vol. 12, no. 1, 2019, doi: 10.7567/1882-0786/aaf62b.

[148] H. Hirayama, Y. Tsukada, T. Maeda, and N. Kamata, "Marked Enhancement in the Efficiency of Deep-Ultraviolet AlGaN Light-Emitting Diodes by Using a Multiquantum-Barrier Electron Blocking Layer," *Appl. Phys. Express*, vol. 3, no. 3, 2010, doi: 10.1143/apex.3.031002.

[149] L. He *et al.*, "Efficient Carrier Transport for 368 nm Ultraviolet LEDs with a p-AlInGaN/AlGaN Short-Period Superlattice Electron Blocking Layer," *Journal of Materials Chemistry C*, vol. 9, no. 25, pp. 7893-7899, 2021, doi: 10.1039/d1tc02191e.

[150] L. He *et al.*, "Marked Enhancement in the Efficiency of Deep Ultraviolet Light-Emitting Diodes by using a $Al_xGa_{1-x}N$ Carrier Reservoir Layer," *Appl. Phys. Express*, vol. 12, no. 6, 2019, doi: 10.7567/1882-0786/ab22df.

[151] S. Chen *et al.*, "Numerical Analysis on the Effects of Multi-Quantum Last Barriers in AlGaN-Based Ultraviolet Light-Emitting Diodes," *Appl. Phys. A*, vol. 118, no. 4, pp. 1357-1363, 2014, doi: 10.1007/s00339-014-8888-z.

[152] X. Ji *et al.*, "Tailoring of Energy Band in Electron-Blocking Structure Enhancing the Efficiency of AlGaN-Based Deep Ultraviolet Light-Emitting Diodes," *IEEE Photonics Journal*, vol. 8, no. 3, pp. 1-7, 2016, doi: 10.1109/jphot.2016.2553848.

[153] B. Cheng *et al.*, "Enhanced Vertical and Lateral Hole Transport in High Aluminum-Containing AlGaN for Deep Ultraviolet Light Emitters," *Appl. Phys. Lett.*, vol. 102, no. 23, 2013, doi: 10.1063/1.4809947.

[154] M. Martens *et al.*, "Low Absorption Loss p-AlGaN Superlattice Cladding Layer for Current-Injection Deep Ultraviolet Laser Diodes," *Appl. Phys. Lett.*, vol. 108, no. 15, 2016, doi: 10.1063/1.4947102.

[155] N. Susilo *et al.*, "AlGaN-Based Deep UV LEDs Grown on Sputtered and High Temperature Annealed AlN/Sapphire," *Appl. Phys. Lett.*, vol. 112, no. 4, 2018, doi: 10.1063/1.5010265.

[156] S. Li *et al.*, "Polarization Induced Hole Doping in Graded $Al_xGa_{1-x}N$ ($x = 0.7 \sim 1$) Layer Grown by Molecular Beam Epitaxy," *Appl. Phys. Lett.*, vol. 102, no. 6, 2013, doi: 10.1063/1.4792685.

[157] K. Sato *et al.*, "Effects of Mg Dopant in Al-Composition-Graded $Al_xGa_{1-x}N$ ($0.45 \leq x$) on Vertical Electrical Conductivity of Ultrawide Bandgap AlGaN p–n Junction," *Appl. Phys. Express*, vol. 14, no. 9, 2021, doi: 10.35848/1882-0786/ac1d64.

[158] D. Jena *et al.*, "Realization of Wide Electron Slabs by Polarization Bulk Doping in Graded III–V Nitride Semiconductor Alloys," *Appl. Phys. Lett.*, vol. 81, no. 23, pp. 4395-4397, 2002, doi: 10.1063/1.1526161.

[159] S. Zhao, S. M. Sadaf, S. Vanka, Y. Wang, R. Rashid, and Z. Mi, "Sub-Milliwatt AlGaN Nanowire Tunnel Junction Deep Ultraviolet Light Emitting Diodes on Silicon Operating at 242 nm," *Appl. Phys. Lett.*, vol. 109, no. 20, 2016, doi: 10.1063/1.4967837.

[160] S. M. Sadaf *et al.*, "An AlGaN Core-Shell Tunnel Junction Nanowire Light-Emitting Diode Operating in the Ultraviolet-C Band," *Nano Lett.*, vol. 17, no. 2, pp. 1212-1218, Feb 8 2017, doi: 10.1021/acs.nanolett.6b05002.

[161] Y. Zhang *et al.*, "Tunnel-Injected Sub 290 nm Ultra-Violet Light Emitting Diodes with 2.8% External Quantum Efficiency," *Appl. Phys. Lett.*, vol. 112, no. 7, 2018, doi: 10.1063/1.5017045.

[162] Y. Zhang *et al.*, "Reflective Metal/Semiconductor Tunnel Junctions for Hole Injection in AlGaN UV LEDs," *Appl. Phys. Lett.*, vol. 111, no. 5, 2017, doi: 10.1063/1.4997328.

[163] A. Pandey, J. Gim, R. Hovden, and Z. Mi, "An AlGaN Tunnel Junction Light Emitting Diode Operating at 255 nm," *Appl. Phys. Lett.*, vol. 117, no. 24, 2020, doi: 10.1063/5.0036286.

[164] Y. Wang *et al.*, "Calculating the Effect of AlGaN Dielectric Layers in a Polarization Tunnel Junction on the Performance of AlGaN-Based Deep-Ultraviolet Light-Emitting Diodes," *Nanomaterials*, vol. 11, no. 12, 2021, doi: 10.3390/nano11123328.

[165] S. Arafin, S. M. N. Hasan, Z. Jamal-Eddine, D. Wickramaratne, B. Paul, and S. Rajan, "Design of AlGaN-Based Lasers with a Buried Tunnel Junction for Sub-300 nm Emission," *Semicond. Sci. Technol.*, vol. 34, no. 7, pp. 3328, 2019, doi: 10.1088/1361-6641/ab19cd.

[166] A. Pandey, J. Gim, R. Hovden, and Z. Mi, "Electron Overflow of AlGaN Deep Ultraviolet Light Emitting Diodes," *Appl. Phys. Lett.*, vol. 118, no. 24, 2021, doi: 10.1063/5.0055326.

[167] C. Kuhn *et al.*, "MOVPE-Grown AlGaN-Based Tunnel Heterojunctions Enabling Fully Transparent UVC LEDs," *Photonics Research*, vol. 7, no. 5, pp. B7-B11, 2019, doi: 10.1364/prj.7.0000b7.

[168] R. Arefin *et al.*, "Theoretical Analysis of Tunnel-Injected Sub-300 nm AlGaN Laser Diodes," *IEEE J. Quantum Electron.*, vol. 56, no. 6, pp. 1-10, 2020, doi: 10.1109/jqe.2020.3021404.

[169] Y. Zhang *et al.*, "Tunnel-Injected Sub-260 nm Ultraviolet Light Emitting Diodes," *Appl. Phys. Lett.*, vol. 110, no. 20, 2017, doi: 10.1063/1.4983352.

[170] K. B. Nam, J. Li, M. L. Nakarmi, J. Y. Lin, and H. X. Jiang, "Unique Optical Properties of AlGaN Alloys and Related Ultraviolet Emitters," *Appl. Phys. Lett.*, vol. 84, no. 25, pp. 5264-5266, 2004, doi: 10.1063/1.1765208.

[171] W. W. Chow and M. Kneissl, "Laser Gain Properties of AlGaN Quantum Wells," *J. Appl. Phys.*, vol. 98, no. 11, pp. 114502, 2005, doi: 10.1063/1.2128495.

[172] C. Liu, Y. K. Ooi, S. M. Islam, H. Xing, D. Jena, and J. Zhang, "234 nm and 246 nm AlN-Delta-GaN Quantum Well Deep Ultraviolet Light-Emitting Diodes," *Appl. Phys. Lett.*, vol. 112, no. 1, 2018, doi: 10.1063/1.5007835.

[173] K. Kamiya, Y. Ebihara, K. Shiraishi, and M. Kasu, "Structural Design of AlN/GaN Superlattices for Deep-Ultraviolet Light-Emitting Diodes with High Emission Efficiency," *Appl. Phys. Lett.*, vol. 99, no. 15, 2011, doi: 10.1063/1.3651335.

[174] Y. Taniyasu and M. Kasu, "Polarization Property of Deep-Ultraviolet Light Emission from c-plane AlN/GaN Short-Period Superlattices," *Appl. Phys. Lett.*, vol. 99, no. 25, 2011, doi: 10.1063/1.3671668.

[175] D. Bayerl, S. M. Islam, C. M. Jones, V. Protasenko, D. Jena, and E. Kioupakis, "Deep Ultraviolet Emission from Ultra-Thin GaN/AlN Heterostructures," *Appl. Phys. Lett.*, vol. 109, no. 24, 2016, doi: 10.1063/1.4971968.

[176] G. Greco, F. Iucolano, and F. Roccaforte, "Ohmic Contacts to Gallium Nitride Materials," *Appl. Surf. Sci.*, vol. 383, pp. 324-345, 2016, doi: 10.1016/j.apsusc.2016.04.016.

[177] Y. Zhang *et al.*, "Demonstration of N-Polar III-Nitride Tunnel Junction LED," *ACS Photonics*, vol. 7, no. 7, pp. 1723-1728, 2020, doi: 10.1021/acsphotonics.0c00269.

[178] Y. Zhang, Z. Jamal-Eddine, and S. Rajan, "Recent Progress of Tunnel Junction-Based Ultra-Violet Light Emitting Diodes," *Jpn. J. Appl. Phys.*, vol. 58, no. SC, 2019, doi: 10.7567/1347-4065/ab1254.

[179] J.-R. van Look *et al.*, "Laser Scribing for Facet Fabrication of InGaN MQW Diode Lasers on Sapphire Substrates," *IEEE Photon. Technol. Lett* , vol. 22, no. 6, pp. 416-418, 2010, doi: 10.1109/lpt.2009.2039995.

[180] H. Zhu, D. E. Niesz, V. A. Greenhut, and R. Sabia, "The Effect of Abrasive Hardness on the Chemical-Assisted Polishing of (0001) Plane Sapphire," *J. Mater. Res.*, vol. 20, no. 2, pp. 504-520, 2011, doi: 10.1557/jmr.2005.0072.

[181] S. Fan, S. Zhao, X. Liu, and Z. Mi, "Study on the Coalescence of Dislocation-Free GaN Nanowires on Si and SiO_x," *Journal of Vacuum Science & Technology B, Nanotechnology and Microelectronics: Materials, Processing, Measurement, and Phenomena*, vol. 32, no. 2, 2014, doi: 10.1116/1.4865915.

[182] Y. Wu, Y. Wang, K. Sun, A. Aiello, P. Bhattacharya, and Z. Mi, "Molecular Beam Epitaxy and Characterization of Mg-Doped GaN Epilayers Grown on Si (0 0 1) Substrate Through Controlled Nanowire Coalescence," *J. Cryst. Growth*, vol. 498, pp. 109-114, 2018, doi: 10.1016/j.jcrysgro.2018.06.008.

[183] Averett, K. L., *et al.*, "Epitaxial Overgrowth of GaN Nanocolumns," *Journal of Vacuum Science & Technology B: Microelectronics and Nanometer Structures Processing, Measurement, and Phenomena* vol. 25, pp. 964–968, 2007, doi: 10.1116/1.2717195.

[184] V. Consonni, M. Knelangen, U. Jahn, A. Trampert, L. Geelhaar, and H. Riechert, "Effects of Nanowire Coalescence on their Structural and Optical Properties on a Local Scale," *Appl. Phys. Lett.,* vol. 95, no. 24, 2009, doi: 10.1063/1.3275793.

[185] P. Dogan *et al.*, "Formation of High-Quality GaN Microcrystals by Pendeoepitaxial Overgrowth of GaN Nanowires on Si(111) by Molecular Beam Epitaxy," *Crystal Growth & Design,* vol. 11, no. 10, pp. 4257-4260, 2011, doi: 10.1021/cg200801x.

[186] P. Dogan, O. Brandt, C. Pfüller, A.-K. Bluhm, L. Geelhaar, and H. Riechert, "GaN Nanowire Templates for the Pendeoepitaxial Coalescence Overgrowth on Si(111) by Molecular Beam Epitaxy," *J. Cryst. Growth,* vol. 323, no. 1, pp. 418-421, 2011, doi: 10.1016/j.jcrysgro.2010.12.081.

[187] S. Zhao and Z. Mi, "Molecular Beam Epitaxy of Al(Ga)N Nanowire Heterostructures and Their Application in Ultraviolet Optoelectronics," in *Molecular Beam Epitaxy*, 2018, pp. 115-133, doi: 10.1016/B978-0-12-812136-8.00007-4.

[188] B. H. Le, S. Zhao, X. Liu, S. Y. Woo, G. A. Botton, and Z. Mi, "Controlled Coalescence of AlGaN Nanowire Arrays: An Architecture for Nearly Dislocation-Free Planar

Ultraviolet Photonic Device Applications," *Adv. Mater.*, vol. 28, no. 38, pp. 8446-8454, Oct 2016, doi: 10.1002/adma.201602645.

[189] Z. Bryan, I. Bryan, J. Xie, S. Mita, Z. Sitar, and R. Collazo, "High Internal Quantum Efficiency in AlGaN Multiple Quantum Wells Grown on Bulk AlN Substrates," *Applied Physics Letters,* vol. 106, no. 14, p. 142107, 2015, doi: 10.1063/1.4917540.

[190] K. Ban *et al.,* "Internal Quantum Efficiency of Whole-Composition-Range AlGaN Multiquantum Wells," *Applied Physics Express,* vol. 4, no. 5, p. 052101, 2011, doi: 10.1143/apex.4.052101.

[191] Ž. Podlipskas *et al.,* "Dependence of Radiative and Nonradiative Recombination on Carrier Density and Al Content in Thick AlGaN Epilayers," *Journal of Physics D: Applied Physics,* vol. 49, no. 14, 2016, doi: 10.1088/0022-3727/49/14/145110.

[192] C. Frankerl *et al.,* "Challenges for Reliable Internal Quantum Efficiency Determination in AlGaN-Based Multi-Quantum-Well Structures Posed by Carrier Transport Effects and Morphology Issues," *J. Appl. Phys.,* vol. 126, no. 7, 2019, doi: 10.1063/1.5100498.

[193] F. Nippert *et al.,* "Auger Recombination in AlGaN Quantum Wells for UV Light-Emitting Diodes," *Appl. Phys. Lett.,* vol. 113, no. 7, pp. 071107, 2018, doi: 10.1063/1.5044383.

[194] M. Shatalov *et al.*, "High Power AlGaN Ultraviolet Light Emitters," *Semicond. Sci. Technol.,* vol. 29, no. 8, pp. 084007, 2014, doi: 10.1088/0268-1242/29/8/084007.

[195] L. Ya-Ju *et al.*, "Study of the Excitation Power Dependent Internal Quantum Efficiency in InGaN/GaN LEDs Grown on Patterned Sapphire Substrate," *IEEE Journal of Selected Topics in Quantum Electronics,* vol. 15, no. 4, pp. 1137-1143, 2009, doi: 10.1109/jstqe.2009.2014967.

[196] Ž. Podlipskas *et al.*, "Dependence of Radiative and Nonradiative Recombination on Carrier Density and Al Content in Thick AlGaN Epilayers," *J. Phys. D: Appl. Phys.*, vol. 49, no. 14, pp. 145110, 2016, doi: 10.1088/0022-3727/49/14/145110.

[197] M. E. Rudinsky and S. Y. Karpov, "Radiative and Auger Recombination Constants and Internal Quantum Efficiency of (0001) AlGaN Deep ‐ UV Light ‐ Emitting Diode Structures," *physica status solidi (a)*, vol. 217, no.14, pp. 1900878 2019, doi: 10.1002/pssa.201900878.

[198] F. Nippert *et al.*, "Auger Recombination in AlGaN Quantum Wells for UV Light-Emitting Diodes," *Appl. Phys. Lett.*, vol. 113, no. 7, 2018, doi: 10.1063/1.5044383.

[199] A. Bhattacharyya, T. D. Moustakas, L. Zhou, D. J. Smith, and W. Hug, "Deep ultraviolet Rmitting AlGaN Quantum Wells with High Internal Quantum Efficiency," *Appl. Phys. Lett.*, vol. 94, no. 18, 2009, doi: 10.1063/1.3130755.

[200] A. Aiello *et al.*, "Optical and Interface Characteristics of $Al_{0.56}Ga_{0.44}N/Al_{0.62}Ga_{0.38}N$ Multiquantum Wells with ∼280 nm Emission Grown by Plasma-Assisted Molecular Beam Epitaxy," *J. Cryst. Growth*, vol. 508, pp. 66-71, 2019, doi: 10.1016/j.jcrysgro.2018.12.025.

[201] Q. Dai *et al.*, "Internal Quantum Efficiency and Nonradiative Recombination Coefficient of GaInN/GaN Multiple Quantum Wells with Different Dislocation Densities," *Appl. Phys. Lett.*, vol. 94, no. 11, 2009, doi: 10.1063/1.3100773.

[202] https://crosslight.com/.

[203] K. K. Ryu, J. C. Roberts, E. L. Piner, and T. Palacios, "Thin-Body N-Face GaN Transistor Fabricated by Direct Wafer Bonding," *IEEE Electron Device Lett.*, vol. 32, no. 7, pp. 895-897, 2011, doi: 10.1109/led.2011.2147751.